UNIVERSITÀ DEGLI STUDI DI NAPOLI
FEDERICO II

UNIVERSITÀ DEGLI STUDI DI NAPOLI FEDERICO II

PH.D. THESIS

IN

INFORMATION AND COMMUNICATION TECHNOLOGY FOR HEALTH

MICROFLUIDIC-BASED FEEDBACK CONTROL OF BIOLOGICAL SYSTEMS FOR BIOTECHNOLOGY AND BIOMEDICAL APPLICATIONS

ANTONELLA LA REGINA

TUTOR: PROF. MARIO DI BERNARDO

XXXV CICLO

SCUOLA POLITECNICA E DELLE SCIENZE DI BASE
DIPARTIMENTO DI INGEGNERIA ELETTRICA E TECNOLOGIE DELL'INFORMAZIONE

Alla mia famiglia

Candidate's declaration

I hereby declare that this thesis submitted to obtain the academic degree of Philosophiæ Doctor (Ph.D.) in is my own unaided work, that I have not used other than the sources indicated, and that all direct and indirect sources are acknowledged as references.

Parts of this dissertation have been published in international journals and/or conference articles (see list of the author's publications at the end of the thesis).

Napoli, March 10, 2023

_____

Abstract

Cybergenetics is an emerging discipline that combines functionalities from synthetic biology and control engineering. The biological systems of interest, such as unicellular or multicellular organisms, are often unpredictable and unstable to characterize. Therefore, to increase the robustness and reliability of the system, typical tools from control theory, such as feedback loops, can be employed.
In this work, we exploit how control engineering can be used to automatically steer complex biological processes towards desired behaviors with a microfluidics/microscopy platform. The platform allows to automatically regulate gene expression in real-time, in model-based or model-free scenario. Hence, cybergenetics tools, microfluidic-microscopy platforms, segmentation and control algorithms allow the precise tuning of such specific biological phenomena in different species such as yeast and mammals. Specifically, I will investigate the possibility to achieve long-term synchronization of cell population, by interfacing genetically modified yeast cells, and the precise tuning of mouse embryonic stem cells fate in a completely controllable automatized environment developing new protocols for long-term culture.

Keywords: cybergenetics, microfluidic, yeast, stem cells

Acknowledgements

This work of thesis is the output of my interaction with the amazing, motivating, and complex world of research, which lead me to grow up as a scientist and as a person and also to meet wonderful people.
I would like to thank Professor Mario di Bernardo and Professor Diego di Bernardo that letting me discover the fascinating world of cybergenetics.
I would like to express my sincere gratitude to Professor Mario di Bernardo for the chance to follow my interest in this field and for supporting me in this work. I would like to offer my special thanks to Professor Lucia Marucci, she gave me the opportunity to work in her system and synthetic biology lab at Bristol University. She offers me the chance to discover the "pros and cons" to work with such complex system as mouse embryonic stem cells. I am deeply grateful for her encouraging technical support, and for motivating me along the path with caring words. Thanks for showing me how to be a good researcher and thinker. I am deeply grateful for this opportunity. In addition, I want to thank all the collaborators that contributed to the research and in particular, I wish to thank Dr Elisa Pedone for her support and for the technical knowledge achieved in mammalian cell culture.
The research presented in this dissertation has been supported by Fondazione Telethon grant TGM16SB1, by the COSYBIO (Control Engineering of Biological Systems for Reliable Synthetic Biology Applications) project, which has received funding from the European Union's Horizon 2020 research and innovation programme under grant agreement 766840, by the Engineering and Physical Sciences Research Council (EPSRC, grant EP/S01876X/1), by the European Union's Horizon 2020 research and innovation programme (grant agreement 766840) and by BrisSynBio, a Biotechnology and Biological Sciences Research Council (BBSRC)/EPSRC Synthetic Biology Research Centre (BB/L01386X/1).

Contents

List of Figures

List of Tables

Chapter 1

Introduction

Synthetic biology is a discipline that allows the re-engineering of living organisms with new specific and useful functions, whereas control theory allows improving stability, robustness, and performance of physical systems [1],[2]. The interface between them leads to the definitions of a new field called Cybergenetics [3],[4].
Cybergenetics applications have a relevant impact on basic science, biotechnology, chemical industry, food and environment, health and biomedicine. Specifically, cybergenetics has the ability to robustly steer cellular behavior. This can be done with different types of controllers such as embedded, multicellular and external feedback control and with different experimental platforms such as microfluidic, optogenetic, and flow cytometry [5]. During the last two decades, several studies and scientific works have been conducted and published about the possibility to steer gene expression behavior for simple biological process with a microfluidic/microscopy experimental platform. The applications involved different species from bacteria, yeast, and mammals [6],[7],[8],[9],[10],[11],[12],[13].
Here, in this work, I will investigate the possibility to control complex biological phenomena with the use of the well know platform. I will investigate the possible implementation *in vitro* of external feedback control strategies in yeast and mammals. Specifically, I will demonstrate how the platform can be experimentally implemented for budding yeast cell cycle synchronization, and how can be used to experimental characterize and control mouse embryonic stem cells. Furthermore, new cybergenetics tools

for a possible scale-up of the experimental platform will be developed.

1.1 Outline of the thesis

- Chapter 2 presents an overview of cybergenetics applications and presents the experimental microfluidic-microscopy platform used to apply an external feedback control on biological system as yeast and mouse embryonic stem cells.

- Chapter 3 reports how to build a cybergenetic system to achieve long-term synchronization of yeast cell cycle across a population. The aim is achieved by interfacing genetically modified yeast cells with a computer by means of microfluidics to dynamically change medium, and a microscope to estimate cell cycle phases of individual cells. Specific controllers such as stop&go and Reference oscillator were experimentally implemented. The results of this work appears on the paper [14]. It has been developed at the Telethon Institute of Genetics and Medicine (TIGEM) in collaboration with Giansimone Perrino, Sara Napolitano, Francesca Galdi, Davide Fiore, Teresa Giuliano, and Diego di Bernardo.

- Chapter 4 presents new cybernetics tools that can allow the application of feedback control to monitor and study more complex biological systems. The new tools involve a new segmentation algorithm "Cheetah" based on a machine learning approach and a new microfluidic device for long-term culture for mammalian cells. Cheetah computational tool kit is described in [15] and it has been developed at the University of Bristol in collaboration with Elisa Pedone, Irene de Cesare, Criseida G. Zamora-Chimal, David Haener, Lorena Postiglione, Barbara Shannon, Nigel J. Savery, Claire S. Grierson, Thomas E. Gorochowski, and Lucia Marucci. The new microfluidic design described in [16] was developed at the University of Bristol in collaboration Adil Mustafa, Elisa Pedone, Ahmet Erten and Lucia Marucci

- Chapter 5 presents the possibility to characterize and control mouse embryonic stem cells dynamics via external feedback control in the

pluripotent state with the use of the microfluidic-experimental platform. Furthermore, in this work a new experimental protocol to culture and maintain mouse embryonic stem cells is reported. This work was developed at Bristol University in collaboration with Elisa Pedone and Lucia Marucci. In this field of interest, a literature review was published [17].

- Chapter 6 summarizes all the results obtained in the thesis and discuss possible future work.

1.2 Research products

The research done during the duration of the PhD was published in the following papers:

1. Giansimone Perrino, Davide Fiore, Sara Napolitano, Francesca Galdi, Antonella La Regina, Mario di Bernardo, and Diego di Bernardo. Feedback control promotes synchronisation of the cell-cycle across a population of yeast cells. In 2019 IEEE 58th Conference on Decision and Control (CDC),pages 933–938. IEEE, 2019

2. Giansimone Perrino, Sara Napolitano, Francesca Galdi, Antonella La Regina, Davide Fiore, Teresa Giuliano, Mario di Bernardo, and Diego di Bernardo. Automatic synchronisation of the cell cycle in budding yeast through closed-loop feedback control. Nature communications, 12(1):1–12, 2021

3. Elisa Pedone, Irene de Cesare, Criseida G. Zamora-Chimal, David Haener, Lorena Postiglione, Antonella La Regina, Barbara Shannon, Nigel J. Savery, Claire S. Grierson, Mario di Bernardo, Thomas E. Gorochowski, and Lucia Marucci. Cheetah: A computational toolkit for cybergenetic control. ACS Synthetic Biology, 10(5):979–989, 2021. PMID: 33904719

4. Elisa Pedone, Mario Failli, Gennaro Gambardella, Rossella De Cegli, Antonella La Regina, Diego di Bernardo, and Lucia Marucci. β-catenin perturbations control differentiation programs in mouse embryonic stem cells. Iscience, 25(2):103756, 2022

5. Adil Mustafa, Elisa Pedone, Antonella La Regina, Ahmet Erten, and Lucia Marucci. Development of a single layer microfluidic device for dynamic stimulation, culture and imaging of mammalian cells. bioRxiv, 2022

6. Antonella La Regina, Elisa Pedone, and Lucia Marucci. Culturing pluripotent stem cells: state of the art, challenges and future opportunities. Current Opinion in Systems Biology, 28:100364, 2021

Chapter 2

State of the art

2.1 Cybergenetics

The development of the Synthetic Biology discipline started in 1970 and it is related to the fields of molecular biology, genetic engineering, and genomics. Synthetic biology expansion can be characterized by two main phases: an early phase defined as the "era of modules" focused on forward engineering simple modules, such as switches and oscillators, and a second phase the "era of systems", in which modules will serve as functional units to create more complex systems with potential applications. The division is represented in figure 2.1. The possibility to re-engineer living organisms has potential in different fields of applications, including energy, environment, and medicine. Simple organisms such as bacteria or plants can clean hazardous waste or produce clean fuel in an efficient and sustainable fashion. Due to the technological progress in recent years, the potential for synthetic biology in human health care applications as cancer treatment, microbiome engineering, and regenerative medicine is improved [2]. Furthermore, new applications began across disparate fields such as biocomputing, living materials, electronic interfacing, therapeutic genome editing, cellular recording, and living biotherapeutics [18]. One of the well-characterized synthetic biology applications is the design of genetic control circuits to optimize biological processes through various biochemical processes, including transcription, translation, and post-translational processes. Even though is well-known how to build genetic circuits to

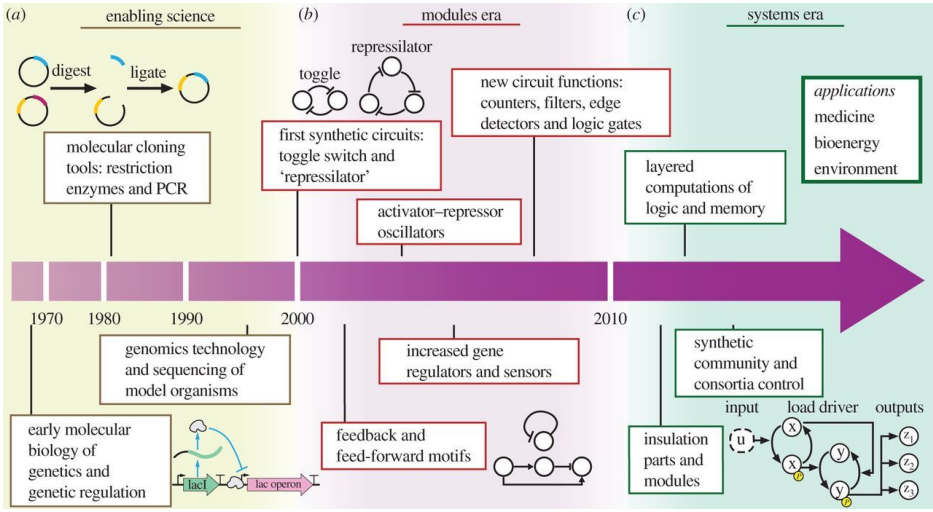

Figure 2.1. Timeline of synthetic biology. Adapted from [2].

control cellular behavior, the noisy nature of bio-molecular interactions makes those circuits need regulation for their correct operation, and often synthetic biology is associated and combined to control engineering [5].

Control engineering is an essential field for the analysis and regulation of dynamic systems. It is used in a number of applications for improving the stability, robustness, and performance of physical systems, such as mechanical devices, electrical or power networks, space and air systems, and chemical processes [19], [20]. Control theory's aim is to steer the behavior of a system to achieve the desired task. There are two types of control:

- open-loop control;
- closed-loop control.

In both, as reported in figure 2.2 a system and a controller are involved. In open-loop control, the system is forced to a certain assigned value $u(t)$ as input, using a reference $r(t)$ as a target, and no measurement of $y(t)$ as an output of the system is considered, whereas, in closed-loop feedback system the output value is measured and used to design a control action. In a classical negative feedback set-up, the controller measured the process

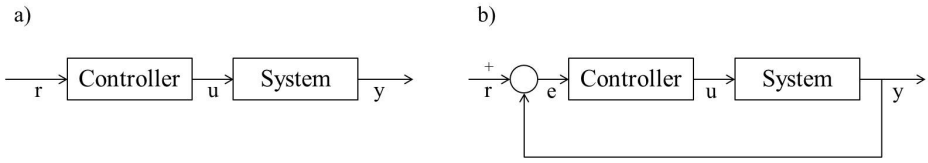

Figure 2.2. Types of control strategies. a) Open loop control b) Closed loop control

output of interest $y(t)$, compared it with the desired value $u(t)$, and, based on the error between these two applies a minimization computes the input to be applied to the process. Furthermore, negative feedback control is useful when the performance, reliability, and robustness of certain hardware components cannot be improved further by better characterization or hardware design [2].

A new and exciting area of study at the interface between control theory and synthetic biology has been recently introduced and we refer as Cybergenetics [4]. Cybergenetics will open up new directions in the field of control and estimation theory, indeed the capability to drive cellular behavior will be disruptive, enabling many applications in biotechnology, health, and biomedicine. It is possible to define three categories of control strategies in cybergenetics applications:

- embedded control, where the control action was embedded within the same cell hosting the process to be controlled,
- multicellular control, where the different functions needed to be implemented and localized in two different cell populations;
- external control, where a computer was interfaced with the biological process in the cell with actuators.

The different controllers proposed have advantages and disadvantages in their applications. For example, for the embedded control the system lacks modularity. As soon as a change in control design is required a complete re-engineering of the synthetic gene regulatory network is needed. For the multicellular control the full experimental implementation *in silico* and validation *in vivo* remained an open challenge. For the external

control it is possible to achieve accurate and fast regulation of gene expression. External control can be used for several applications and it brings to design and development specific tools and platforms to apply it. Many challenges remained in terms of deploying these platforms because most of them are not immediately translatable to 'outside-the-lab'. Even though recent advances in developing synthetic biological platforms are promising and the outcome could be disruptive [18]. Cybergenetics discipline holds great promise for addressing global needs in different fields.

2.1.1 External feedback control

System robustness is a relevant aspect of engineering and in biology, it is an explicit design requirement, and is a property of a specific functionality or performance measure. An engineered system that lacks robustness has little chance of delivering reliable functionality. The presence of model uncertainty, coupled with system perturbations and environmental disturbances leads to a lack of robustness. Negative feedback is a key element for achieving robustness, and its effectiveness can be seen in both fields of engineering and biology. Negative feedback is an intrinsic mechanism highly exploited and also preserved in nature. Furthermore, there are a wide variety of biological phenomena that provide a rich source of examples of negative feedback control, including gene regulation and signal transduction; hormonal, immunological, and cardiovascular feedback mechanisms; and population dynamics and epidemics. Several studies over the years investigate and exploit external feedback control applications to achieve control of biological processes [21], [22]. Figure 2.3 reported a negative feedback loop schema from an engineering point of view. It is characterized by four main elements: a system, a sensor, a controller, and an actuator. The output of the system $y(t)$ contains relevant information that can be used to compute the control input $u(t)$. In particular, the output of the system $y(t)$ is measured thanks to sensors and it is compared to the reference $r(t)$; the difference between the two signals is called control error $e(t)$. Control error influences the input $u(t)$ according to proper mathematical law. Indeed, the difference between reference and measured output is sent to a controller to minimize the future value of the control error.

A negative feedback approach has been implemented and applied *in vitro* over the years with the use of specific experimental platforms or ge-

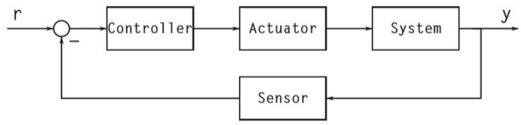

Figure 2.3. Negative feedback loop. Block scheme representing the negative feedback closed loop.

netic tools. The experimental aspects find large applications with different approaches. From an experimental point of view, the negative feedback loop is characterized by a system that in this case is composed of cells that need an environment with specific characteristics to grow, and elements such as microfluidic devices or turbidostats can be used for long-term cell culture; by a sensor and different types of sensors can be used to measure system output such as a microscope or a flow cytometer; by an actuation composed by syringes, pumps or light-based system applying a change in inducers concentration, drugs or expose the cells to the light of a specific wavelength and by a controller that is implemented in a computer. The most utilized controllers are Relay controllers, Proportional Integral Derivative (PID) controllers, and Model Predictive Control (MPC) to regulate gene expression in bacteria, yeast, and mammalian [23],[24].
As matter of fact, different experimental platforms are reported in the literature and are used for *in vitro* implementation. Indeed, the characterization and control of gene expression in yeast can be achieved via a microfluidic/experimental platform. Different control algorithms as Proportional-Integral (PI) and Model Predictive Control (MPC) controllers are used to forcing yeast cells to express a desired constant fluorescence level of a reporter protein using small molecules as control input [24]. Furthermore, external regulation of gene expression in yeast can also be implemented on a system base-light with other specific experimental platforms tailored for independent photo induction of gene expression with the purpose to regulate its transcription [25],[23]. A similar application was performed on mammalian cells with an optogenetic protein regulation combined with transcription visualization approaches [26],[27]. However, other successful attempts to control gene expression, or even signaling pathways, in mammals have been described in the literature based on external perturbation

and microfluidic approach to automatically regulate gene expression from inducible promoters in different cell types [10],[11] ,[23]. In addition, a further application for negative feedback control is to develop the theory and methodologies needed to build control systems at the molecular level. Different genetically engineered negative feedback circuits were reported and developed in yeast and mammal organism [28],[29]. Hence, the large and untapped potential of de novo design of proteins for generating tools that implement complex synthetic functionalities in cells for biotechnological and therapeutic applications is promising. One example can be the engineered synthetic circuit into human cells that can sense the glucose concentration and respond to correct deregulation [29]. The possibility to investigate, characterize, explore and control biological species with feedback control is growing in a wide range of possible applications with tremendous benefit for our health and well-being, and will drive major advances in basic science, industrial biotechnology, and medical therapy [30].

2.2 Biological systems

A biological system is a complex network that connects biological entities. New discoveries about genetic manipulation, explanation of biochemical pathways, and feedback controls in unicellular and multicellular organisms lead to the investigation and application of biological systems. From simpler organisms such as bacteria or yeast to more complex ones such as mammals can be used to investigate and explore a specific biological mechanism of interest [31].

2.2.1 Yeast

During the last years, an increasing number of molecular biologists have taken up yeast as their primary research system because the basic cellular mechanics of replication, recombination, cell division and metabolism are generally conserved between yeast and larger eukaryotes, including mammals [32]. Yeast *Saccharomyces Cerevisiae* can provide a key role to understand crucial biological mechanisms and is the most studied unicellular organism. It is a small, single-celled member of the kingdom of fungi, and

it is robust and easy to grow in simple nutrient media. An electron scanning of a cluster of yeast cells is reported in the figure 2.4. It is reported that yeast can reproduce in two different ways asexually or sexually and *Saccharomyces Cerevisiae* is characterized by asexual reproduction and occurs by asymmetric cell divisions. The reproduction process in living organism is ruled and regulated by a biological process, named cell cycle. Cell cycle is the critical chain of events by which the nucleus and all the other components of a cell are duplicated and parceled out to create two daughter cells from one. The daughter, from her side, contains the information and machinery necessary to repeat the process [33],[32],[34]. Cell cycle of budding yeast is characterized by 4 sequential phases:

- **Gap phase** $G1$
- **Synthesis phase** S
- **Gap phase** $G2$
- **Mitosis phase** M

In general, S and M phases are separated by two gaps, known as $G1$ and $G2$ as reported in the figure 2.5. The $G1$ phase depends on external conditions and guarantees cell growth. The transition from $G1$ phase to the S phase is ruled by a checkpoint called *Start transition*. This checkpoint is used to avoid the event that if DNA damage is detected or the cell has not reached the critical size, the cell arrests in $G1$ and is unable to undergo the Start transition. Otherwise, the *Start transition* commits the S phase trigger. S phase is able to initiate DNA replication and the start of budding formation, and the growth of bud proceeds in the $G2$ phase. The M phase is characterized by a second check point, called the *Spindle assembly checkpoint*; in the event that DNA damage is detected, DNA is not replicated completely, or chromosomes are not aligned on the metaphase plate, thus, the cell arrests in metaphase and is unable to undergo the finish transition, while if no DNA damage is detected the sister chromatids are able to separate and the cell division occurs. Furthermore, $G1$ is called as unbudded period, in which the cell can growth until to reach a certain critical value able to guarantee bud formation, whereas $S - G2 - M$ are called as budded period in which the new daughter mass

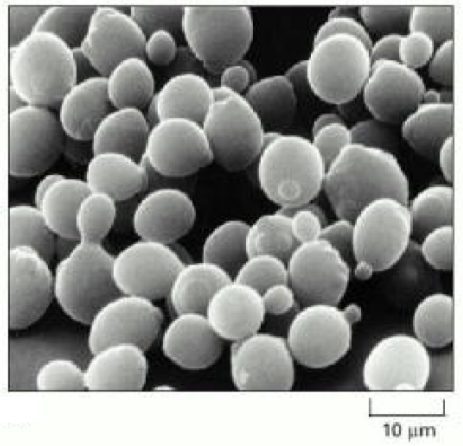

Figure 2.4. The yeast Saccharomyces Cerevisiae. An electron scanning of a cluster of cells. *S. Cerevisiae* proliferates by forming a bud that enlarges and then separates from the rest of the original cell. Many cells with buds are visible. Adapted from [33].

is generated. At the end of budded period, that is the end of M phase, it is possible to observe a budding division, i.e. the daughter cell is divided by the mother. The volumes of the parent cell and the bud formation were determined as were the intervals of the cell cycle devoted to the unbudded and budded periods. The daughter cell is the cell produced at division, and it is characterized by the volume growth generated during the cell cycle in $S - G2 - M$ phases. During the unbudded period both the daughter and the parent cell increase significantly in volume. Furthermore, *S. Cerevisiae* has an ovoid shape with a diameter of about $5 - 10\ \mu m$ [35].
Hence, the *Saccharomyces Cerevisiae* yeast cell cycle is an asynchronous process where each cell in the population budding at a different time. Even though the desynchronized behavior increases cellular heterogeneity and it may be advantageous in unicellular organisms for the survival of the population in unfavorable conditions, there are conditions such as biotechnological applications where the synchronization is required [36],[37].
In research, synchronization would enable the correct identification of cell cycle-dependent processes on the gene regulatory as well as on the metabolic level. The production and/or secretion rates of several het-

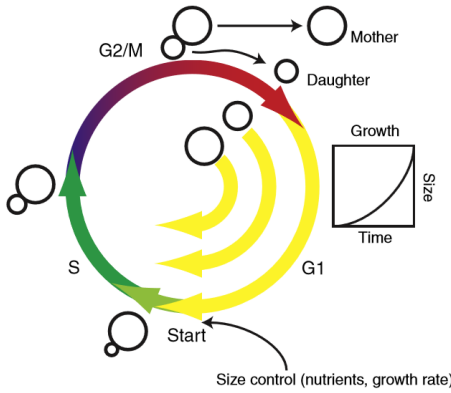

Figure 2.5. Size dependent cell cycle progression in S. Cerevisiae. Size control is a function of nutrient conditions and growth rate within the $G1$ phase. Daughter cells are born at different sizes and grow exponentially, smaller cells spend more in the $G1$ phase than the larger cells in order to partially compensate the initial size variation. Adapted from [34].

erologous proteins in the *Saccharomyces Cerevisiae* change during the cell cycle. Indeed, in industrial applications, a continuous, synchronized culture would implicate the purification of fewer amounts of media [38]. In literature, there are many methods with many advantaged and disadvantages to achieve cell synchronization. Biologists to obtain yeast cell cycle synchronization use typically open-loop control strategies or built ad-hoc for the process being controlled using empirical rules. Two main different methods are used when synchronization of the cell population is desired. It is possible to block cells at a specific stage in the cycle in a chemical or physiological approach but such methods suffer from the disadvantage that the cells have been interfered with and are therefore already abnormal in certain aspects or it is possible to select cells at a particular stage of the cell cycle. This may be on the basis of some physical property, e.g. the loose attachment of mitotic cells or the varying size or DNA content of cells at different stages of the cycle.
The method is chosen according to the queries of the experiment. It is sometimes preferable to perform the initial stages of an experiment with an unsynchronised exponentially growing culture and then to select cells at a given phase of the cycle by e.g. zone centrifugation for enzymatic anal-

ysis. In such experiments the cells, following selection, are not generally replaced in culture and so they may be exposed to an otherwise deleterious environment [39]. Despite all the different biological approaches the possible applications have relevant limitations. Indeed, there is no possibility to maintain synchronization over a long time period [40],[41],[38].
It is clear that new methods need to be developed, and the use of new technologies, such as cybergenetics, could overcome those limits.

2.2.2 Mouse embryonic stem cells

One of the most investigated mammal cell in the last years is stem cells. Stem cells are unspecialized cells able to differentiate into any cell of an organism and have the ability to self-renewal. There are several steps of specialization and developmental potency is reduced at each step. A stem cell classification is made on the degree of specialisation. Totipotent stem cells (able to divide and differentiate into cells of the whole organism), multipotent stem cells (they can specialize in discrete cells of specific cell lineages), oligopotent stem cells (can differentiate into several cell types), unipotent stem cells (characterized by the property of dividing repeatedly), and pluripotent cells (form cells of all germ layers but not extra-embryonic structures) [43],[44]. In my thesis, pluripotent stem cells are considered and studied and embryonic stem cells (ESCs) are an example of pluripotent stem cells [45], [46],[47],[48]. Pluripotent cells have the capacity to give rise to all the somatic lineages of the embryo and to the germline.
In vivo, the pluripotent state emerges during development of a totipotent zygote toward a blastocyst. This process delineates the inner cell mass (ICM), which is the pluripotent founder population, and the trophectoderm (TE), which forms an extraembryonic epithelial layer that envelopes and supports the ICM. At the late blastocyst stage (embryonic day 4.0 [E4.0]) the ICM consolidates to establish the pluripotent Nanog-expressing epiblast lineage and an overlying extra-embryonic layer of Gata6-expressing primitive endoderm. This point is defined as the developmental state characterized by uniform expression of key pluripotency factors (Nanog, Sox2, Oct4). This phase is liberated from epigenetic and developmental constraints and described as being in a "naive" or "ground" state of pluripotency, which reflects their unbiased developmental potential. As post-implantation development proceeds, however

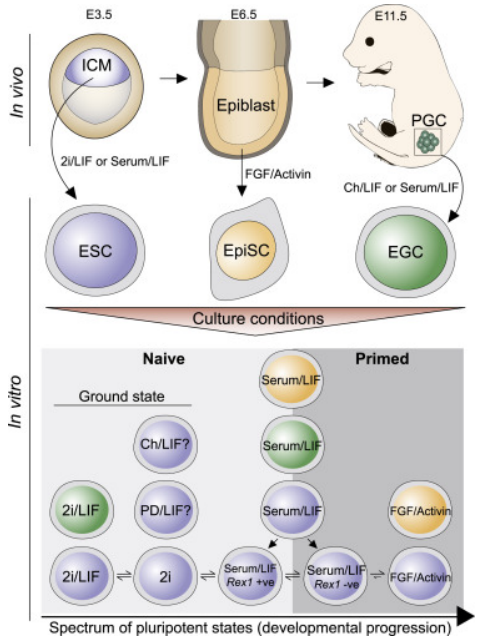

Figure 2.6. Embryonic origin and spectrum of pluripotent stem cell states. The pluripotent cells of a blastocyst between E3.5 and E4.5 can give rise to functionally naive ESCs (blue). Between E5.5 and E8.0 postimplantation epiblast can establish EpiSCs (orange), which occupy a primed pluripotent state. Additionally, primordial germ cells (PGCs), which are the founders of the germline lineage, can give rise to naive EGCs (green), which are highly comparable to ESCs. Depending on the culture/derivation conditions these pluripotent stem cells occupy discrete molecular states that can be broadly classed as naive or primed. The state of pluripotency adopted *in vitro* is primarily dictated by the combination extrinsic signals in the culture environment rather than the developmental source of the pluripotent cells. Adapted from [42].

(from E5.0), powerful inductive stimuli trigger naive epiblast cells to transit to a "primed" state of pluripotency that is poised to initiate lineage specification programs and is epigenetically restricted.
In vivo when development occurs from the inner cell mass up to the more differentiated state pluripotency is lost, whereas pluripotency can be recapitulated *in vitro* indefinitely. Nowadays, stem cells are the only *in vitro* system that allows to study and characterize pluripotency [42]. In this work, the mammalian cells, used for the investigation as a dynamic system, are the mouse embryonic stem cells (mESCs). Mouse embryonic stem cells are isolated for the first time in 1981 by Evans and Kaufman [49],[50] they are derived from the preimplantation epiblast or can also be obtained via reprogramming of differentiated cells using the Yamanaka factors [43],[51]. Mouse embryonic stem cells (mESCs) can exist in different pluripotency states depending on the media delivered. A picture of pluripotent mESCs is reported in figure 2.7. Nowadays, two types of mESCs media is mostly used for pluripotency cells expansion *in vitro*: serum-based and serum-free media [52],[53],[54]. It has been extensively reported that mESCs cultured in serum-based media enriched with the leukaemia inhibitory factor (LIF) present heterogeneous expression of pluripotency genes, and, on removal of pluripotency stimuli, transition to the primed state faster than serum-free cultured cells [55],[56],[57],[47],[58]. These results lead to the investigation of new serum-free culture protocols based on chemical perturbation of specific genes and signaling pathways, such as bone morphogenic protein-4 (BMP4), glycogen synthesis kinase-3 (GSK3) and mitogen-activated protein kinases/extracellular signal-regulated kinases (MEK/ERK). The ground state of naıve pluripotency was established by Wnt/β-catenin and MEK/ERK pathway inhibition with the glycogen synthesis kinase-3 (GSK3) inhibitor CHIR99021 (CH) and the MEK inhibitor PD0325901 (PD), respectively; indeed, their synergistic action promotes and sustains mESC self-renewal in 2i and 2i+LI cultures (the latter with further addition of the LIF) [59],[60]. Of note, the presence of CH and PD was shown to be beneficial for maintaining homogeneous pluripotent gene expression also in serum-based media [52]. Although the 2i+LIF medium is routinely used for ground state pluripotency cultures, it has been recently reported that prolonged expansion in this condition can cause irreversible epigenetic and

genomic changes that interfere with mESC developmental potential [61].

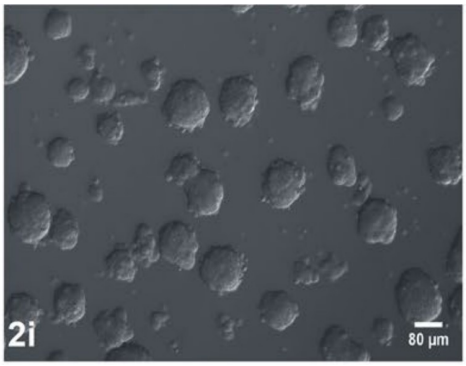

Figure 2.7. Morphological appearances of naive state of mESCs. Adapted from [53].

These effects seem to be owing to continuous MEK/ERK pathway inhibition, which can downregulate the DNA methyltransferases and their cofactors; therefore, a new medium (t2i/L) with decreased PD concentration was proposed [62]. Alternative serum-free formulations have also been recently introduced; mESCs cultured with the SRC inhibitor CGP77675, replacing PD in the a2i/L medium, showed preserved epigenetic and genomic integrity as well as developmental potential after long-term expansion [63]. In addition, simultaneous inhibition of MEK and the transforming growth factor-beta (TGFβ) receptor using PD and SB431542, respectively, in a new medium called R2i allowed efficient generation and maintenance of ground state naıve mESCs, protected from genomic integrity loss in long-term cultures [64]. A recent study proposed a chemically defined medium based on selective inhibition of cyclin-dependent kinases 8 and 19 (CDK8/19) [65], suggesting that different signalling pathways might be targeted for the establishment of naıve pluripotency [17]. Open challenges are still present in defining a detailed culture protocol for mESCs in a pluripotent state. The higher heterogeneous response to drugs and the genomic abnormalities caused by prolonged kinase inhibition leads to the necessity to define an advanced protocol that could allow biologists to overcome all those limitations. The emerging new technologies and theoretical approaches based on modeling, dynamical system theory and

machine learning could support the rational design of better culture protocols [66],[67]. In the literature, there are several mathematical models developed over the years. Most of them are characterized by the description of gene regulatory networks (GNR) involved in the process of stem cell maintenance linked to the culture media stimulation [68]. One example is a model developed to predict and simulate single-cell fate transitions in response to combinations of signaling pathways that typically occurs during development and differentiation [69]. However one of the main gene investigated for pluripotency maintenance in *in vitro* and in *in silico* is Nanog, which is expressed homogeneously in all cells in the pluripotent state. Nanog distribution can change dynamically. Notably, many of the metastable mESC genes are regulated by Nanog directly or indirectly process. Specifically, many investigations are based on the link between Nanog heterogeneity behavior in different serum-based or serum-free culture media [70]. Computational attempts to explain the origins and functions of Nanog dynamics in mESCs have been done over the years [71],[72],[73]. Furthermore many reporter cell lines have been generated to test experimentally via approaches, including flow cytometry and fluorescence activated cell sorting (FACS), time-lapse microscopy, single-cell sequencing. Nowadays, understanding the mechanism involved in pluripotency regulation is still an open challenge. Even though there are well-clear processes defined that can respond to time-varying stimuli the complexity of the phenomena did not allow to characterize and apply stimuli with desired amplitudes and temporal dynamics. The nascent field of cybergenetics could explore, perform and apply the desired input on our system. Indeed cybegenetics can control systems to dynamically regulate gene expression for specific stimuli. The stimuli to apply can be decided apriori or applied in real time based on a prediction of the best stimuli in the system. Indeed, control systems usually employ a negative feedback approach. As a matter of fact, the high number of parameters controlling cell fate as genetic background, gene network interactions and related non-linear dynamics, signaling pathways and experimental cell culture settings lead us to focus on the necessity to design robust pluripotent stem cell culture protocols. Indeed the vast majority of protocols for mESCs culture have been derived using trial and error approaches, which are expensive and time-consuming. Optimization of mouse embryonic stem cell culture based on the possibility

to apply cybergenetics could overcome some actual limitations in the field. Hence, the demand for scaling up stem cell cultures highlight the need of integrating computational approaches into the design of robust protocols which can enable reproducible results across laboratories.

Chapter 3

Automatic feedback control of cell cycle in budding yeast

In this chapter, I am going to describe the results achieved for yeast cell cycle synchronization. The results and methods are adapted from our work [14]. I contributed to performing in vitro experiments with both yeast strain, cycling and non cycling. I contributed with image and data analysis, and I helped with the modelling of yeast cell cycle focusing more on non cycling strain.

The cell cycle is the process by which eukaryotic cells replicate. In yeast cells, *S. Cerevisiae* is characterized by asexual reproduction and occurs by means of asymmetric cell divisions, and this phenomenon is called budding. The *Saccharomyces Cerevisiae* yeast cell cycle is an asynchronous process where each cell in the population budding at a different time. In biology, this phenomena of desynchronized behavior increase cellular heterogeneity and allowed the survival of the species in difficult enviroments, but there are biotechnological applications where the synchronization is required [36],[37].
Over the years, biologists developed different protocols and methods to synchronize yeast cell cycle [39], but there is no possibility to maintain synchronization over a long time period [40],[41],[38].
Cybergenetics discipline can be used to overcome those limitations. The idea is to investigate the feasibility of controlling the cell cycle by applying

this new promising area. In more detail is to build a cybergenetic system to achieve long-term synchronization of the cell population, by interfacing genetically modified yeast cells with a computer by means of microfluidics to dynamically change the medium, and a microscope to estimate cell cycle phases of individual cells. The computer implements a controller algorithm to decide when, and for how long, to change the growth medium to synchronize the cell cycle across the population.

3.1 Materials and methods

Experimental platform The closed-loop feedback scheme, represented in figure 2.3, can be implemented from an experimental point of view with a technological platform used to perform *in vitro* experiments on living bacteria, yeasts, and mammals. Figure 3.1 represents the several components of the platform, which are based on a microfluidics device, a time-lapse microscopy apparatus, a controller, and a set of automated syringes controlled by a computer.

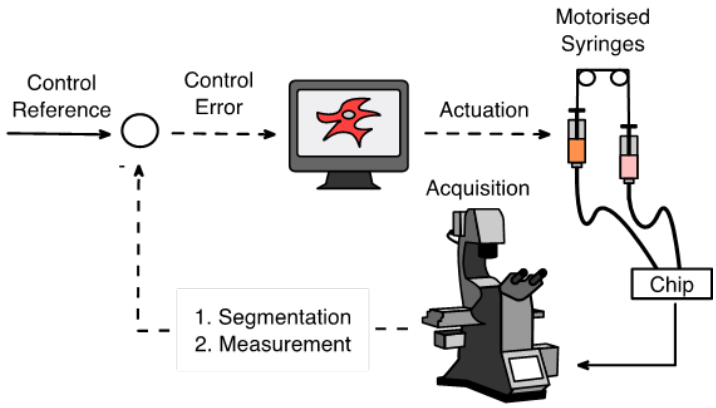

Figure 3.1. Overview of the experimental platform. Cells are loaded in a microfluidics device where two different growing media can be delivered to cells via an automated syringes system. A microscope acquires images in real time that are processed by a pc. [74].

The platform is able to work in either open-loop or closed-loop configurations. As open-loop configuration the computer is able to regulate

the actuators and deliver the decided input inside the microfluidics device located on the microscope, whereas in closed-loop configuration the computer compares firstly the acquired data from the microscope and then evaluates the best input to apply using a proper controller.

Actuators It is possible to control the medium reaching the cells just by changing the relative height of the two syringes. The syringes are connected to the inlet ports a specific design of the microfluidic device called DAW junction. The Dial–A–Wave junction was designed to combine the two inputs in a precise ratio depending on the pressures applied to the inlets and possible combinations of the fluids that arrive at the cells are reported in figure 3.2. The relative height variation applies hydrostatic pressures that rely on a system of two vertically mounted linear actuators. In detail, the actuation system comprises two linear guides and two stepper motors, that realize the motion of the syringes through two timing belts and four pulleys. Major details and specifications of the actuation system are reported in [75].

Miscroscopy and image analysis An inverted fluorescence microscope was used to monitor cell dynamics. The microscope was equipped with an automated and programmable stage, an incubator to guarantee fixed temperature and gasses to the cell environment, and a high sensitivity Electron Multiplying CCD (EMCCD) Camera. A fixed image area of the microfluidics device was acquired at regular time intervals using the camera. The camera can acquire both phase contrast and fluorescence im-

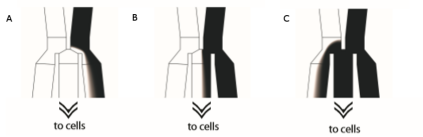

Figure 3.2. DAW junction for combining different fluids in a precise ratio. A) Administration of input 1 to the cells, ratio media 1 and media 2 is equal to zero. B) Administration of input 1 and 2 to the cells ratio media 1 and media 2 is equal to 50 %. C) Administration of input 2 to the cells, ratio media 1 and media 2 is equal to 100 %. Adapted from [76].

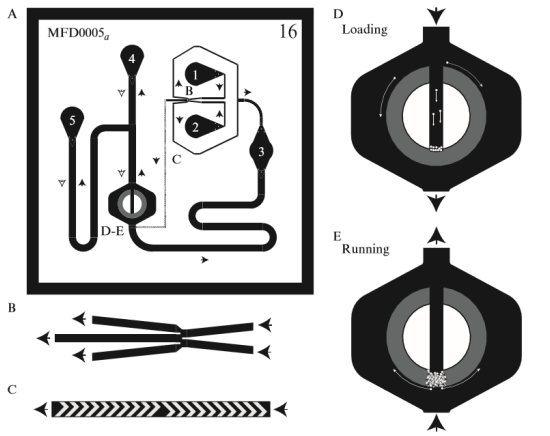

Figure 3.3. Overview of the $MFD0005_a$ chip. A) $MFD0005_a$ Device. B) Depiction of the DAW junction. C) Depiction of the SHM D) Overview of the trap region under loading conditions. E) Cells' trap upon running of an experiment. Adapted from [76].

ages. At this stage, segmentation algorithms are applied to measure the fluorescence signals expressed by fluorescent reporters.

Microfluidics The experimental approach involves the application of microfluidics technology. Microfluidics is the study and manipulation of fluids at the sub-millimeter length scale, which has collected great attention in the last twenty years thanks to the development of new technologies. Microfluidics receives great interest in biological field applications due to their ability to precisely control and perturb the environment of cells while their behavior is captured using a microscope [76]. The development and the use of microfluidic devices offer a number of significant advantages, such as the ability to track a cell over time and the use of small quantities of samples and reagents, compared to existing methods such as flow-cytometry and traditional microscopy [77]. The microfluidic device of interest used with the experimental platform is already published and designed for specific species such as yeast, bacteria, and mammals.

Yeast microfluidic device

Basic concepts of fluid mechanics are necessary to be considered when the design of a microfluidics device is realized. Indeed, at the micro-scale, the fluid mechanics is only ruled by the laminar flow conditions. A specific microfluidic device designed for yeast species application was considered for our work. The figure 3.3 represents the geometry of $MFD0005_a$ device [76]. It is designed to grow cells in a monolayer and to cope with high growth by flushing an excess of cells into a waste port. The device is characterized by 5 ports, a dial-a-wave junction (DAW), a staggered herringbone mixer (SHM), and a trap region. Port 1 and 2 are the inlets for the device and in particular for the DAW. The fluids enter separately from the two inlets and meet at the DAW junction, where the fluid that leaves the junction to the cell chamber is characterized by the pressure of the ports. The DAW is composed of two inlets and three outlets. Two are connected to port 3, called also cell and shunt waste port, where the excess fluid is diverted through a shunt network from the DAW junction, while the fluid of the center one, is delivered through a long channel, where the SHM is present, to the cell chamber. SHW is used to achieve a uniform concentration due to the limitation of phenomena diffusion. Indeed, the corkscrew design permits to increase in the surface area that logarithmically reduces the length of the channel necessary for uniform mixing. After mixing, the fluid moves to the cell chamber and proceeds to the outlet ports 4, 5, and 3. Figure 3.3.D characterizes the cell loading operation, where the gray region is the actual cell trap with a height of 3.50 μm while the black region has a height of 10 μm and is the cell chamber. In the black area, cells are represented with a white circle, the cells enter from port 5 and can pass around the trap and move to the shunt waste or can enter in the central channel and move to the trap entry barrier. Figure 3.3.E represents the cell trap upon a running experiment and in this case, the fluid is reverted, the yeast can grow and the colony expands to fill the entire trap and then will move out of the trap into the outer channel and be carried away to the waste port.

Yeast strains and growth conditions All Saccharomyces cerevisiae strains used in this study are congenic with W303 strain. The $SJR14a4d$ strain 34 is the non-cycling strain [78]. The $yDdB028$ strain was derived

from the $GC84-35B$ strain [79] and represents the cycling strain. The $yDdB028$ strain was constructed using standard procedures. The $HTB2-mCherry$ cassette was amplified via PCR on genomic DNA extracted from the $SJR14a4d$ strain and cloned into plasmid $pRS41N-GAP-CYC$ (a derivative of the nourseothricin-selective $pRS41N$ plasmid 39 containing the CYC terminator). The $HTB2-mCherry$ cassette was amplified from plasmid $pRS41N-GAP-HTB2-mCherry-CYC$ and inserted into the yeast $HTB2$ locus via homologous recombination [80] such that expression was synchronizing endogenous promoter. Both strains were grown at 30 °C in either synthetic complete medium, composed of yeast nitrogen base (0.67% w/v) with all amino acids; or synthetic complete drop-out medium, composed of yeast nitrogen base (0.67% w/v) with all amino acids except methionine; both supplemented with glucose (2% w/v) as carbon source.

Microfluidic device production, loading and experiments The microfluidics device used for yeast cell cycle experiments were performed with the MFD0005a device [81], charcaterized by a chamber in which the cells are trapped. Microfluidics devices were fabricated with a replica moulding technique, where the master-mould was produced using multi-layer soft-lithography with SU-8 as photoresist, and exposed to vapours of chlorotrimethylsilane (CARLO ERBA Reagents) for 10 min. Poly-dimethylsiloxane (PDMS; Sylgard 184, Dow Corning) was poured on the top of the master mould with a 1:10 ratio (curing agent to base; w/w) and cured at 80 °C for 2 hrs. Next, the PDMS layer was cut and peeled from the master mould and inlet ports were pierced with a micro-puncher (0.5 mm; World Precision Instruments) and then irreversibly bonded to a cover glass (thickness no. 1.5; Marienfeld Superior) through a plasma treatment for 30 s in a low-pressure plasma machine (ZEPTO version B; Diener electronic). The bonded device was baked for 2 hrs at 80 °C, and then stored at 4 °C until use. The experiments start with a microfluidics device filled with double distilled water for removing air bubbles. Next, two syringes filled with $+MET$ and $+MET$ media were first mounted on the automated actuation system and connected to the inlet ports of the microfluidics device. Afterward, three syringes filled with double distilled water were connected to the remaining ports of the microfluidics device for balancing the flow pressure inside the device. Finally, the microfluidics

device was placed in the opaque cage incubator of the microscope that was preheated to either 30 °C. For microfluidics experiments cells from a frozen glycerol stock (80 °C) were resuspended in 10 mL of either methionine-free (non-cycling strain) or methionine-supplemented (cycling strain) growth medium, grown overnight in a shaking incubator at 220 r.p.m. and 30 °C, and then injected in the microfluidics device by pouring the batch culture in a syringe that was temporarily connected to the loading port of the microfluidics device. After that, the operator run the image acquisition and the custom MATLAB software. At the beginning of the experiment, a region of interest (ROI) was selected on the first acquired phase contrast image and in that region the fluorescence signals obtained from cells have to be quantified.

Microscopy image acquisition and processing. Phase contrast and epifluorescence images were acquired at 2 min intervals at ×40 magnification (CFIPlan Fluor DLL 40× dry objective, NA 0.75; Nikon Instruments) using a Nikon Eclipse Ti-E inverted microscope (Nikon Instruments) coupled with an EMCCD cooled camera (iXon Ultra 897; Andor Technology). The microscope stage was surrounded by an opaque cage incubator (Okolab) able to maintain the temperature at either 30 °C. Time-lapse experiments were conducted with the Perfect Focus System (Nikon Instruments) enabled. Appropriate filter cubes were used to acquire the yellow (YFPHYQ and FITC for the cycling and the non-cycling strains, respectively; Nikon Instruments) and the red (TRITC HYQ; Nikon Instruments) fluorescence channels. Time-lapse image acquisition was controlled by the NIS-Elements Advanced Research software (Nikon Instruments). Raw phase contrast and epifluorescence images were processed using custom scripts implemented in the MATLAB environment. The images in the red channel were used to identify single-cell nuclei visible thanks to the nuclear fluorescence marker ($Htb2 - mCherry$). Next, the nuclei centroids were used as seeds for a Voronoi tessellation to generate a single-cell region mask to crop the phase contrast images around each cell. The resulting phase contrast cropped images were used to generate a binary mask defining the region of a single cell. We applied the function regionprops to all the single-cell masks to quantify the radius of each cell. Fluorescence intensities were then quantified by processing the yellow fluorescence im-

ages with the binary single-cell masks described above, using the function regionprops. Specifically, for the non-cycling strain the fluorescence is quantified as the average fluorescence intensity in the region selected by the binary mask; while for the cycling strain the fluorescence is quantified as the maximum fluorescence intensity detected in the region selected by the binary mask. Fluorescence intensities are measured in arbitrary units (a. u.). Single-cell traces were tracked in real-time using a custom tracking algorithm previously described [82].

3.2 Yeast strain for inducible cell cycle start

The cell cycle control system, in budding yeast, involves dozens of interacting genes and consists at its core of at least the $Cdk - APC/C$ oscillator. It is driven by a proteins circuit centered on the cyclin-dependent protein kinase (Cdk) and the anaphase-promoting complex (APC). In budding yeast, there is only one Cdk (called Cdc28) and nine different cyclins ($Cln1, Cln2, Cln3; Clb1, Clb2, Clb3, Clb4, Clb5, Clb6$). During normal cell cycle progression, the cell needs to grow sufficiently large to execute START. The major players involved in the budding yeast cell cycle are the cyclin Cln3 that ruled the "size control" of START. It is a dose-dependent activator of the $G1/S$ transition and had a very relevant role in cell cycle activation [34]. For cybergenetic applications, two engineered yeast strains have been selected and reported in 3.4.
The first strain which we referred to as the non-cycling strain, was engineered by Rahi et al. [78],[83],[84]. In the non-cycling strain, all the endogenous genes encoding the $G1$ cyclins ($Cln1, Cln2$, and $Cln3$) are deleted, thus making the cells unable to progress towards the S phase. To enable control of the cycle progression by changing the growth medium, the endogenous $Cln2$ gene was inserted downstream of the methionine repressible promoter P_{MET3}. In addition, to track the cell-cycle progression, a yellow fluorescent protein (YFP) was inserted downstream of the endogenous $Cln2$ promoter, and considering that the $Cln2$ promoter is activated in $G1$ and repressed in $G2$, the yellow fluorescence reporter can be used as a proxy of the cell-cycle phase, and also a nuclear fluorescence marker to help image analysis was added as a constitutively expressed histone $Htb2 - mCherry$. According to these modifications, the cell cycle of the

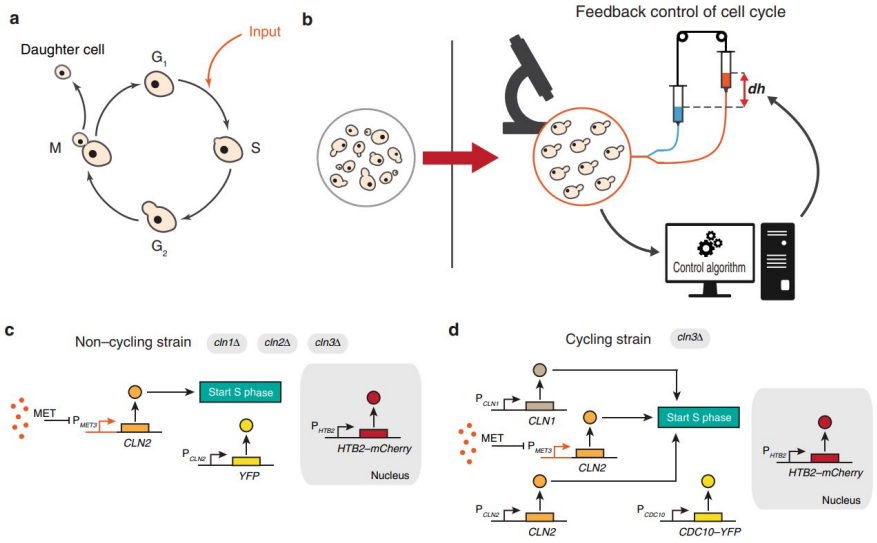

Figure 3.4. Cell cycle synchronization through automatic feedback control and yeast strains. a) Cell cycle phases of *S. Cerevisiae* yeast. b) Experimental microfluidics platform to automatically synchronize the cell cycle. c) Non-cycling yeast strain. Cells are deleted for genes encoding for the $G1$ cyclins $Cln1-3$ while an exogenous $G1$ cyclin gene $CLN2$ is placed under the control of the methionine-repressible promoter P_{MET3}. A yellow fluorescent protein (YFP) is expressed under the control of the endogenous promoter P_{CLN2}, and a red fluorescent nuclear reporter ($Htb2-mCherry$) is also present in this strain. d) Cycling yeast strain. Cells are deleted only for the $G1$ cyclin $Cln3$, and an exogenous copy of the $G1$ cyclin gene $CLN2$ is placed under the control of the methionine-repressible promoter P_{MET3}. A red nuclear fluorescence reporter ($Htb2-mCherry$) and a yellow fluorescence reporter, consisting of a fusion protein between endogenous mitotic septin Cdc10 and YFP ($Cdc10-YFP$), are also present in this strain. Adapted from [14].

non-cycling strain can be halted at the $G1$ phase in presence of methionine, or allowed to progress towards the S phase in absence of methionine [84]. The second strain, which we call the cycling strain, it was derived from the one described by Charvin et al [79]. In this strain, endogenous control of cell cycle initiation is maintained by preserving the genes encoding the $G1$ cyclins $Cln1$ and $Cln2$ and by deleting $Cln3$. An extra copy of $CLN2$ is placed under the control of the methionine-repressible promoter P_{MET3}. In addition, to track cell cycle progression, a yellow fluorescence reporter was inserted as a mitotic septin $Cdc10-YFP$ to characterize the $S-G2-M$ phases of the cell cycle, and also a nuclear fluorescence marker to help image analysis was added as a constitutively expressed histone ($Htb2-mCherry$). According to these modifications, the cell cycle of the cycling strain can cycle independently of methionine levels in the growth medium. Both strains will be characterized and described to apply on them an external feedback control to achieve yeast cell cycle synchronization.

3.3 Mathematical modeling of yeast cell cycle

Any biological system has the potential for generating oscillations, showing the ability to display fascinating spatial and temporal patterns, which hint that the underlying cellular processes are highly dynamic and operate on a wide range of time and length scales. A biological oscillator can be defined as a system that generates a periodic variation of a molecular species. The development of new techniques to quantitatively measure gene expression in cells has shed light on a number of systems that display oscillations in protein concentration [85]. An oscillation is defined as a cyclic change of a physical quantity and is characterized by a relatively constant waveform and a period. Thus to characterize an oscillation, the most relevant information is the period and the phase. The period is defined as the time interval between two identical reference points on the waveform. The phase is useful to characterize the comparison of rhythms between different oscillators. In an isolated oscillator, the phase is able to exhibit a precise periodic rhythm.
From a mathematical point of view, an oscillator is defined as a nonlinear autonomous dynamical system that exhibits self-sustained oscillations. In the case of a biological oscillator, these self-sustained oscillations are gener-

ated by periodic variations of molecular species. Biological oscillators can be modeled as nonlinear phase oscillators by exploiting the phase reduction theory. The phase reduction theory is a powerful method for analyzing the properties of oscillators [86]. Indeed, multidimensional dynamical equations describing oscillatory systems can be reduced to a one-dimensional differential equation, that describes the temporal evolution of the oscillations. The phase reduction theory was introduced in the 1950s by Arthur T. Winfree, which is considered the pioneer of this theory. In the 1980s, this theory was improved and extended by Yoshiki Kuramoto who introduce the Kuramoto theory. Indeed in the late 1970s, Kuramoto proposed a solvable coupled oscillator model that exhibits collective synchronization transition considering the concept of collective synchronization of globally coupled oscillator populations [87],[88]. Overall, one of the main aspects of Kuramoto's theory to consider is the introduction of a complex order parameter, the Kuramoto index defined as reported in 3.1:

$$R(t)e^{j\psi(t)} = \frac{1}{N(t)} \sum_{m=1}^{N(t)} e^{j\theta_m(t)} \tag{3.1}$$

where $N(t)$ is the time-varying number of cells, ψ the mean phase $\in [0, 2\pi]$, $\theta_m(t)$ the phase of the mth cell, both evaluated at time t and R is defined as the mean phase coherence, with $R \in [0, 1]$. Kuramoto order parameter can be used to evaluate the synchronization among the cell cycle phases. Indeed, when R is equal to 1, all cells are synchronized, whereas R equal to zero are desynchronized [88].
Furthermore, in biology to characterize cell cycle syncronization a specific index is used, the budding index (B.I.) as reported in 3.2. It is computed as the percentage of budded cells within the population and it is expected to remain constant over time for an unsynchronised cell population.

$$B.I.(t) = \frac{N_{S-G2-M}(t)}{N(t)} * 100 \tag{3.2}$$

where $N(t)$ is the total number of cells at time t and $N_{S-G2-M}(t)$ is the number of budded cells (i.e. cells in the S-G2-M phases) at time t.

Nowadays, according to the increasing number of theories and their possible investigation, the possible information that can be obtained using mathematical theory is quantitatively increased [89]. Hence, we constructed a deterministic agent-based mathematical model to describe and characterize the collective dynamical behavior of the cell cycle in both strains. The agent-based model is based on the idea that each agent represents a cell in the population [4],[90].
The model of a single agent is based on a set of two state-dependent ordinary differential equations (ODEs), which follow the evolution of cell cycle phase θ and cell volume V in each cell:

$$\frac{d}{dt}\theta = \begin{cases} 0 & \text{if} \quad 0 \leq V < V_c \\ f(\theta) + z(\theta)u & \text{if} \quad V \geq V_c \end{cases} \tag{3.3}$$

$$\frac{d}{dt}V = g(\theta) \tag{3.4}$$

where $\theta \in S^{-1}$ is the 2π periodic cell cycle phase on the unit circle, $V \in R_+$ is the cell volume, $V_c \in R_+$ is the critical volume and $u \in [0, 1]$ is the external input. The external input represents the methionine-rich ($u = 0$) or methionine-depleted ($u = 1$) growth medium, whereas V_c the critical volume defines the minimum volume required to start the cell cycle, and it also allows us to distinguish between the mother ($V \geq Vc$) and daughter ($0 \leq V < Vc$) cells.
Furthermore, the cell volume growth rate during the G1 phase is defined by the phase-dependent switching function $g : S^1 \to R_+$:

$$g(\theta) = \begin{cases} \beta V & \text{if} \quad 0 \leq \theta < V_{G1/S} \\ 0 & \text{if} \quad \theta_{G1/S} \leq \theta < 2\pi \end{cases} \tag{3.5}$$

where $\beta \in R_+$ is the volume growth rate and $\theta_{G1/S}$ is the cell cycle phase value at the $G1$ to S transition. In the cell cycle model, some extra assumptions were needed. We assumed that volume growth in the mother cell occurs only in the $G1$ phase, whereas the bud grows in volume only during the $S - G2 - M$ phases.

The phase-dependent switching function $f : S^{-1} \to R_+$ is able to model the phase oscillator dynamics, and it changes according to the specific strain.

For the non-cycling strain, the function $f := f_{nc}$ is state-dependent:

$$f_{nc} = \begin{cases} 0 & \text{if } 0 \leq \theta < \theta_{G1/S} \\ \omega & \text{if } \theta_{G1/S} \leq \theta < 2\pi \end{cases} \tag{3.6}$$

where $\omega = 2\pi/T$ is the angular velocity depending on the cell cycle period T.
For the cycling strain, the function$f := f_c$ becomes state-independent:

$$f_c = \omega \tag{3.7}$$

Finally, the phase response curve $z \in S^1 \to R_+$ models the linear response of the cell cycle phase θ to the input u:

$$z(\theta) = \begin{cases} \omega_z & \text{if } 0 \leq \theta < \theta_{G1/S} \\ 0 & \text{if } \theta_{G1/S} \leq \theta < 2\pi \end{cases} \tag{3.8}$$

where $\omega_z \in R_+$ is the angular velocity added to the cell cycle phase dynamics when the cell is fed with a methionine-free medium.
Besides this agent-based model also considers cell division events with the addition of a new event when a cell passes through the M to $G1$ transition ($\theta_{M/G1} = 2\pi$), and the initial condition of the daughter cell depends on the state of the mother cell. In table 3.1 are reported the values used in the simulation of the agent-based model for both strains.

Table 3.1. Parameter values used in the agent model of the non-cycling and cycling strain

Parameters	Non cycling	Cycling
Initial phase	$\Theta_0 = 0$	$\Theta_0 = 0$
Initial volume	$V_0 = 0.61 V_{M/G1}$	$V_0 = 0.61 V_{M/G1}$
Volume of the mother	$V_M/G1$	$V_M/G1$
Critical volume	$V_c = 1$	$V_c = 1$
Volume growth rate $[min^{-1}]$	$\beta = 0.00083$	$\beta = 0.00083$
Nominal cell cycle period $[min]$	$T = 75$	$T = 105$
Angular velocity	$\omega_z = 2\pi/T$	$\omega_z = \pi/T$
Phase value at G1/S transition	$\theta_{G1/S} = \pi/2$	$\theta_{G1/S} = 4/5\pi$

3.4 *In silico* and *in vitro* validation of yeast cell cycle syncronitation

After model characterization, new approaches to characterize and study yeast cell cycle were performed. Indeed, *in silico* simulations were computed and then *in vitro* experiment for the investigation on how to characterize the cell cycle with the experimental-microfluidic platform as reported in the chapter 2. The platform allowed to perform experiments as open-loop or closed-loop. In the specific case, for the external feedback control application, the quantity to be regulated (e.g. the cell-cycle phase of each cell) is measured in real-time and then the controller, usually implemented in a computer, adjusts the input accordingly (e.g. duration and timing of the stimulation) to achieve the control objective (e.g. synchronization of cell cycle across cells). For both strains, experimental characterization was performed and then different control strategies were applied. For the non-cycling strain a stop&go control algorithm, whereas for the cycling strain a reference oscillator. As outcome of the experiments, information such as the number of cells, the mean of YFP fluorescence intensity, cell tracked, budding index and input delivered were evaluated to get info on cell cycle behavior.

3.4.1 Non cycling strain

First of all, the non-cycling strain was characterized by the experimental platform reported in figure 3.1. Hence, unforced experiments and a set of open-loop experiments were performed. In the case of non-cycling yeast cells under the conditions of methionine-depleted medium cells are able to cycle, considering the increase of cell number in an exponential way, and the YFP fluorescence intensity averaged across the population shows a flat profile due to cells not cycling in phase. After this first yeast characterization, a set of open-loop experiments was performed. To characterize the cell cycle different periodic pulses of methionine depletion as $T_u = 60, T_u = 75, T_u = 150$ and duration $D_Met = 20$ min or 30 min were tested according to the data obtained from *in silico* simulation.
Numerical simulations show that the forcing period T_u plays a key role in achieving cell cycle synchronization across the population. It must be

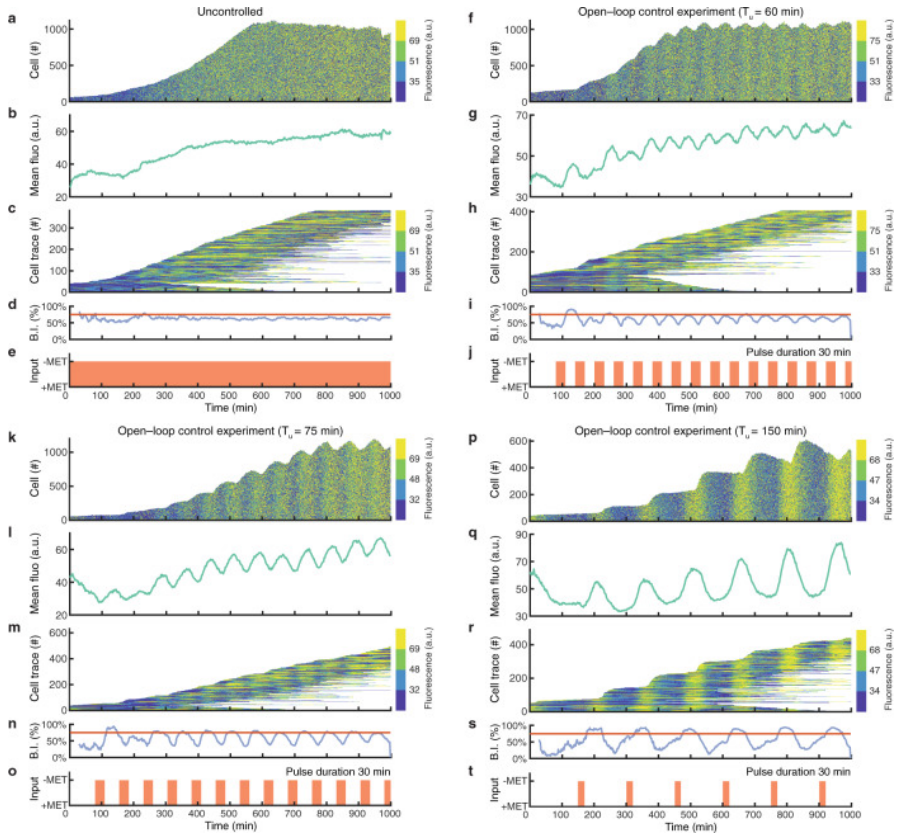

Figure 3.5. Characterisation and open-loop control of the non-cycling yeast strain. Experiments with non-cycling yeast strain cells grown in the automated microfluidics platform in four different conditions: (a–e) methionine-depleted medium ($-MET$); (f–j) alternating pulses of methionine-rich ($+MET$) and methionine-depleted (MET) medium with a period $Tu =$ 60min; (k–o) alternating pulses with a period $Tu =$ 75min; (p–t) alternating pulses with a period $Tu = 150$ min. Duration of MET pulse was set to 30 min. a, f, k, p) Number of cells and the distribution of YFP fluorescence intensity in the population over time. b, g, l, q) Average YFP fluorescence intensity in the cell population. c, h, m, r) Single-cell fluorescence traces over time. d, i, n, s) Budding index (blue) reporting the percentage of cells in the budding phase ($S - G2 - M$) computed from the estimated cell cycle phases. The red line denotes the expected value of the budding index in the case of a totally desynchronized cell population. e, j, o, t) Growth medium delivered to the cells as a function of time $+MET$ methionine-rich medium, $-MET$ methionine-depleted medium. Adapted from [14]

greater than the intrinsic cell cycle period (i.e $Tu \leq 75$min) [14]. The longer the period (Tu), the larger the average cell volume (V). Experimental results confirmed what numerical simulations predict.
Even though there is the possibility to synchronize cells using periodic stimulation, the open-loop control strategy is highly sensitive to environmental conditions. For example, there is a possible variation due to the periodic stimulation, pulse duration, and grown conditions. To overcome the drawbacks of open-loop control, we implemented a closed-loop feedback to automatically synchronise yeast cells cycle over cell population. Specifically, for non-cycling strain, a stop&go control algorithm was implemented. It is an event-triggered feedback control strategy that was devised to synchronize the cell cycle across a population [90]. Stop&go algorithm computes the percentage of cells in the $G1$ phase by means of the estimated cell cycle phases, at each sampling time t_k. A fixed threshold $\upsilon\%$ rules the presence or absence of methionine in the growth media. If the percentage of cells in the $G1$ phase is higher than the threshold the algorithm delivers a MET pulse of duration D_{Met} to the cells, otherwise, cells are kept in $+MET$ medium. *In silico* simulation reported in figure 3.6 were implemented with a threshold $\upsilon_{\%}$=100% and $D_{Met}t = 30$ min (duration of MET pulse). The number of cells over time increases indicating synchronization; the population average fluorescence signal and the budding index are oscillatory, as expected for synchronized cells, and the external input became a quasi-periodic signal after a transient period. From numerical simulations, it is achieved yeast cell cycle synchronization with the stop&go control strategy. For those reasons, an experimental implementation of the stop&go feedback control strategy was implemented with a threshold fixed to $\upsilon_{\%}$=50%. The experiment was designed with starting conditions of desynchronized population yeast cells, which were cultured overnight in the absence of methionine. The controller was switched on after 30 min of calibration and switched off after 500 min of the controlled experiment. Stop&go controller at each sampling time estimates the cell cycle phase of each cell across the population from fluorescence microscopy images and decides the type of media to deliver inside the microfluidic device. As reported in figure 3.6 the data related to the number of cells, the mean fluorescence of YFP, and BI allows us to confirm that the stop&go control strategy is able to automatically synchronize the cell population

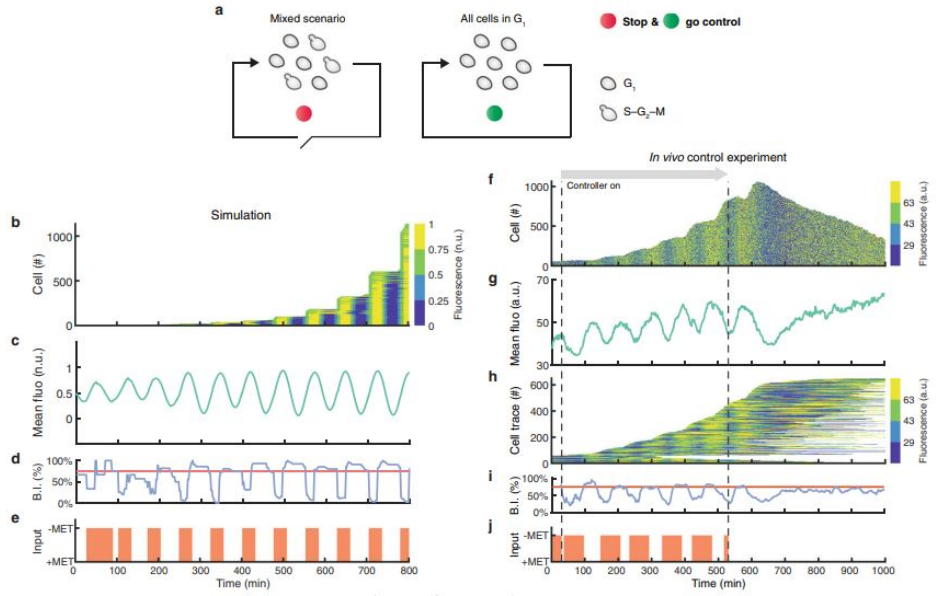

Figure 3.6. Automatic feedback control enables cell cycle synchronisation in the non-cycling yeast strain. a) Depiction of the stopgo control strategy. b–e) Numerical simulation of the stopgo control strategy. f–j) Experimental implementation of the stop&go control strategy. Dashed lines indicate the start and the end of the control experiment, after which cells are grown in methionine-rich medium. b, f) The number of cells and the distribution of YFP fluorescence intensity in the population over time. c, g) Average YFP fluorescence intensity in the cell population. h)Single-cell fluorescence traces over time. d, i) Budding index (blue) reporting the percentage of cells in the budding phase ($S - G2 - M$) computed from the estimated cell cycle phases. The red line denotes the expected value of the budding index in the case of a totally desynchronized cell population. e, j) Growth medium delivered to the cells as a function of time $+MET$ methionine rich medium, $-MET$ methionine depleted medium. Adapted from [14].

over time, even in the condition of new and unexpected environmental perturbations

3.4.2 Cycling strain

Next, the cycling strain was characterized by the experimental platform. Hence, unforced experiments in the absence and in the presence of methionine and open-loop experiments were performed. As expected in both conditions, the number of cells increases exponentially over time, while cells are desynchronised as evidenced by the flat profile in the average YFP fluorescence intensity and in the budding index. For the open-loop experiment, a periodic stimulation with $-MET$ pulses of period $Tu = 80$ min and duration $D_{Met} = 20$ min was selected according to previous results published by Charvin et al.[79]. Their experimental results were confirmed also with our experimental setup. To assess more robustness to cell cycle synchronization a closed-loop feedback control was designed.

For cycling strain, a reference oscillator feedback control strategy was proposed and implemented. It was adapted from the theory proposed by Bai and Wen to synchronize a homogenous population of nonlinear phase oscillators using a common input [91]. The strategy is based on a continuously cycling computer-generated in silico virtual yeast cell coupled to the real cells via the microfluidic device according to a star-like topology. The virtual cell behaves as a reference oscillator for all the other cells. The ODE model was built to describe the evolution of the reference oscillator phase θ_r on the unit circle S^1 over time:

$$\frac{d}{dt}\theta_r = \omega_r + \gamma \sum_{m=1}^{N} sin(\theta_m - \theta_r) \tag{3.9}$$

where $\omega_r \in R_+$ is the natural frequency of the reference oscillator, $\gamma \in R_+$ is the coupling strength, $N \in N$ is the number of cells, $\theta_m \in S^1$ is the cell cycle phase of the mth cell in the population computed at each sampling time t_k and N_k is the number of cells whose phases have been measured at sampling time t_k. Then, the algorithm computes the control action $u(t_k)$ to apply to the cell population through the state feedback control law:

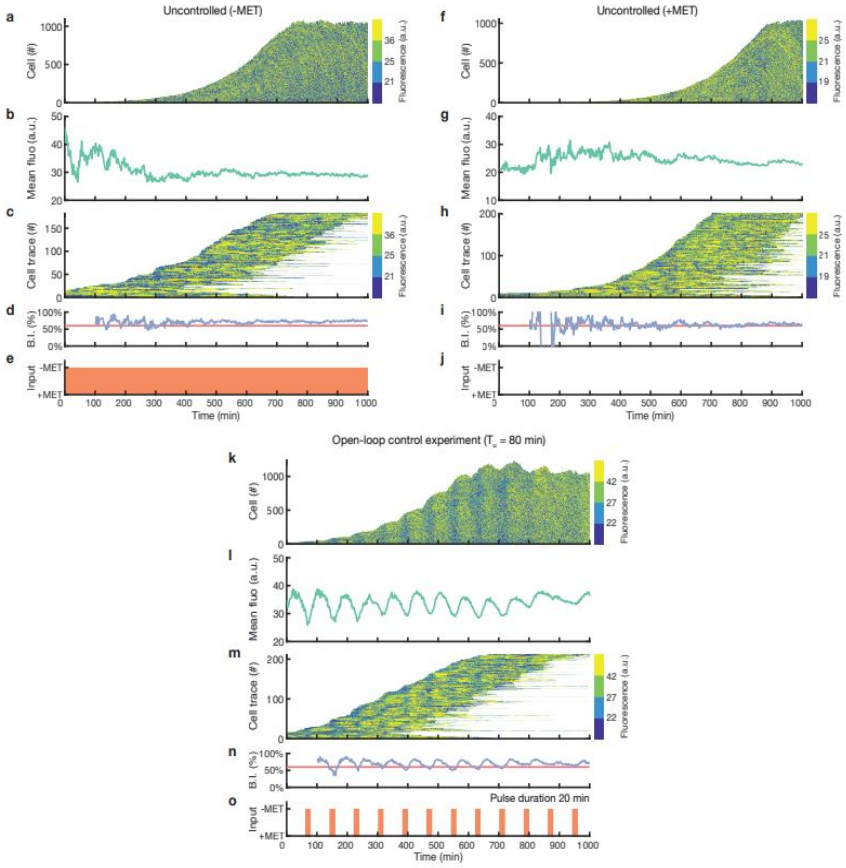

Figure 3.7. Characterisation and open-loop control of the cycling yeast strain. (a-e) methionine-depleted medium ($-MET$); (f-j) methionine-rich medium (+MET); (k-o) alternating pulses of methionine-rich ($+MET$) and methionine-depleted ($-MET$) medium with a period $T = 80$ min. Duration of $-MET$ pulse was set to 20 min. a, f, k, The number of cells and the distribution of YFP fluorescence intensity in the population over time. b, g, l, Average YFP fluorescence intensity in the cell population. c, h, m, Single-cell fluorescence traces over time. d, i, n, Budding index (blue) reporting the percentage of cells in the budding phase ($S-G2-M$) computed from the estimated cell cycle phases. The red line denotes the expected value of the budding index in the case of a totally desynchronised cell population. e, j, o, Growth medium delivered to the cells as a function of time $+MET$ methionine-rich medium, $-MET$ methionine-depleted medium. Adapted from [14].

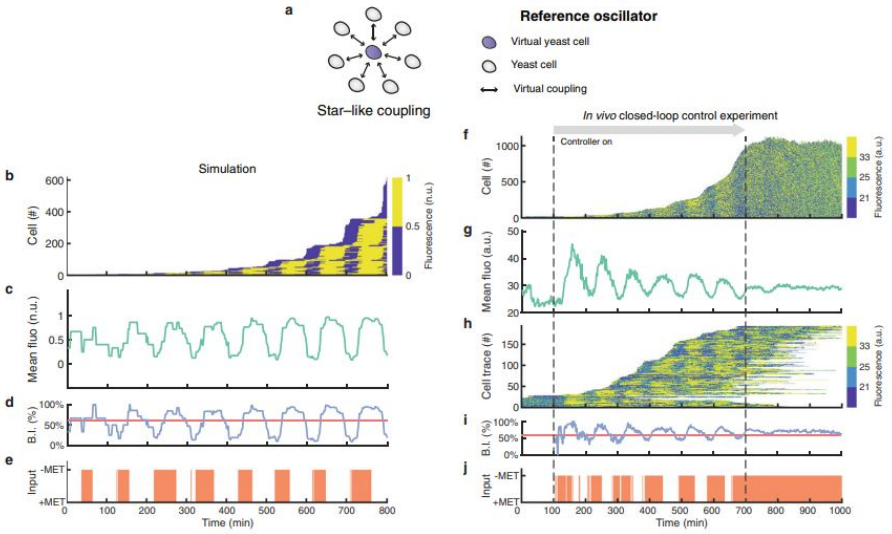

Figure 3.8. Automatic feedback control enables cell cycle synchronization in the non-cycling yeast strain. a Schematic illustration of the reference oscillator control strategy. Yeast cells are coupled to a virtual cell so that each cell cycles in synchronization with the virtual cell. b–e Numerical simulation of the reference oscillator control strategy. f–j Experimental implementation of the reference oscillator control strategy. An initial calibration phase of 100 min is required to set up the phase estimation algorithm. Dashed lines indicate the start and the end of the control experiment, after which cells are grown in a methionine-depleted medium. b, f The number of cells and the distribution of YFP fluorescence intensity in the population over time. c, g Average YFP fluorescence intensity in the cell population. h Single-cell fluorescence traces over time. d,i Budding index (blue) reporting the percentage of cells in the budding phase ($S - G2 - M$) computed from estimated cell cycle phases. The red line denotes the expected value of the budding index in the case of a totally desynchronised cell population. e, j, Growth medium delivered to the cells as a function of time $+MET$ methionine-rich medium, MET methionine-depleted medium. Adapted from [14].

$$u(t_k) = \begin{cases} +MET & \text{if} \quad \sum_{m=1}^{N_k} a_m(t_k) sin(\theta_m(t_k) - \theta_r(t_k) \geq 0 \\ -MET & \text{if} \quad \sum_{m=1}^{N_k} a_m(t_k) sin(\theta_m(t_k) - \theta_r(t_k) \leq 0 \end{cases} \tag{3.10}$$

where $\theta_r(t_k)$ is the phase of the reference oscillator at the sampling time t_k, $\theta_m(t_k)$ is the cell cycle phase of the mth cell measured at the sampling time t_k; and $a_m(t_k) \in [0, 1]$ is a time-dependent coefficient associated to the mth cell denoting if that cell is in the $G1$ phase at the sampling time t_k that is:

$$a_m(t_k) = \begin{cases} 1 & \text{if} \quad 0 \leq \theta_m(t_k) \leq \theta_{G1/S} \\ 0 & \text{if} \quad \theta_{G1/S} \leq \theta_m(t_k) \leq 2\pi \end{cases} \tag{3.11}$$

where $\theta_{G1/S}$ is the phase at the $G1$ to S transition. The algortihm intgrates the ODE model of the reference oscillator to obtain the value of the reference phase θ_r, using MATLAB numerical solver ode45. The numerical simulations of the reference oscillator strategy show effective synchronisation of the cell cycle population. We thus tested the reference oscillator feedback control strategy experimentally and assessed its synchronisation performance. The experiment start from a desynchronised population, yeast cells were cultured overnight methionine-rich medium. The controller was switched on after 100 min of calibration and switched off after 600 min of the controlled experiment. The controller was able to synchronise the cell population in agreement with numerical simulations, as evidenced by the large oscillations in the average YFP fluorescence intensity and in the budding index. Furthermore, it is possible also confirmed that once the controller is turned off, cells quickly desynchronise. These results demonstrate the feasibility of synchronising the cell cycle across the population using the reference oscillator control strategy, which is more robust than open-loop control strategy that is highly sensitive to environmental conditions.

3.5 Discussion

In nature, the cell cycle in budding yeast is an unsynchronised process (i.e yeast cell over a population bud at a different time). Biologists

and biotechnologists can achieve cell cycle synchronization, but only for short-term synchronization. In this chapter, using cybergenetics tools, a completely automatic system able to achieve long-term synchronization of the cell population was proposed. Tools such as engineered yeast cells, microfluidic, microscope, computer, and control theory were used. The implementation of the control algorithm allows the decision of when, and for how long, to change the growth medium to synchronize the cell cycle across the population. It has been shown how open-loop approaches are less robust than closed-loop feedback control. Even though closed-loop approaches are more complex to implement than open-loop approaches, the possibility to control cell cycle yeast in a robust way can have disruptive outcomes in industrial applications.

Chapter 4

New methods for cybergenetic

In this chapter, I am going to describe the results achieved for the development of new cybergenetics tools. The results and materials are adapted from our works [15],[16]. In Pedone et al. I contributed to performing experiments with mESCs and generating training data with the new tools, whereas in Mustafa et. al I helped with the experiments and cell culture.

The development of cybergenetics disciplines growth exponentially during the last 20 years in a proportional way to the progress of new technologies. Experimental platforms with optogenetic or microfluidic applications have been developed and broadly used [5].
Even though those platforms are already used for *in vitro* applications with bacteria, yeast, and mammal, a new upgrade of the platform is needed according to the biological phenomena and characteristics that the scientist wants to take trace. Indeed, there are still some limitations and open challenges to maintaining long-term culture for mammalian cells in a microfluidic device and also the possibility of achieving a robust segmentation algorithm to avoid wrong system output measurements.
Here, new advances in the use of segmentation algorithms with deep learning applications and new design of microfluidic device have been developed and reported.

4.1 Materials and methods for segmentation algorithm

Cheetah training process Training of the U-Net convolutional neural network was performed using a Dell Precision 5530 laptop (Intel Core i7-8850H CPU, 16 GB RAM, and 512 GB NVMe SSD) running Windows 10 connected to a Sonnet eGFX Breakaway Box 550 hosting an NVIDIA Titan Xp GPU with 12 GB GDDR5X RAM. The set of annotated images was split into training set (70%) and in validation set (30%).

Mammalian cell lines, media, and culture mESCs used were subjected to two rounds of infection and drug selection to stably express the transactivator (EF1a-rtTA, neomycin) and the doxycycline-inducible vector ($pLVX_TRE3GDDmCherry$, puromycin; Addgene plasmid 108679) [12]. mESCs were grown on gelatin-coated dishes in Dulbecco's modified Eagle's medium ($DMEMD5796$, Sigma) supplemented with 15% fetal bovine serum (F7524, Sigma), 1× nonessential amino acids (11140035, Thermo Fisher), 2 mM L−glutamine (25030024, Thermo Fisher), 100 μM 2−mercaptoethanol (31350010, Thermo Fisher), 1 mM sodium pyruvate (11360039, Thermo Fisher), 1× penicillin/streptomycin (P4458, Sigma), and 1000 U/mL LIF (250-02,Peprotech).

Microfluidic device loading and cell imaging The microfluidic device used was designed by Prof. Jeff Hasty [92] and the geometry was described in chapter 5. The chip was pre-filled with mESC media supplemented with 1 $\mu g/mL$ Doxy ($D9891$, Sigma) and 100 nM TMP ($T7883$, Sigma) before the cell loading. After that, cells from a subconfluent Petri dish were washed with sterile phosphate-buffered saline (PBS) ($D8537$, Sigma), trypsinized for 2 to 3 min at room temperature, and centrifuged at 1000 rpm for 5 min, the pelleted cells were resuspended in 200 μL of complete mESC medium + Doxy/TMP and gently loaded using a 2 mL syringe in the device while applying constant vacuum suction. The chip was kept for 24 h in a tissue culture incubator (5% CO2, 37 °C) under constant Doxy/TMP perfusion. The day after, the device was ready for imaging acquisition, it was transferred to the microscope and connected to the actuation system. Time-lapse microscopy was performed using a

Leica DMi8 inverted microscope equipped with an environmental control chamber (PeCon) for long-term temperature control and CO2 enrichment. Imaging was performed using a 20× objective every 60 min. The experimental setup includes consecutive acquisition in three channels (phase contrast, green fluorescence, and red fluorescence).

4.2 Computational toolkit for cybergenetics control

In the literature, different segmentation algorithms have been proposed to automatically analyze images of various organisms and tissues [93],[94]. The most used method to characterize image segmentation is thresholding [95]. Even though commercial software packages are developed to automate image acquisition and analysis, they are often difficult to apply for specific purposes, such as for specific biological processes or cell morphology. The main properties to consider for a segmentation algorithm are accuracy and robustness. Furthermore, the presence of a control algorithm applied in real-time on a specific biological process, aspects such as computational cost and time are relevant too. New computational tools related to deep learning applications can overcome and help to simplify external cybergenetics control applications. Indeed Cheetah, a new flexible computational toolkit, simplifies the integration of real-time microscopy analysis with algorithms for cellular control. Cheetah is able to characterize long-term bacterial and mammalian cell growth by dynamically controlling protein expression.

Cheetah is a Python package designed to support closed-loop control in cybergenetic applications. The toolkit combines real-time image segmentation with image analysis and cellular control algorithms using the U-Net convolutional neural network (CNN). U-Net is a generic deep-learning solution for frequently occurring quantification tasks such as cell detection and shape measurements in biomedical image data [96]. Indeed, U-Net was chosen for segmentation because it has been proven to be reliable for a wide range of applications in systems and synthetic biology. As reported in the literature, deep learning-based image analysis can properly perform segmentation, tracking, and lineage reconstruction [97]. For our applications, Cheetah implemented U-Net using Keras, and to avoid overfitting,

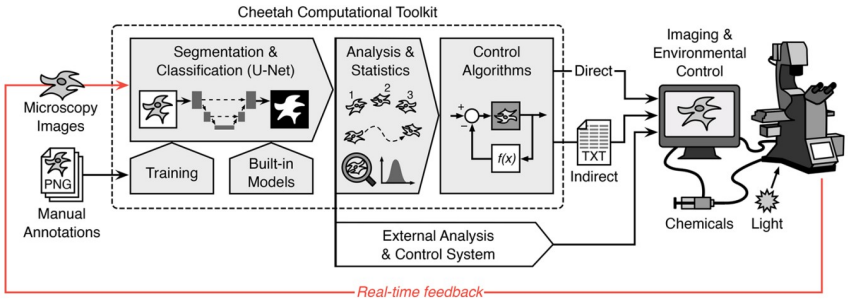

Figure 4.1. Overview of the Cheetah computational toolkit. Structure of Cheetah's core modules and their interactions reported in gray-filled arrows and boxes. Adapted from [15].

regularization can be customized to use either batch normalization.
Cheetah is characterized by four modules as represented in figure 4.1. The first module is based on the generation of training data " Data augmentor". The data set is based on the principle of augmented training sets; it gave an accurate segmentation model to be trained using a small number of manually labeled images. Manual annotations used in the training for each organism were generated by a single person to avoid any differences in cell classifications. The labeled training images then were resampled and manipulated, by sampling subregions of manually labeled images and then randomly applying image rotations, vertical and horizontal flips, scaling and shearing operations, and adjustments to the image histogram to simulate varying illumination levels. The use of these augmented training sets allows an accurate segmentation model. The second module is characterized by an image segmentation process "Segmenter". It divides the image into various classes distinguishing between background and cell (e.g., class 1 = background, class 2 =cell). At this stage parameters for previously trained models are used to predict the class of each pixel in a new image or image stack. The third module process the images by applying analyses such as extraction of pixel-intensity histograms to classify and label separate cells and to track cells across a time series of images. In the end, the fourth module was based on the implementation of user-defined feedback control algorithms such as Relay, Proportional Integral, and Proportional Integral Derivative. This module allowed for continual process images and

generated a control output then used to actuate the experimental setup.

4.2.1 Cheetah experimental implementation

Cheetah is a tool that can be integrated with the microfluidics and imaging platform for external feedback control previously described in chapter 3. It is possible to characterize, describe and implement *in vitro* experiments with species such as bacteria and mammal using Cheetah cybergenetics tools. Hence, for bacteria application, the tool allows identification, isolation, and control of the biological process of interest, and major details on the entire process are reported in [15].
Here, we focused more on the Cheetah's capability to be applied to a complex system such as mouse embryonic stem cells. As well known, there are many challenges to overcome in dealing with mESCs, the most relevant is that their shape can change a lot over time, and there is a higher probability of death during the experiment due to their high sensibility to light exposure. Cheetah toolkit allowed distinguishing, after proper training, between alive and dead cells. This implied a more accurate value of fluorescence intensity which was not affected anymore by cells' viability. In more detail, the training process involved a manual annotation based on human knowledge about the spherical shape of dead cells. The number of 34 large images (1280× 1056 pixels) containing 314 clones in total with each pixel labeled as "background", "cell border", "alive cell interior", or "dead cell interior".
We further validate the toolkit experimentally *in vitro*. First, open-loop and then closed-loop experiments with an engineered mESCs cell line were performed. mESC of interest was modified to carry an inducible dual input genetic construct, where a mCherry fluorescent protein fused to a destabilizing domain (DD) was under the control of a "TetOn" promoter as reported in 4.2. This engineered cell line was previously characterized and described in [12].

Rigorously, an open-loop experiment was performed to assess the Cheetah's performance of cell segmentation. mESCs were exposed to plain or Doxy/TMP supplemented media for the entire duration of the time lapse. Cheetah toolkit measured the average of mCherry expression. To validate our results we compared the performance of cell segmentation and average mCherry fluorescence of Cheetah versus ChipSeg. ChipSeg is a well-

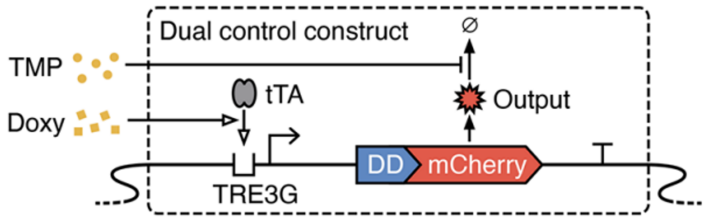

Figure 4.2. Overview of genetic construct of mESCs. Small molecules (TMP and Doxy) work in tandem to boost the expression level of mCherry. Regulation is due to a tetracycline transcriptional activator (tTA) and a destabilizing domain (DD), which forms part of the mCherry reporter protein. Adapted from [15].

known and largely used algorithm in cybergenetics application [12],[24]. As reported in figure 4.3, images were acquired each hour for 29 hours in phase contrast and red fluorescence channel in a selected area shown by the dashed box. Then images were processed with both segmentation algorithms ChipSeg and Cheetah. It is visible that ChipSeg incorrectly segmented the walls of the microfluidic chamber and struggled to precisely isolate cell bodies within the chamber, whereas Cheetah allowed more accurate results in cell body recognition. Indeed, ChipSeg led to a slightly lower estimation of average mCherry fluorescence. Furthermore, Cheetah was allowed to classify alive and dead cells, mCherry fluorescence for living cells was marginally higher than for dead cells.
After Cheetah validation in open-loop, we proceed to design a control experiment to maintain the desired reference value of mCheery fluorescence intensity. The biological system was allowed to switch "on" mCherry reporter by the combined presence of doxycycline (Doxy) and trimethoprim (TMP). We implemented a Relay control strategy. According to the biological system to achieve control drugs such as doxycycline and trimethoprim or plain media were used as external stimuli. In figure 4.4, images in phase contrast and red fluorescence were acquired each hour for 24 hours. In this case, we selected a desired reference average mCherry fluorescence of 10 arbitrary units (a.u.), which was half of the saturating mCherry fluorescence reached overnight and measured during the initialization phase of

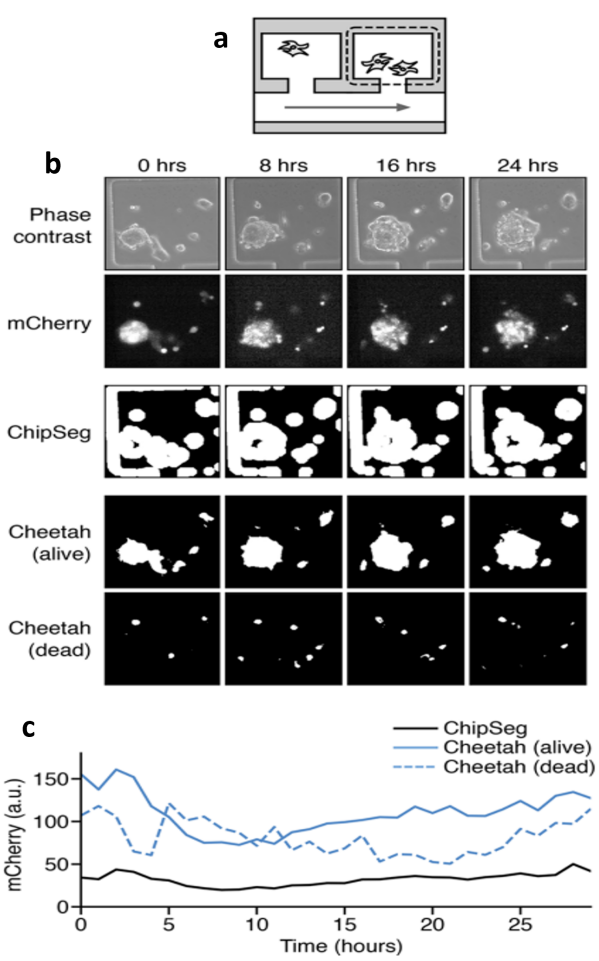

Figure 4.3. Open-loop experiment with Cheetah of mESCs. a) Microfluidic chamber representation used for mouse embryonic stem cell. b) Time-lapse images of mESCs growing in the microfluidic chamber for phase contrast and mCherry fluorescence as well as segmentation masks for cells generated using ChipSeg and Cheetah. For Cheetah, separate masks are shown for living and dead cells. c) The average mCherry fluorescence of the cell segmentation mask over time calculated using either ChipSeg or Cheetah. The Adapted from [15].

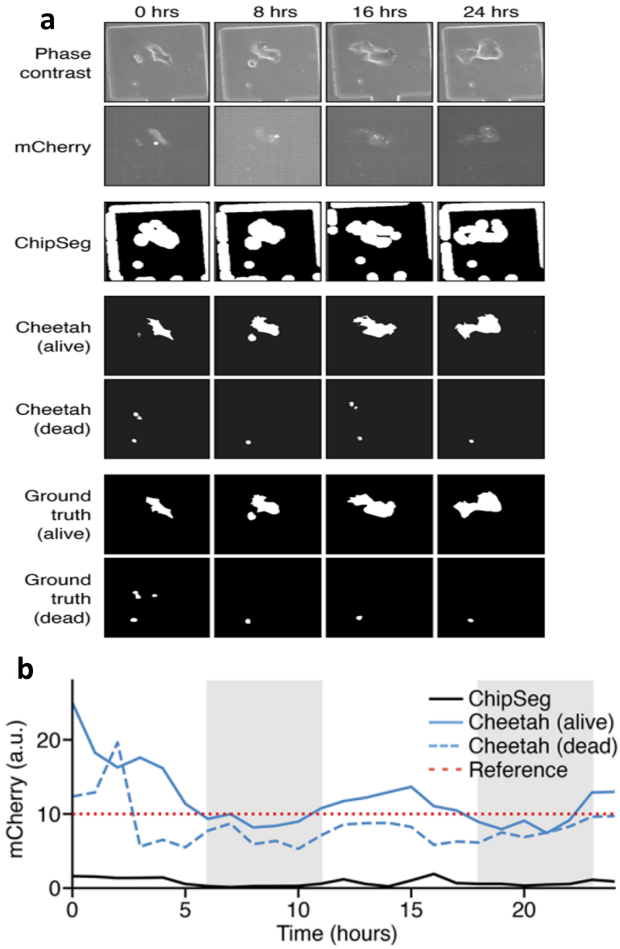

Figure 4.4. Closed-loop control of protein expression in mammalian cells. a) Time-lapse images of mouse embryonic stem cells (mESCs) growing in the system for phase contrast and mCherry fluorescence as well as segmentation masks for cells generated using ChipSeg and Cheetah and manually annotated to give a ground truth (white regions denote cells). For Cheetah and the ground truth, separate masks are shown for living and dead cells. b)) Average mCherry fluorescence of the cell segmentation mask over time calculated using either ChipSeg or Cheetah. Red dotted line denotes the external reference that the controller aims to maintain (10 au). Gray shaded regions show when the control signal triggered the release of TMP and Doxy. Adapted from [15].

120 min. In closed-loop experiment, there was a regulation between the current mCherry fluorescence of the cells and the desired reference value, and based on this value the delivery of chemicals can be adapted. Considering the mask generated by both segmentation algorithms also, in this case, Cheetah was able to recognize the cells in a more robust manner. Furthermore, also the fluorescence estimation confirmed that the average mCherry fluorescence was much lower due to the misclassification of the chamber walls. This error in fluorescence estimation can trigger mistaken control input to our system. Those results underlined the capability to apply Cheetah in real-time experiments with higher performance than another segmentation algorithm. We expect the deep learning methods that are central to Cheetah's capabilities will play an increasingly important role in synthetic biology.

4.3 Materials and methods for the new microfluidic device

Device Fabrication The microfluidic device was fabricated using maskless photolithography. The process can be divided into three main steps: silicon wafer preparation, exposure, and development. Firstly, the preparation consists of a negative photoresist SU-8 2050 (MicroChemicals GMBH, Stuttgart, Germany) applied on a 4-inch silicon wafer spin-coated at 3000 rpm for 30 seconds to achieve a height of 50 µm, and then exposed to the hot plate before at 65 °C for 2 minutes and then at 95 °C for 9 minutes. Secondly, the exposure consists of a baked silicon wafer exposed using a Heidelberg laser writer 'µPG101' (Heidelberg Instruments Mikrotechnik GmbH) using 30 mW of power at 10 %. A post-exposure baking step was performed first at 65 °C for 1 minute and then at 95 °C for 7 minutes. In the end, the development phase consists to immerse the baked wafer in the SU-8 developer solution (MicroChemicals GMBH, Stuttgart, Germany) to remove the access photoresist. Extra hard baking is performed by placing the wafer directly on the hot plate at 200 °C for 10 minutes to enhance the adhesion of structures to the wafer. The final device was obtained by pouring PDMS on the mold with a base-to-curing agent ratio of 10:1. Air bubbles removal was performed in a desiccator for 25 minutes and then baked in the oven at 70 °C for 120 minutes. The baked PDMS mold was

autoclaved to achieve sterilization, and the single device was realized by bonding the PDMS layer on a microscope glass slide (75 mm × 25 mm) using an oxygen plasma machine at 100 % power.

Device and mixing characterization experiments Fluorescence dyes used for the experiments were Atto 488 (41051-1MG-F), Atto 647 (97875-1MG-F), Rhodamine B CAS-81-88-9 and Phosphate-buffer saline (D8537-500 ML) used at a 10 μM concentration. The experimental platform consisted of syringe pumps (World Precision Instruments AL-1000), a DMi8 inverted fluorescence microscope (Leica Microsystems Wetzlar, Germany), and an Andor iXON 897 Ultra back integrated camera. Images were collected to test the efficacy of the device for the media exchange and mixing, and were acquired by using an objective lens of magnification 10x. The media exchange and mixing experiments were 30 minutes long with images recorded every 2 minutes.

Mammalian cell lines, media, and culture mESCs used in this study were two different cell lines already published and largely used, REX-dGFP [98] and MiR-290-mCherry/miR302-eGFP (named here DRC) [99]. mESCs were grown on gelatin-coated dishes in Dulbecco's modified Eagle's medium ($DMEMD5796$, Sigma) supplemented with 15% fetal bovine serum (F7524, Sigma), 1× nonessential amino acids (11140035, Thermo Fisher), 2 mM L−glutamine (25030024, Thermo Fisher), 100 μM 2−mercaptoethanol (31350010, Thermo Fisher), 1 mM sodium pyruvate (11360039, Thermo Fisher), 1× penicillin/streptomycin (P4458, Sigma), and 1000 U/mL LIF (250-02, Peprotech).

Microfluidic device loading and cell imaging The chip was prefilled with mESC media before the cell loading. After that, cells from a subconfluent petri dish (10 cm) were washed with sterile phosphate-buffered saline (PBS) ($D8537$, Sigma), trypsinized for 5 min at room temperature, and centrifuged at 1200 rpm for 5 min, the pelleted cells were resuspended in 100 μL of complete mESC medium and gently loaded using a 2 mL syringe in the device from the outlet port while applying constant vacuum suction at a pressure of -80 kPa. The chip was kept for 5 days in a tissue culture incubator (5% CO2, 37 °C) under constant perfusion, and images

were acquired every 24 hrs using a Leica DMi8 inverted microscope using a 20× objective in the phase contrast channel.

4.4 Development of a single layer microfluidic device

The need for more complex platforms and biological systems to be controlled led to the design of the new microfluidic device. The new device can be implemented and used in the platform described in the chapter 3. The new design is composed of a single-layer microfluidic mixing with vacuum-assisted cell loading systems suitable for mammalian cell culture and dynamic stimulation. Furthermore, the geometry of the chambers allowed a higher number of cells entrapped and the possibility to perform long cell cultures of up to 5 days. The device has promising future applications for open-loop and closed-loop experiments that require a tunable and precise amount of drug concentration to be delivered to the biological system.

4.4.1 Design and fabrication

Dynamic drug stimulation, mixing, and long-term media perfusion were relevant aspects to consider for cell biology applications. The novelty of the new design involved the capability to allow mixing phenomena on a single-layer microfluidic device with vacuum-assisted cell loading systems for mammalian cell culture. In the literature, many microfluidic devices that allowed mixing and drug exchange have been developed but all of them were characterized by a multilayer design and the process of fabrication was more complex than the single layer [100],[101],[102]. For all those reasons, the possibility to design and develop the structure on one single layer is promising and it reduces time and cost in mold development.

The device of interest was made of four inlets connected to a diffusive mixing part, five cell culture chambers (footprint 360 µm × 360 µm and height 50 µm), an output port, and vacuum-assisted cell loading. Due to the independent input ports, four different types of media could be delivered via a syringe pump system. The pumps can be switched on or off according to experimental design and the drugs within the microfluidic

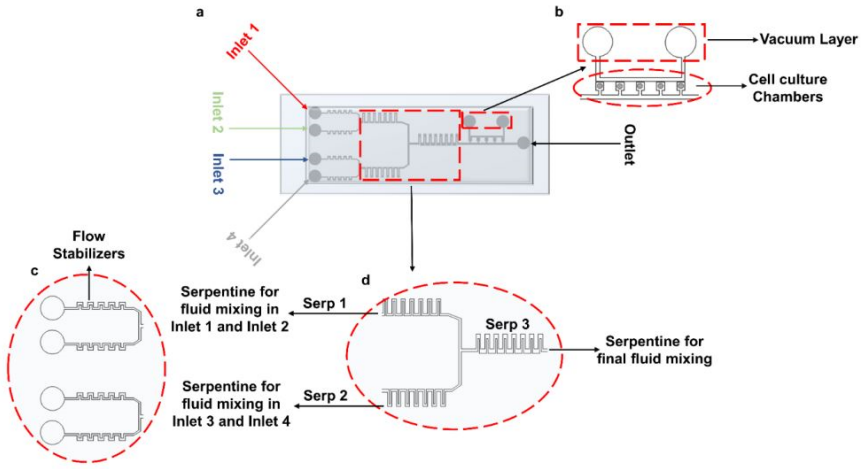

Figure 4.5. Design of microfludic device. Adapted from [16].

device could be mixed at a desired working concentration for the experiment. The media entered the device, crossed the three serpentine structures, that mixed and stabilized the flow, then the flow was delivered inside the microfluidic chambers where the cells were located. A main channel connected the mixing part to the biological system and as a dynamic exchange, the media was moved out via an outlet port connected with an external waste. The distance between the vacuum layer and the trapping chambers was 80 µm, and cells are loaded by applying a vacuum to the vacuum layer. The design was reported in figure 4.5. The production of the microfluidic device was characterized by a maskless photolithography technique with a negative photoresist exposure. Once prepared the baked silicon wafer, the design of the device, generated on computer-aided design software (CAD), was printed by the equipment. The equipment used is a Heidelberg laser writer 'µPG101' (Heidelberg Instruments Mikrotechnik GmbH). After the exposure, the silicon wafer was developed obtaining a mold suitable to do replica molding. The replica molding process was less time and cost-consuming than other approaches or device production that involved the use of material such as PMMA Poly-methylmethacrylate. For our application, we selected the PDMS material to produce our device,

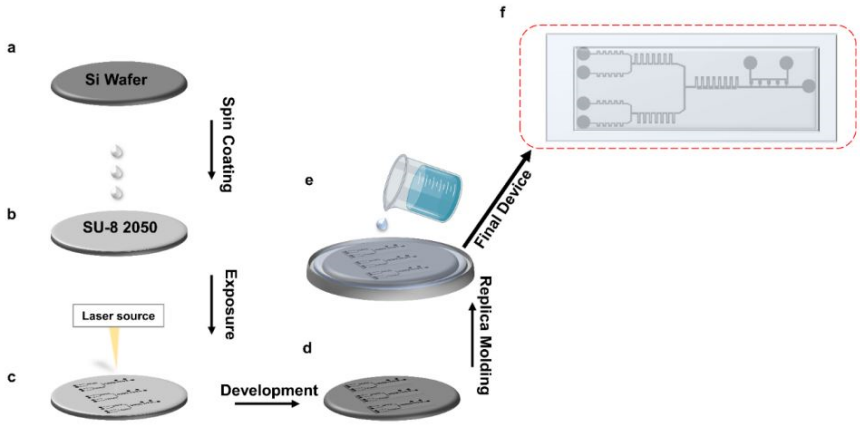

Figure 4.6. Device fabrication protocol. (a) Basic silicon wafer. (b) application of SU-8 2050 negative photoresist. (c) Exposure of the wafer to a laser source. (d) Cleaning and development (e) PDMS replica molding. (f) Final design of fabricated device bonded on a glass slide. Adapted from [16].

then it was bonded on glass and ready to be used for each type of desired application.

4.4.2 Experimental microfluidic device characterization

First, the design functionality was tested *in silico* performing finite element analysis with COMSOL 5.6 Multiphysics software, and then *in vitro* performing experiments using the experimental platform reported in figure 4.7 to test the mixing and cell viability.
In silico modeling gave a better prediction of fluids' behavior. Indeed, computational fluid dynamics (CFD) helped in the design and optimization of microfluidic devices. CFD model was based on solving fluid flow by using a laminar form of the Navier-Stokes equation and modeling transport mechanisms using mass transport equations. At the inlets fully developed flow boundary condition was used whereas at the outlet boundary condition was set to be zero pressure.
Once obtained promising results from the simulation, the next steps to characterize was device production and experimental validation. The ex-

perimental approach was possible with the same platform described in chapter 3 but in this case, the external actuator was not anymore made of actuators on motorized linear rails that use hydrostatic pressure, but was made of syringe pumps that deliver the external media inside the microfluidic device. The syringe pumps delivered the media using controlled software, and each pump could be ruled in an independent way. The experimental schema with the new pump was reported in figure 4.7. It consisted of an inverted fluorescence microscope with an integrated camera that allowed device and cell imaging.

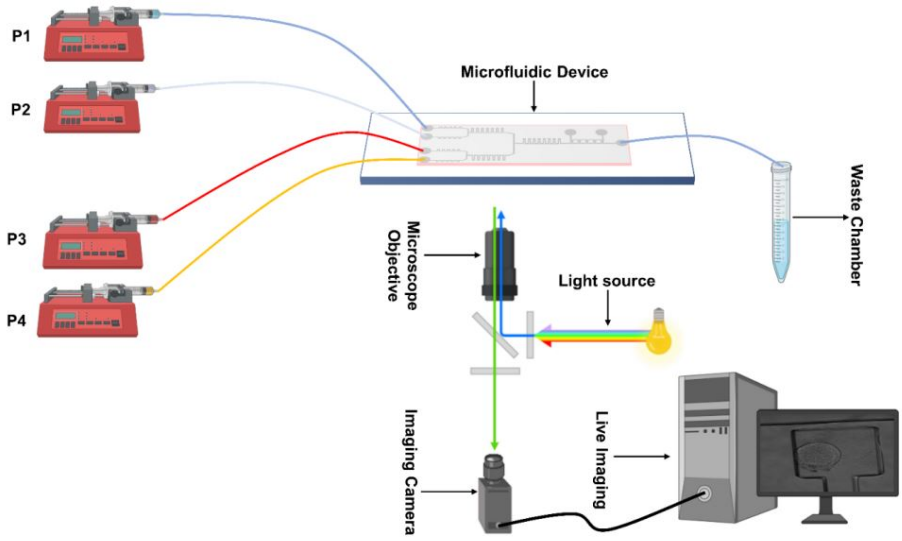

Figure 4.7. Experimental setup using the new design. Adapted from [16].

Hence, *In vitro* a batch of experiments was performed. The device allowed media exchange and media mixing with 4 or 2 inputs of media delivered.
First of all, the possibility to use 4 independent inputs to achieve mixing was tested. Each syringe was enriched with 4 different fluoresce dyes: Atto 488, Atto 647, Rhodamine B, and Phosphate-buffer saline, and located on the syringe pumps (World Precision Instruments AL-1000) for media de-

livery. The syringe was ruled by a customized Matlab code to guarante the switch on/off and changed flow rates during experiments. The fluid variation required a balance of the flow rates in the main junction avoiding any backflow from the inlets. The image acquisition over time with different color channels allowed to get information and confirm the ability of the device to achieve mixing in one single-layer design using serpentine structures when all the pumps are switched on. The data reported in the figure 4.8 confirmed the results for both applications *in silico* and *in vitro*. Furthermore, the device was tested in the case of only two inputs delivered and the other two closed as reported in the 4.9. The fluorescence dyes used were Atto 488 and Rhodamine B. In this case, the simulation and the experiments show that the rectangular serpentine structures acted as effective micromixers for two inputs.

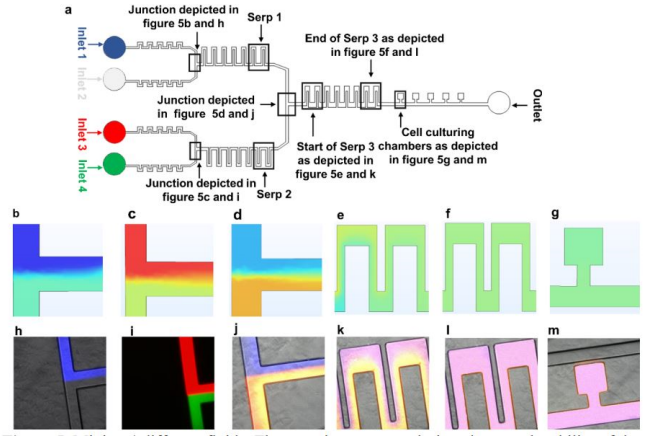

Figure 4.8. *In silico* and *in vitro* characterization of a microfluidic device with 4 inputs for mixing experiment. Mixing experiments were obtained with serpentine structures. (a) Microfluidic device design. (b-g) COMSOL simulation depicting diffusion-based mixing of four fluids. (h-m) Experimental results for static mixing at 50 µl/hr. Adapted from [16].

Furthermore, in the presence of 4 inputs was also tested the capability of the dynamic media exchange of the device. The experiment was designed in a way that the syringes containing ATTO 488 and Rhodamine B were always kept with the pumps switched on at 50 µl/hr whereas the syringe

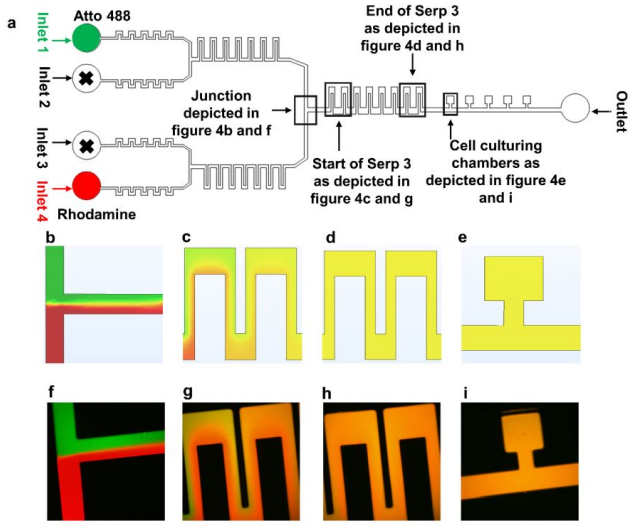

Figure 4.9. *In silico* and *in vitro* characterization of microfluidic device with 2 inputs for mixing experiment. Mixing experiments obtained with serpentine structures.(a) Microfluidic device design. (b-e) COMSOL simulation depicting diffusion-based mixing of two fluids. (f-i) Experimental results for static mixing at 50 µl/hr. Adapted from [16].

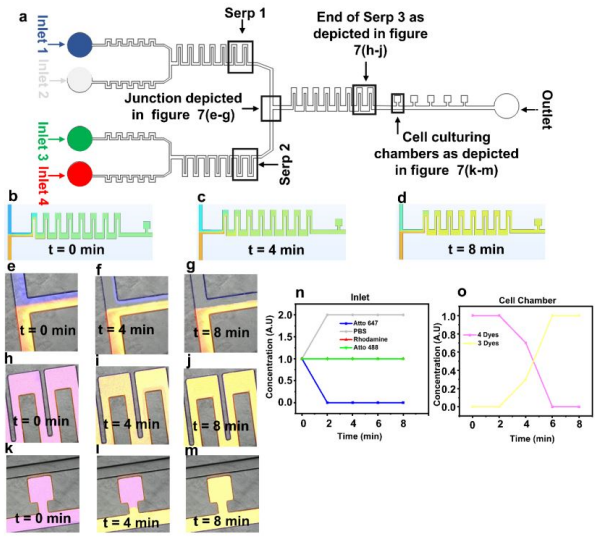

Figure 4.10. ***In silico*** **and** ***in vitro*** **characterization of microfluidic device with 4 inputs for media exchange.** Media exchange experiments were obtained with serpentine structures. (a) Microfluidic device design. (b-d) COMSOL simulation for media exchange of four fluids. (e-m) Experimental results of media exchange in time. The blue dye was switched off at t=0 min and the flow rate for PBS was increased to 100 µl/hr. (n-o) Time vs concentration plots at the inlet junctions (n) and cell culture chambers (o). [16].

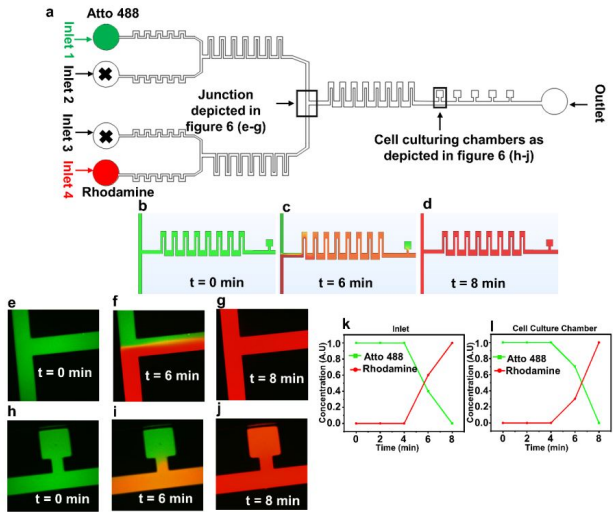

Figure 4.11. ***In silico* and *in vitro* characterization of microfluidic device with 2 inputs for media exchange.** Mixing experiments were obtained with serpentine structures. (a) Microfluidic device design. (b-e) COMSOL simulation depicting diffusion-based mixing of two fluids. (f-i) Experimental results for static mixing at 50 µl/hr. Adapted from [16].

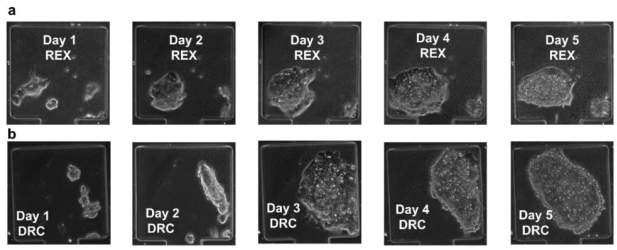

Figure 4.12. mESCs cultured inside the microfluidc device. Cell viability tests for REX-dGFP2 (a) and MiR-290- mCherry/miR302-eGFP (b) up to 5 days. Images acquired every 24 hrs. Adapted from [16].

containing Atto 647 was switched off and Phosphate-buffer saline flow rate was increased to 100 µl/hr. This permitted to the balance the fluidic inside of the device and in both cases, computational and experimental, media exchange happens in a range of 8 min as reported in figure 4.10. In addition, media exchange was also tested with the two inputs. In this experiment initially, the pump controlling the syringe with the ATTO 488 was switched on at 50 µL/hr and the pump controlling the Rhodamine B syringe was switched off. After 4 min the on/off condition was inverted and after 2 min Rhodamine B started to take over the ATTO 488 in the device. Quantification of the fluorescence signals confirmed successful media exchange, with a short time delay between pumps' switching and complete change of dye in the cell culture chambers as reported in the figure 4.11. Furthermore, the capability to load and grow cells inside the new device was characterized. We investigate the cells viability of mESCs, in particular, we use two different cell lines REX-dGFP [98] and MiR-290-mCherry/miR302-eGFP (named here DRC) [99]. Cells were loaded inside the device with a vacuum-assisted system and growth inside the incubator for up to 5 days. Images are reported in the figure 4.12.

4.5 Discussion

In this chapter, we reported the possibility to create cybergenetics tools that combine computational, physical, and biological elements to allow us to control more complex biological processes. We investigated the developments considering two aspects computational and experimental.
From a computational point of view, Cheetah was an easy-to-use computational toolkit that was flexible to the new questions that come from the scientific field. It was a suitable computational framework that combines both robust U-Net image segmentation with analysis functions. It had the ability to rapidly segment and classify morphologically different cell types overcoming some computational limitations for control experiment applications. However, new features could be easily integrated into the code to satisfy more sophisticated control strategies, and the possibility to add tracking events could be disruptive for further applications.
From an experimental point of view, the design of a new microfluidic device as a single-layer that combines a passive microfluidic micromixing

mechanism suitable for long-term mammalian cell culture can find different applications such as complex combination drug delivery experiments or control experiment applications. Besides, a possible extension of this work could be a further development of a microfluidic device that allows 3D structure for tissue development. Hence, both tools can find large applications in the cybergenetics field.

Chapter 5

Automatic feedback control of stem cells fate

In this chapter, I am going to present the main work, of my entire contribution, developed during my Phd on mouse embryonic stem cells.

Mouse embryonic stem cells were isolated for the first time in 1981 by Evans and Kaufman [49],[50]. mESCs can exist in different pluripotency states. Pluripotent stem cells are unspecialized cells owning two properties: they can be indefinitely expanded retaining pluripotency or pushed into specific differentiated states by proper stimuli [45],[46]. Both *in vivo* and *in vitro*, different pluripotent stages correspond to different degrees of cell specialization [53],[103].
Naive and primed pluripotency define the preimplantation (mouse embryonic day E3-E4.5) and postimplantation (E6.5) epiblast [57]. The transition from naıve to primed pluripotency requires the progressive switching-off/on of pluripotency and differentiation genes. *In vitro* mESCs are suitable tools to study pluripotency. In particular, focusing on the naıve and primed states they offer the capability to study how the tuning of media components can finely regulate the pluripotent spectrum [17]. There are well-defined protocols to culture mESCs but the most used are still 2i and 2i+LIF. For those reasons we decided to focus our attention on those media investigations because it is generally believed that the best media conditions to maintain a naive state in mouse embryonic stem cells

are composed of all those drugs CH, PD and LIF [104],[42],[105]. As a matter of fact, PD and CH act on MEK/ERK pathway and glycogen synthesis kinase-3 (GSK3) pathway. CHIRON closely mimics WNT signaling by inhibiting GSK3. FGF signaling activates the MAPK pathway leading to phosphorylation of MEK, which in turn phosphorylates and activates ERK. Activated ERK promotes transition to "a primed" state, which is blocked by the MEK inhibitor PD [59]. Besides, LIF signaling affects many pathways but primarily acts via JAK-mediated phosphorylation of STAT3, which activates Tcfp2l1 and Klf4 [106]. LIF has antagonistic effects in different cell types, including stimulating or inhibiting cell proliferation, differentiation, and survival and it has been fully demonstrated that LIF is an important supplement for ESC self-renewal and pluripotency.
In literature, it has been reported that the combination of any two of these three supplements was sufficient to maintain naive self-renewal of ESCs [107]. However, extended culture of pluripotent cells in 2i+LIF compromises their epigenetic and genomic stability as well as their developmental potential [62] . Cells with the same genetic background and with the same culture conditions for long-term, in presence of all the inhibitors can cause genomic abnormalities. Indeed, it has been reported that prolonged culture of male mouse ES cells in 2i+LIF resulted in irreversible epigenetic and genomic changes that impaired their developmental potential [61]. Those problems are mostly associated to presence of PD drug. Inihibition of Mek1/2 is responsible for these effects because cause the downregulation of DNA methyltransferases and their cofactors. To solve those problems a modulation of its concentration has been done or a replacement of the Mek1/2 inhibitor with a Src inhibitor over the years. Besides, Bao et al. showed that LIF alone is capable of supporting ESCs for self-renewal and proliferation over p40 [108].
On the basis of all those knowledge, we developed a new culture protocol for long-term culture of mouse embryonic stem cell where we reduced the exposure of PD drug. Furthermore, in this chapter, we also investigated the possibility to characterize the biological system of mouse embryonic stem cells as a dynamic system with flow cytometry techniques and cybergenetic tools. Open-loop and closed-loop experiments were performed using the microfluidic-microscopy experimental platform to characterize and control the biological system.

The possibility to control mouse embryonic stem cells in the pluripotency spectrum automatically, playing with different external drug perturbations in real-time with a controller is a promising result for further investigation of specific biological pathways of interest or cell fate regarding the developmental stage. In addition, the introduction of our new protocol, based on an alternate presence of drugs inserted in the media, can allow long-term culture and probably reduce the current limitations due to the long exposure of mouse embryonic stem cells to drugs involved to maintain pluripotency in the dishes.

5.1 Materials and Methods

Mammalian cell lines, media, and culture mESCs used in this work are REX-dGFP generated by Smith et al. [98]. The culture used for continuous growth is serum-based. Indeed, mESCs were grown on gelatin-coated dishes in Dulbecco's modified Eagle's medium ($DMEMD5796$, Sigma) supplemented with 15% fetal bovine serum (F7524, Sigma), 1× nonessential amino acids (11140035, Thermo Fisher), 2 mM L−glutamine (25030024, Thermo Fisher), 100 μM 2−mercaptoethanol (31350010, Thermo Fisher), 1 mM sodium pyruvate (11360039, Thermo Fisher), 1× penicillin/streptomycin (P4458, Sigma), and 1000 U/mL LIF (250-02, Peprotech). The culture used to perform experiments is serum-free. We tested the two serum-free cultures 2i and 2i+LIF respectively. To note, for the 2i+LIF culture, cells were kept for 2-3 passages (around 6-10 days) in serum-free NDiff227-based media supplemented with 1000 U/mL LIF, 3 μM of the GSK-3a/b inhibitor Chiron-99021 (CH) and 1 μM of the MEK inhibitor PD0325901, and for the 2i culture cells were kept for 2-3 passages (around 1 week) in serum-free NDiff227-based media supplemented with 3 μM of the GSK-3a/b inhibitor Chiron-99021 and 1 μM of the MEK inhibitor PD0325901.

Mammals microfluidic device: design Even though mammalian cells are more sensitive to small changes in pH, shear stress, and other external factors than simpler organisms such as yeast and bacteria, new microfluidic application pop up from the literature for mammals applica-

tions too. Indeed specific devices have been developed to perform *in vitro* experiments with mammal cells. One of the most interesting for our purpose is described in [92] and the design of the microfluidic device is reported in figure 5.1. The device is composed of 7 ports, a dial-a-wave junction (DAW), a staggered herringbone mixer (SHM), a vacuum channel, and 33 individual culture chambers. The port 6 and 7 are used as inlets and the flow from the inlets converges in a ratio dependent on the inlet pressure. In the DAW figure 5.1.B, the middle channels of the junction leading to the cell chambers while the two outer are connected to port 5, the shunt waste port. The staggered herringbone mixers (SHM) immediately follows the DAW junction, and it enhances the diffusive mixing of the combined laminar flow streams before the fluid reaches the main perfusion channel and the culture chambers. A high number of cells can be entrapped into the different chambers (230 μm by 230 μm footprint, 40 μm height) via port 1 and by applying temporary vacuum pressure to the vacuum channel, from ports 3 and 4, located parallel to the column of the culture chambers at a distance of 160 μm.

Microfluidic device production and loading Microfluidics devices were fabricated with a replica moulding technique, where the master-mould was produced using multilayer soft-lithography with SU-8 as photoresist, and exposed to vapors of chlorotrimethylsilane (CARLO ERBA Reagents) for 5 min. Polydimethylsiloxane (PDMS; Sylgard 184, Dow Corning) was poured on the top of the master mold with a 1:10 ratio (curing agent to base; w/w) and cured at 80 °C for 2 hrs. Next, the PDMS layer was cut and peeled from the master mould and inlet ports were pierced with a micro-puncher (0.75 mm; World Precision Instruments) and then irreversibly bonded to a cover glass (thickness no. 1.5; Marienfeld Superior) through a plasma treatment for 30 s in a low-pressure plasma machine (ZEPTO version B; Diener electronic). The bonded device was baked for 1 hrs at 80 °C, and then stored at 4 °C until use.
To load the microfluidic device first of all, the chip was pre-filled with mESC serum-free media 2i or 2i+LIF before the cell loading. After that, the media from a p60 subconfluent Petri dish of mESCs was collected and centrifuged at 1200 rpm for 5 min, whereas the cells still attached were trypsinized for 5 min at room temperature, and it was collected and mixed

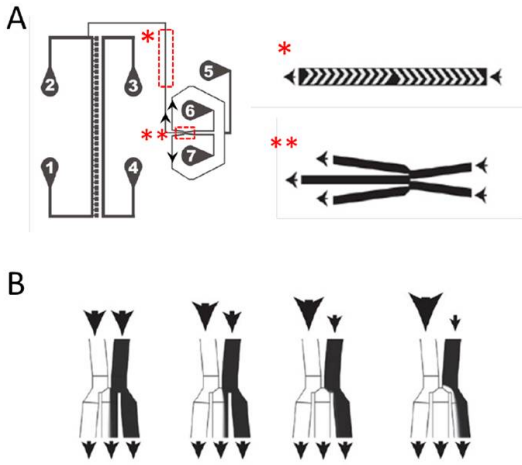

Figure 5.1. Overview of the design of microfluidic device. (A) Design of the mammal microfluidic device. The flow direction is indicated by the black arrows. (B) DAW junction. The ratio between the inputs ports 6 and 7 is determined by each port's pressure. Adapter from [92].

with cells collected from the centrifugation. After 5 min the cells were filtered with a 40 μm and centrifuged at 1200 rpm for 5 min. At this stage the pelleted cells were resuspended in 50 μl of mESC medium 2i or 2i+LIF and loaded using a 2 mL syringe into the main channel of the device from port 2 and a vacuum is applied in the channel adjacent to the culture chambers (ports 3 and 4) to evacuate air and replace the chamber volume with fluid containing cells. The remaining untrapped cells in the main channel are washed away at a high flow rate without disturbing cells inside the traps. Then, the chip was kept for 24 h in a tissue culture incubator (5% CO2, 37°C) under constant 2i or 2i+LIF media perfusion connected to port 5 and the waste medium is washed trough port 1, while all the other ports (2, 6 and 7) are plugged. The day after, the device was ready for imaging acquisition. The fluidic connections from the ports of the device to syringes containing growth medium are then established using 24 gauge PTFE tubing (Cole-Parmer Inc.) interfaced via 22 gauge stainless steel luer stub pins. The device was secured on the microscope

stage within an environmental chamber maintained at 37°C with humidified 5% CO2 and 50 ml syringes were connected to its ports and hung at different heights, in order to regulate the flow from the inlets (ports 6 and 7) to the outlets (ports 5, 1 and 2) according to hydrostatic pressure. The syringes connected to the outlet port contain 12 ml of standard complete culture medium and they serve as a waste tank. The syringes connected to the inlets port were filled with 2i and Ndiff227 respectively for the 2i condition, and with 2i+LIF and Ndiff227 for 2i+LIF media. The correct functioning of the media delivered is checked by inspecting the red fluorescence emitted by Sulforhodamine as a result of the automatic height control of syringes.

Microscopy images acquisition and processing Time-lapse microscopy was performed using a Leica DMi8 inverted microscope equipped with an environmental control chamber (PeCon) for long-term temperature control and CO2 enrichment and an Andor camera iXON 897. Imaging was performed using a 40× objective every 60 min. The experimental setup included consecutive acquisition in three channels (phase contrast, green fluorescence, and red fluorescence).
For image analysis, we used an image processing algorithm that is not based on cells' morphological features but exploits the property of cells to exhibit a white halo in Phase contrast image. First, the image analysis algorithm defined a threshold to generate a first binary image selecting only pixels belonging to cells' edges; then it obtained a second binary image (mask) in which the cell area is overestimated by using dilation and filling operators; and by subtracting the data obtained from the mask with the one of the previous point, it derived a binary image that selected the portion of the original image covered by cells. Finally, the binary filter obtained is applied to the green field image to calculate the average intensity fluorescence of pixels belonging to cells, subtracting the background signal.

Flow cytometry mESCs were cultured for 6-10 days in 2i or 2i+LIF media. The cells were seeded in a 12-well plate coated with gelatin. The samples were analyzed at the flow cytometer day by day, and for day 1 and day 2, 300000 cell/cm^2 were plated whereas for day 3 and day 4, 150000 ell/cm^2. In detail, for 2i media from naive to primed the cells in

the 12-plate were seeded in Ndiff with the absence of CH and PD, whereas for the primed naive transition the cells were seeded with the presence of CH and PD starting from cells cultured for 3 days in Ndiff and previously culture 1 week in 2i+LIF or 2i. In addition for the 2i+LIF media naive primed transition the cells in the 12-well were seeded in Ndiff media with the addition of LIF.
To process mESCs samples via flow cytometer, the media was collected and insert in a tube, then 100 μl of trypsin was added in the 12 well and waited 5 min. Then the trypsin from the dish was added to the media collected and centrifuge for 5 min at 12000 g. Then pelleted cells were resuspended in 200 μl of PBS (PBS, Sigma) and DAPI and processed the samples via flow cytometry. The GFP positive fraction was sorted from DAPI negative using the BD Fortessa X-20.

New protocol: mESCs culture mESCs were adapted from 1 week in a naive state with 2i+LIF media and then alternate at each passage for 2 months in absence or presence of drugs. The dishes were coated with gelatin.
2i+LIF media was composed by Ndiff227 basal media with the addition of Chiron-99021 (CH) at the concentration of 3 μM, PD0325901 1 μM and LIF 1 μM.
The culture media tested were Ndiff+CH+LIF, for simplicity called CH+LIF, composed of the basal media Ndiff227, Chiron-99021 (CH) at the concentration of 3 μM and LIF 1 μM, and Ndiff+LIF, for simplicity called LIF composed of the basal media Ndiff227 and LIF 1 μM.
For example, at each passage for the condition Ndiff+CH+LIF, we alternate this media with the 2i+LIF that differs from Ndiff+CH+LIF for the prensece of PD0325901 at the concentration of 1 μM, whereas for Ndiff+LIF, at each passage we alternate this media with the 2i+LIF that differs from Ndiff+LIF for the presence of PD0325901 1 μM and Chiron-99021 (CH) at the concentration of 3 μM.

New protocol: flow cytometry We tested samples via flow cytometry, we collected mESCs samples from a 12-well plate with gelatin coating at high and low passages. First of all, the media was collected and inserted in a tube, then 100 μl of trypsin was added in the 12-well and waited 5

min. Then the trypsin from the dish was added to the media collected and centrifuged for 5 min at 12000 g. Then pelleted cells were resuspended in 200 μl of PBS (PBS, Sigma) and DAPI and process the samples via flowcytometer. The GFP positive fraction was sorted from DAPI negative using the BD Fortessa X-20.

Rna extraction We tested mESCs culture with the new experimental protocol for gene expression with RNA extraction. mESCs were collected from a confluent 6-well plate with gelatin coating cultured in the respectively desired media. To eliminate the contamination from genomic DNA, the RNeasy Plus Mini Kit (Qiagen) was used to purify the total RNA used for the RNA Sequencing.

Library Preparation Total RNA was quantified using the Qubit 2.0 fluorimetric Assay (Thermo Fisher Scientific). Libraries were prepared from 125 ng of total RNA using the 3'DGE mRNA-seq research grade sequencing service (Next Generation Diagnostics srl) 1 which included library preparation, quality assessment and sequencing on a NovaSeq 6000 sequencing system using a single-end, 100 cycle strategy (Illumina Inc.)

Bioinformatic workflow The raw data were analyzed by Next Generation Diagnostics srl proprietary 3'DGE mRNA-seq pipeline (v2.0) which involves a cleaning step by quality filtering and trimming, alignment to the reference genome and counting by gene [109], [110],[111]. The raw expression data were normalized, analyzed and visualized by Rosalind HyperScale architecture(OnRamp BioInformatics, Inc.) [112].

QuantSeq 3' RNA sequencing data processing and analysis Data of RNA sequencing were analyzed by ROSALIND®, with a HyperScale architecture developed by ROSALIND, Inc. (San Diego, CA). Individual sample counts were normalized via Relative Log Expression (RLE) using DESeq2 R library [112]. Read Distribution percentages, violin plots, identity heatmaps, and sample MDS plots were generated as part of the QC step. DEseq2 was also used to calculate fold changes and p-values and perform optional covariate correction. Clustering of genes for the final heatmap of differentially expressed genes was done using the PAM

(Partitioning Around Medoids) method using the fpc R library. Hypergeometric distribution was used to analyze the enrichment of pathways, gene ontology, domain structure, and other ontologies. The topGO R library [113], was used to determine local similarities and dependencies between GO terms in order to perform Elim pruning correction. Several database sources were referenced for enrichment analysis, including Interpro, NCBI, MSigDB6, REACTOME [114], WikiPathways [115]. Enrichment was calculated relative to a set of background genes relevant for the experiment.

5.2 Mouse embryonic stem cells

An engineered mouse embryonic stem cell line was selected from the literature. We selected this line generated in Austin Smith laboratory [98]. We used the mESC line containing a Rex1-GFPd2 reporter as reported in figure 5.2. It is characterized by the modification of one allele of the Rex1 coding sequence replaced with the coding sequence of a destabilized green fluorescent protein (GFP). GFP is a fluorescent reporter with a relatively short half-life of 2 hours, whereas Rex1 gene is a pluripotency marker for stem cells and it is regulated by Nanog transcriptional regulators of pluripotency [116].

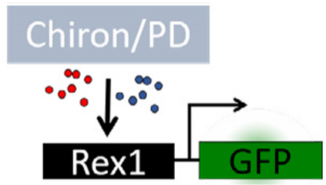

Figure 5.2. mESCs engineered cell line. mESCs carrying a mono-allelic GFP knock-in at the Rex1 locus. Adapted from [117].

Rex1 gene expression has been noted to fluctuate, with a multimodal distribution observed in conventional serum/LIF culture conditions. Rex1 fluctuations and heterogeneity were reduced by the addition of the two inhibitors Chiron (CH) and PD in serum-based and in serum-free culture.

[118],[119]. The presence of specific culture conditions allows to keep cells in a naïve/pluripotent state or push them into a primed/differentiated one. Currently, the most used culture conditions that allow the naïve state are 2i and 2i+LIF composed of specific drugs such as PD, CH and LIF which act on biological pathways. In conclusion, the addition or withdrawal of specific drugs could tune the pluripotency spectrum transition between naive to primed state.

5.3 Experimental set-up to track pluripotency transition

First of all we have to select which culture conditions to analyze and from the different media reported in the literature we selected a serum-free based media and specifically we investigate the characterization of mESCs in 2i and 2i+LIF media.
2i media is composed by a basal media called NDiff227 supplemented with two specific drugs CH and PD. 2i/LIF is characterized with the same components, plus the presence of Leukemia inhibitory factor. Secondly, we developed a microfluidic experimental protocol to monitor stem cell transition in time. The specific pipeline is reported in figure 5.3. Starting from mESCs cultured in serum-based media, we adapt the cells to the serum-free culture 2i or 2i+LIF for 6 to 10 days. Then the cells are ready to load and grow in the microfluidic device. The device is kept in the incubator at 37 °C and 5% $C0_2$ overnight. Once tested the viability and feasibility of culture mESCs in the microfluidic device, the cells were ready for imaging. We designed and performed specific experiments to characterize the pluripotency spectrum transition from naive to primed in mESCs using the cybergenetics tools. In detail, we used the experimental platform reported in chapter 3 that could precisely manipulate culture conditions while measuring gene expression.

5.3.1 Open-loop microfluidic characterization

Once tested the possibility of growing mESCs in serum-free culture in the microfluidic device, we decided to perform open-loop experiments to test the feasibility to monitor in real-time the pluripotency spectrum tran-

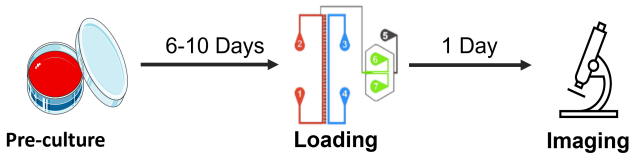

Figure 5.3. Experimental scheme for microfluidic-based monitoring of cells pluripotency. mESCs are pre-cultured in serum-free culture 2i or 2i+LIF for 6-10 days, then mESCs are loaded in the device and after an overnight in the incubator is ready for imaging.

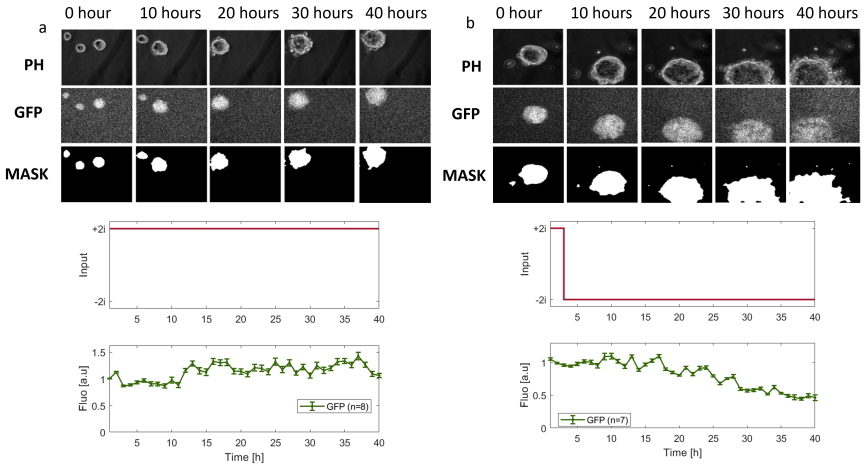

Figure 5.4. Characterization and open-loop control of mESCs in the absence of 2i media. Time-lapse images of mESCs grown in the microfluidic chamber for phase contrast (PH), green fluorescence protein (GFP), and segmentation mask generated using the Otsu method (MASK). Cells were imaged with a sampling time of 1 hour. The green line represents the averaged GFP fluorescence with the relative standard deviation error measured from the cells segmentation mask calculated over time across the chambers (n=8 in a and n=4 in b), whereas the red line represents the media received from the cells at each time point. In a) we test the constant presence of both inhibitors CH and PD (+2i) whereas in b) the constant absence (-2i). Here, the cells were adapted in 2i for a calibration phase of 3 hours, and then we removed CH and PD.

sition. The platform allowed to acquire the changing behavior of mESCs in real time via image acquisition. The images were acquired at a specific time point and we measured as output information the intensity of fluorescence as an indicator of gene expression for pluripotency behavior.
Firstly, we investigated the pluripotency spectrum transition with 2i media. We performed two experiments. For the first one, starting from cell cultured in 2i media for 1 week, we characterized mESCs cell line when the constant presence of the drugs (+2i) was delivered. The experiment was reported in figure 5.4. We acquired images with the microscope in the two different channels phase contrast and green fluorescence channel. The images were acquired each hour for up to 40 hours. Then, the images were post-processed with Otsu algorithm able to generate the relative Mask of interest at that specific time frame to quantify gene expression. The input, reported with a red line, is the external perturbation (i.e the media delivered) acting on the mESCs. In this case, we perturbed the system with the Ndiff227 basal media with the constant presence of CH and PD (+2i). The fluorescence, reported with a green line in the arbitrary unit [a.u], is the quantification of the green fluorescence protein over time averaged across the number of chambers ($n = 8$). The number of chambers was not constant among the different experiments performed due to the high variability to entrap cells in the specific chambers.
Hence, the microfluidic-experimental platform allowed monitoring in real-time of naive state of pluripotency, indeed in the case of constant delivery of the drugs, CH and PD, the reporter showed an almost constant behavior (green line).
After this preliminary result, we also investigated mESCs with another external perturbation. Starting from mESCs cultured in 2i media for 1 week, we characterized mESCs cell line when the constant absence of the drugs (-2i) was delivered. Before to perturb the system with (-2i) media, we kept the cells in a calibration phase of 3 hours in (+2i) media. The experiment was reported in figure 5.4. The images were acquired as reported previously, but in this case, we perturbed the system with the Ndiff227 basal media with the constant absence of CH and PD. The fluorescence, reported with a green line in the arbitrary unit [a.u] was the quantification of the green fluorescence protein over time averaged across the number of chambers ($n = 7$). In the case of the absence of drugs as CH and PD

in the media, the reporter showed a decreasing behaviour (green line) as indication that mESCs felt drugs perturbation in a microfluidic device and we were able to follow in real-time pluripotency dynamics.
We concluded that we could perturb pluripotency in mESCs with drugs, that acted on specific pathways, with addition and withdrawal. For the 2i media characterization, the constant presence of drugs could be seen as an "ON" behavior of the system (i.e. the system is able to maintain the naive state) whereas the constant absence as "OFF" behavior (i.e. the system feels drugs perturbation and was pushed to the primed spectrum of pluripotency).
Furthermore, we investigated the 2i+LIF media behavior. We performed two experiments. For the first one, starting from cell culture in 2i/LIF, we characterized mESCs cell line when the constant presence of the drugs PD, CH and LIF were delivered. The experiment was reported in figure 5.5. We acquired images in PH and GFP channels each hour for up to 30 hours. The images were post-processed with Otsu algorithm. The input, reported with a red line, is the external perturbation (i. e. the media delivered) acting on the mESCs. In this case, we perturbed the system with the Ndiff227 basal media with the constant presence of CH, PD and LIF. The fluorescence, reported with a green line in the arbitrary unit [a.u], is the quantification of the Green Fluorescence Protein over time averaged across the number of chambers ($n = 8$). The microfluidic-experimental platform allowed monitoring in real-time state of pluripotency, indeed in the case of constant delivery of the drugs, CH, PD and LIF, the reporter showed almost constant behavior (green line).
Then, we ran another experiment starting from cell cultured in 2i+LIF media for 1 week, we characterized mESCs cell line when the constant absence of the drugs PD, CH and LIF was delivered. The experiment was reported in figure 5.5. The images were acquired each hour for up to 40 hours in PH and GFP channels, and post-processed with Otsu. In this case, we adapted the cells in a calibration phase of 3 hours in presence of drugs and then perturbed the system with the Ndiff227 basal media with the constant absence of CH, PD and LIF. The fluorescence, reported with a green line in the arbitrary unit [a.u], is the quantification of the green fluorescence protein over time averaged across the number of chambers ($n = 4$).

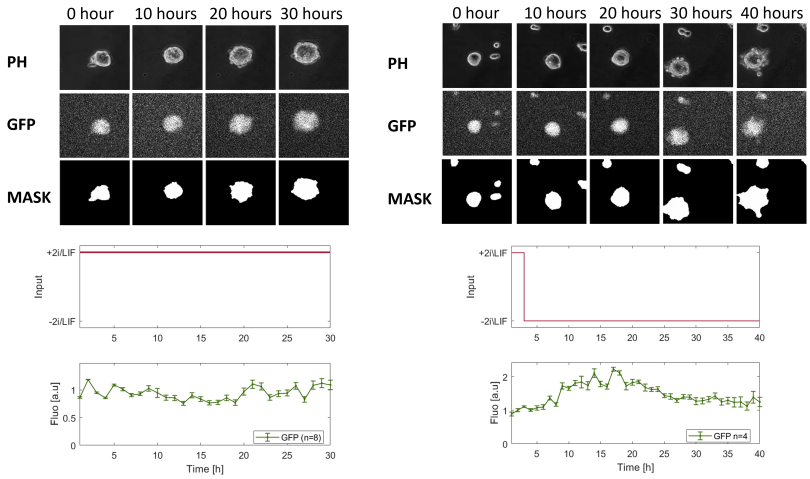

Figure 5.5. Characterization and open-loop control of mESCs in the absence of 2i+LIF media. Time-lapse images of mESCs grown in the microfluidic chamber for phase contrast (PH), green fluorescence protein (GFP), and segmentation mask generated using the Otsu method (MASK). Cells were imaged with a sampling time of 1 hour. The green line represents the averaged GFP fluorescence with the relative standard deviation error of the cells segmentation mask calculated over time across the chambers (n=8 in a and n=4 in b), whereas the red line represents the media received from the cells at each time point. In a) we test the constant presence of both inhibitors CH and PD (+2i) whereas in b) the constant absence (-2i). Here, the cells were adapted in 2i for a calibration phase of 3 hours and then perturbed with CH and PD withdrawal. In a) we test the constant presence of inhibitors CH, PD, and LIF (2i+LIF) whereas in b) the constant absence (-2i+LIF). Here, the cells were adapted in 2i+LIF for a calibration phase of 3 hours and then we removed CH, PD, and LIF.

Even though mESCs were perturbed by drug withdrawal and the system felt the perturbations, at the same time, the dynamics with 2i+LIF media were slower than 2i media.
In conclusion, we summarized that from the characterization of this open-loop experiments mESCs could maintain constant expression of GFP in presence of drugs, whereas a decreasing behaviour in absence. However for the following experiments which were closed loop, we decided to focus on LIF free media to avoid undesired delay in drug response.

5.3.2 Model-free external feedback control of stem cell identity

One of the most used model-free negative feedback control is the Relay. The relay system theory has constantly received a lot of attention since the 1950s [120]. Relay control systems are employed in a variety of technological domains due to their simplicity. Examples of industrial applications involving relay control were reported in [121]. One of the simplest and most famous examples is the thermostat. The device was able to measure the temperature in a room, compare this value with the desired one, and regulate the temperature in the room. Indeed, the thermostat was able to decide either to turn the heat on, if the temperature is too low; or to turn it off, if the temperature is too high. In a relay regulator, the control response (i.e. the output of the relay) changes every time the controlling signal (i.e. the input of the relay) exceeds fixed values, which are called threshold values ($\pm\epsilon$). Relay controller showed a switching behaviour. Often they work with unusually intensive and fast variations of control response. These variations could cause some undesired oscillations, as known as chattering phenomenon. To overcome the chattering behaviour, the characteristic curve needed a hysteresis. Hysteresis' idea was introduced in 1960s and only in 1980s receives more interest especially in connection with applications [122]. Hysteresis is defined as a rate-independent memory effect. Hysteresis depends on the current and the past states.

Due to the complexity of the dynamics of the mouse embryonic stem cells' biological system, we decided to apply a simple control strategy as Relay. Indeed, I employed the relay to decide the proper control action that had to be applied to the biological system to maintain the pluripotency spectrum desired. In this realization, the fluorescence intensity of the gene

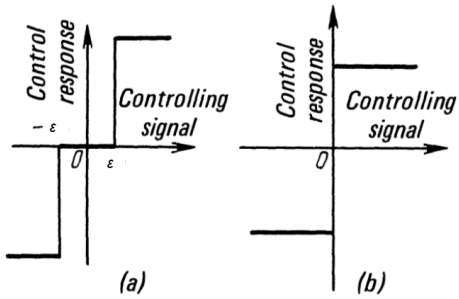

Figure 5.6. Relay controller. a) Relay controller's with hysteresis while b) without hysteresis.

of interest was chosen as the systems' output y(t) that had to be compared with the reference $r(t)$, in order to obtain the control error. Thus, the control error was computed as:

$$e(t) = r(t) - y(t) \tag{5.1}$$

In detail, the relay control of the biological system was designed to achieve pluripotency stem cells control. We investigate the 2i media condition. To this end, no drugs such as CH and PD are delivered when cells are in the naive state (i.e. above the desired reference); conversely, drugs are delivered when the cell moves into the direction of the spectrum of primed state (i.e. below the desired reference). The mathematical description of control law can be defined as follows:

$$u(t) = \begin{cases} u_{max} & \text{if} \quad e(t) \geq \epsilon \\ u_{min} & \text{if} \quad e(t) < \epsilon \end{cases} \tag{5.2}$$

where the hysteresis ϵ is equal to 5% of reference value. The maximum u_{max} and minimum u_{min} value could be considered as "ON/OFF" mechanism of our system. We performed two experiments applying model-free external feedback control of mESCs to automatically control the pluripotency spectrum. We selected two reference set-point $r = 50\%$ and $r = 80\%$, and are reported in figure 5.7. The experiments started with mESCs cultured for one week in 2i ensuring that the reporter is active. mESCs were controlled to reach and maintain 80% or 50% of the initial fluores-

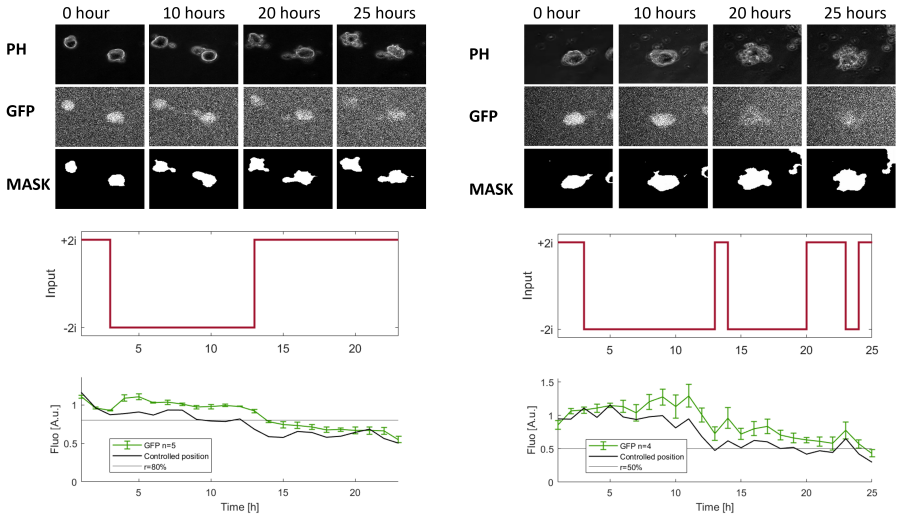

Figure 5.7. Automatic feedback control enables pluripotency tuning in mESCs with set-point 80% and 50%. Time-lapse images of mESCs grown in the microfluidic chamber for phase contrast (PH), green fluorescence protein (GFP), and segmentation mask generated using the Otsu method (MASK). Cells were imaged with a sampling time of 1 hour. The green line represents the averaged GFP fluorescence of the cells in the segmentation mask was calculated over time across the chambers (n=5 in a and n=4 in b) for the uncontrolled position, whereas the black line represents the controlled position. The red line represented the media received from the cells decided in real-time by the controller. In figure a) was reported pluripotency tuning in mESCs with set-point 80%, whereas in figure b) pluripotency tuning in mESCs with set-point 50%.

cence. The initial fluorescence was computed as the mean between the value of green fluorescence protein (GFP) during the initialization phase of 3 hours. Once the control experiment was initialized, as expected, PD and CH were initially removed until the desired reference fluorescence was achieved; pulses of PD and CH were then delivered to cells following a Relay strategy.
In detail, the red line represented the input delivered on the system decided by the controller, the black line represented the behavior of the controlled chamber position selected, and the green line represented the averaged GFP of the cells across the uncontrolled chambers. Images were acquired in PH and GFP. mESCs showed good response to drugs and the feedback strategy, although simple, was effective to automatically regulate Rex1 expression. Furthermore, the automatic control had a second benefit purpose for our aim which is to reduce the excessive and continuous exposure of the cells to drugs, CH and PD, while maintaining naïve stem cell states.

5.4 Characterization of stem cell pluripotency transitions via flow cytometry

We next decided to check if the dynamics in microfluidic were maintained when cells were cultured in dishes and fluorescence was measured by a flowcytometer. Flow cytometry is a technology that provides rapid multi-parametric analysis of single cells in solution. Flow cytometers utilize lasers as light sources to produce both scattered and fluorescent light signals that are read by detectors such as photodiodes or photomultiplier tubes. Cell populations can be analyzed and/or purified based on their fluorescent or light-scattering characteristics. Flow cytometry is a powerful tool that has a lot of applications in molecular biology [123].
First of all, we decided to test and validate 2i media behavior using a flow cytometry approach. The idea is to investigate the pluripotency spectrum transition from a naive to a primed state and in addition, explore if the process is reversible from primed to naive.
Naive-primed transition experiment was based on the concept to start with cells in a naive state, and then testing day by day via flow cytometry their behavior after the withdrawal of the drugs as reported in figure 5.8. We cultured cells in 2i media for 1 week and from a naive state, where CH

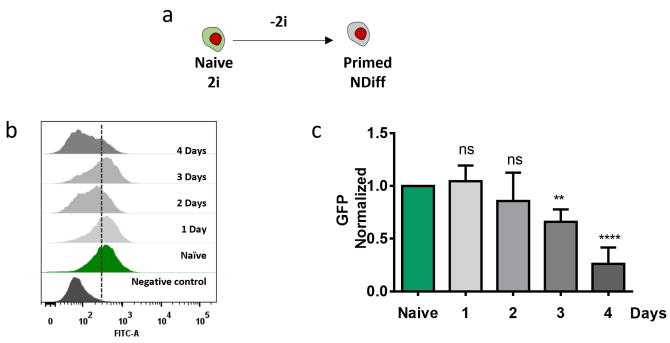

Figure 5.8. mESCs from naive to primed via flowcytometry for 2i culture. a) Experimental pipeline. b) Representative flow cytometry histogram of mESCs in the absence of the inhibitors CH 3µM and PD 1µM. c) Median Fluorescence Intensity (MFI) of mESCs cells cultured in the absence of inhibitors. p-values from two-tailed unpaired t-test computed over Naïve pluripotency are shown * $p < 0.05$, **$p<0.01$, ***$p<0.001$, ****$p<0.001$. Number of biological replicates n=2. Error measured as standard deviation.

and PD drugs were present, we removed them maintaining cells only in the basal media Ndiff227 for 4 days. We evaluated cells' behavior in the green spectrum as an indicator of pluripotency marker. We analyzed the representative histogram of mESCs during drugs perturbation, which reported how in a naive state the level of green fluorescence protein was higher and the distribution was unimodal and as soon the cells are pushed into a primed one with drug removal, it changed to a bimodal distribution. Furthermore, we quantified the Median Fluorescence Intensity (MFI) of mESCs cells cultured, and there is a relevant transition after 2 days of drugs withdrawal. On the basis of these results, that mESCs are pushed in primed state spectrum of pluripotency, we decided to investigate the case where the transition from primed to naive is reversible. We adapted cells from on week in 2i media reaching the naive state, then we removed the drugs for 3 days pushing cell into primed one, and from this condition we started to add again drugs testing day by day the GFP intensity. As reported in figure 5.9 the histogram of GFP intenisty transit from a unimodal (i.e naive state) to a multimodal (i.e primed state) and the again

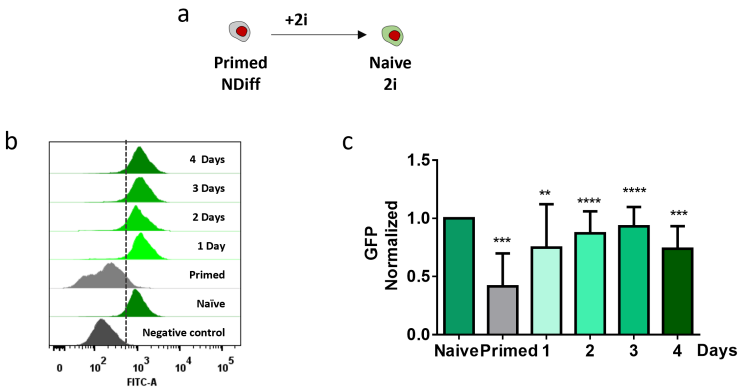

Figure 5.9. mESCs from naive to primed via flowcytometry for 2i culture. a) Experimental pipeline. b) Representative flow cytometry histogram of mESCs in the presence of the inhibitors CH 3µM and PD 1µM. c) Median Fluorescence Intensity (MFI) of mESCs cells cultured in the presence of inhibitors. p-values from two-tailed unpaired t-test computed over Naïve pluripotency are shown * $p < 0.05$, **$p<0.01$, ***$p<0.001$, ****$p<0.001$. Number of biological replicates n=2. Error measured as standard deviation.

to unimodal. The reversibility of primed state was also confirmed by the quantification of MFI.

Even though in 2i culture with simultaneous inhibition of Map-kinase and Gsk3 pathways, LIF is no longer required, recent findings also suggested that LIF has a role not covered by the 2i for the maintenance of naïve pluripotency. This suggested that LIF functions is suitable for the maintenance of naïve pluripotency in a context dependent manner [124]. LIF is critical for self-renewal and to maintain an undifferentiated state [108]. According to that knowledge and considering how previous results on cybergenetics characterization of 2i+LIF showed slow dynamics and delay in drug response when all the drugs CH, PD, and LIF are removed, we decided to investigate mouse embryonic stem cells behaviour for the 2i+LIF media via flow cytometry with a different approach. The design of experiment was based on culture mESCs in 2i+LIF for 1 week, then removing only CH and PD drugs for 4 days keeping always LIF present in the culture, and testing whenever cells showed a response with this different external pertubation.

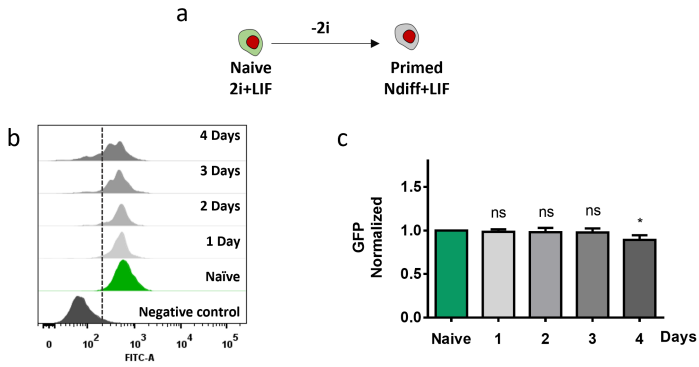

Figure 5.10. mESCs from naive to primed via flowcytometry for 2i+LIF culture. a) Experimental pipeline. b) Representative flow cytometry histogram of mESCs in the absence of the inhibitors CH 3µM and PD 1µM. c) Median Fluorescence Intensity (MFI) of mESCs cells cultured in the absence of inhibitors. p-values from two-tailed unpaired t-test computed over Naïve pluripotency are shown * $p < 0.05$, **$p<0.01$, ***$p<0.001$, ****$p<0.001$. Number of biological replicates n=2.Error measured as standard deviation.

In contrast to previous results where our aim was to allow the tuning of the pluripotency spectrum from naive to primed, in this case the experiment reported in 5.10 wanted to investigate if our selected mouse embryonic stem cells system with the constant presence of LIF could maintain the naive state removing CH and PD drugs for a short time. From the reported histogram for green fluorescence expression and from the evaluation of the median fluorescence intensity, mESCs could still maintain pluripotency upon these specific drugs perturbation for 2-3 days

5.5 Leveraging delayed drug response for new protocols' design

As our previous experiment reported in figure 5.10 showed that the response of cells to drugs is quite slow, we thought to leverage this delay to check if we could design a new protocol to culture mESCs while reducing exposure to drugs. An experimental pipeline is reported in figure 5.11. We cultured mouse embryonic stem cells in 2i+LIF media for 1 week and then

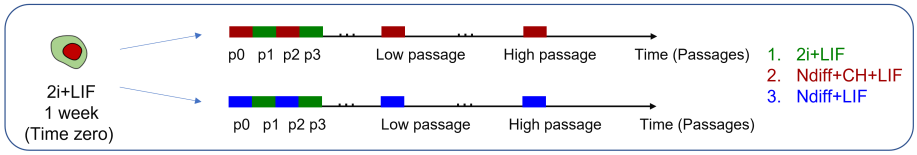

Figure 5.11. New protocol experimental pipeline.

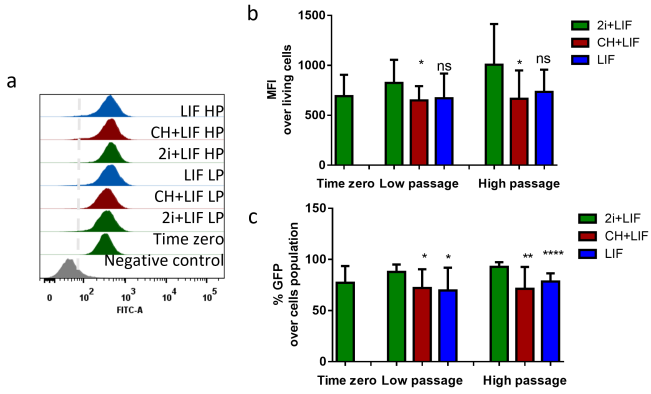

Figure 5.12. mESCs from naive to primed via flowcytometry for 2i+LIF culture. a) Experimental pipeline. b) Representative flow cytometry histogram of mESCs in the absence of the inhibitors CH 3µM and PD 1µM. c) Median Fluorescence Intensity (MFI) of mESCs cells cultured in the absence of inhibitors. p-values from two-tailed unpaired t-test computed over Naïve pluripotency are shown * $p < 0.05$, **$p<0.01$, ***$p<0.001$, ****$p<0.001$. Number of biological replicates n=2. Error measured as standard deviation.

alternate the drugs present in the media at each passage. We tested two different conditions, one where we delivered with the basal media Ndiff only the two drugs CH and LIF (Ndiff+CH+LIF) and one with basal media and LIF (Ndiff+LIF).
The main rationale is to reduce mESCs to inducing drugs ensuring pluripotency. Here, we cultured the mouse embryonic stem cells with this protocol for 2 months using this alternated approach and tested them via flow cytometry at the high and low passages (HP-LP), where low passage was one month of treatment and high passage was two months. We used the 2i+LIF condition as our positive control.
The data reported in figure 5.12 showed that the distribution is unimodal and remained constant among the culture condition over time. Then we evaluated the Median Fluorescence Intensity (MFI) and the percentage of Green Fluorescence Protein (%GFP) as indicator of how many cells were in the pluripotent state.
The data confirmed that GFP expression is comparable in the 2i+LIF, CH+LIF and LIF conditions.

RNA sequencing

Furthermore, to measure all the genes expressed by cells, not only Rex1 gene, we performed mRNA sequencing. We cultured the cells with the protocol as described in figure 5.11 and we collected samples for sequencing in the different culture conditions at a specific time point. The experiment involved the triplicate of mESCs samples in that culture condition at that time point as a reporter in table 5.1.

To gather inside the specific biological process, we also focused on gene

Table 5.1. Summary of media and time point in each experiment.

Experiment name	Media
EXP1	2i+LIF LP
EXP2	CH+LIF LP
EXP3	LIF LP
EXP4	2i+LIF HP
EXP5	CH+LIF HP
EXP6	LIF HP

expression. First of all, we investigated the distribution of the sample. In figure 5.13, the violin plot displayed the actual distribution of the log of the unnormalized gene counts for each sample in our experiment. We overlayed a box plot on a violin plot. Box plots are a standardized way to display the distribution of data based 5 metrics: minimum, first quartile, median, third quartile and maximum. Sometimes the mean is also displayed as a dot in the rectangle delimited by the 25th and 75th percentiles, but while box plots only graph summary statistics, violin plots showed the actual and full distribution of the data. In fact, they are rotated density plots on each side of the box plot, which gave us the ability to clearly observe the variation in the data. The legend in the figure reported the different samples, one by one, analyzed for media conditions and time points collection. In the plot, the distribution and median appeared similar among the conditions.

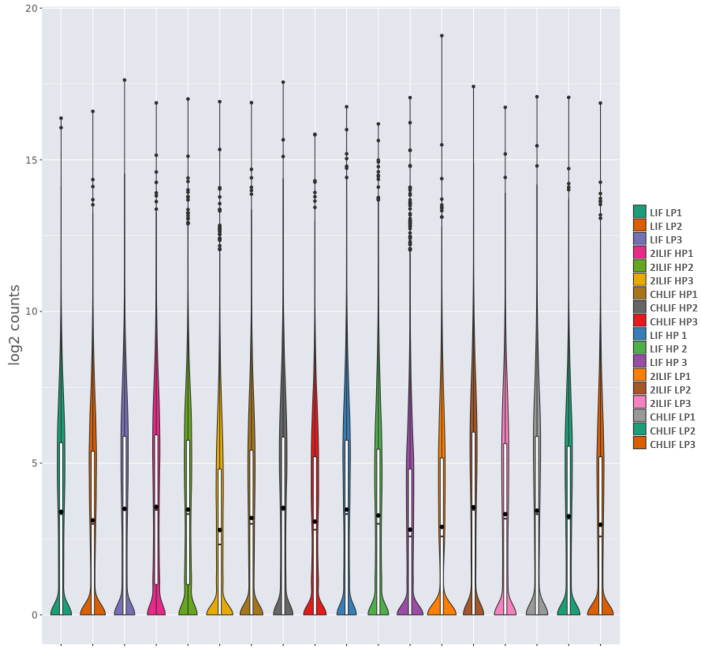

Figure 5.13. mESCs pluripotency: Violin plot. Representation of the distributions of numeric data for one or more groups.

Furthermore, another qualitative analysis was reported in figure 5.14.

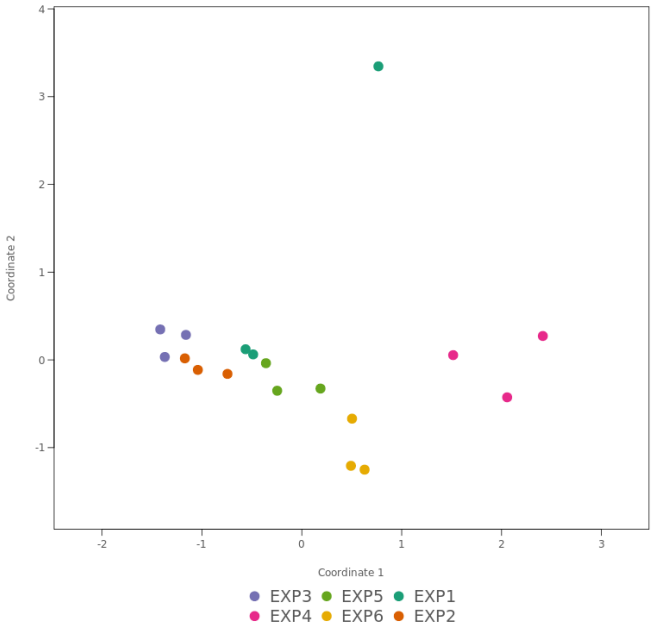

Figure 5.14. mESCs pluripotency: MSD plot. A multidimensional scaling between the different experiments. EXP1, represented in dark green, reports the behavior for 2i+LIF culture condition at low passage. EXP2, represented in orange, reports the behavior for CH+LIF culture condition at low passage. EXP3, represented in purple, reports the behavior for LIF culture condition at low passage. EXP4, represented in magenta, reports the behavior for 2i+LIF culture condition at high passage. EXP5, represented in light green, reports the behavior for CH+LIF culture condition at high passage. EXP6, represented in yellow, reports the behavior for LIF culture condition at high passage. Dots of a similar color represent biological replicates for each condition (n=3).

A multidimensional scaling (MDS) plot provided a visual representation of the patterns of proximities (i.e. similarities or distances) among the samples. In this case, we plotted the expression differences between samples within the experiment. Samples that are clustered together generally have similar patterns of expression. In the figure, each sample was represented as a dot. They were divided for culture condition and time point as reported in table 5.1. The representation cluster of our data showed a similar expression pattern. The 2i+LIF, CH+LIF and LIF media at low passage cluster together, whereas the 2i+LIF, CH+LIF and LIF at high passage represented a less similar behavior. Furthermore, other data and types of analysis could gave us other information and interpretations. We then analyzed genes that were differential expressed between conditions. The number of genes differential expressed and the relative pathways were reported in table 5.2. Furthermore, a vulcano plot was generated for each comparison, among culture conditions and time points. Indeed, vulcano plots were reported in the figures 5.15, 5.16, 5.17 and showed differences in expression between the groups of the selected comparison. The log ratio of the fold change is on the X axis, the negative log of p-adj/p-value is on the Y axis, and each dot represents a gene within the comparison performed.

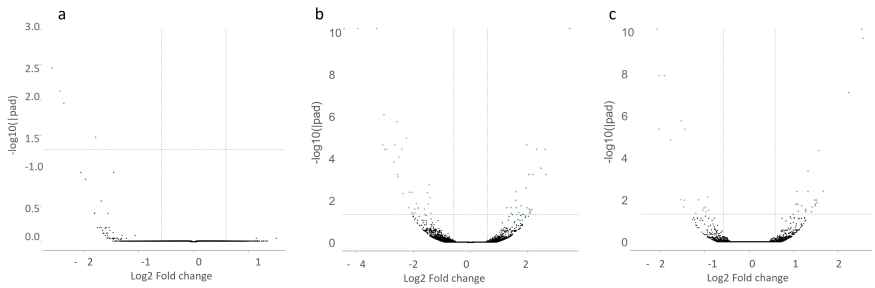

Figure 5.15. Comparison between experimental conditions for differential expression at the low passage: Vulcano plot. a) Represents the comparison between CH+LIF media vs 2i+LIF. b) Represents the comparison between LIF media vs 2i+LIF c)Represents the comparison between LIF media vs CH+LIF.

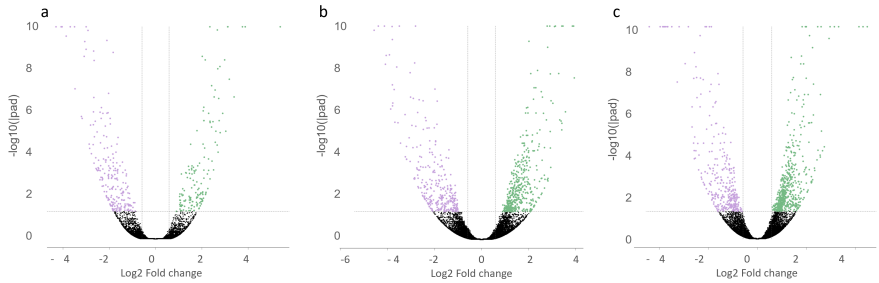

Figure 5.16. Comparison between experimental conditions for differential expression at the high passage: Vulcano plot. a) Represents the comparison between CH+LIF media vs 2i+LIF. b) Represents the comparison between LIF media vs 2i+LIF c)Represents the comparison between LIF media vs CH+LIF.

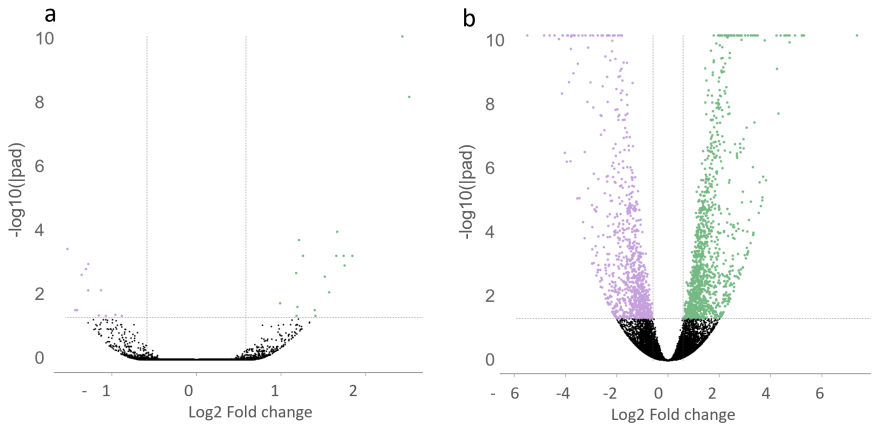

Figure 5.17. Comparison between experimental conditions for differential expression at the high and the low passage for CH+LIF vs LIF media: Vulcano plot.

The fold change was selected between values ≤ 1.5 and ≥ 1.5 and p-Adj fixed to a selected threshold of 0.05000. Furthermore, the coloring on the dots reflected the clustering information for each gene, and those in black are genes that do not pass the parameters of the filter selected. Genes with the same coloring are grouped together based on the similarity of their expression pattern. In figure 5.15 was reported the comparison between culture conditions at low passage, in figure 5.16 comparison between culture conditions at high passage, and in figure 5.17 comparison between low passage and high passage for CH+LIF and LIF media respectively. These results suggested that the number of genes differentially expressed is overall quite low. All the samples at low passages were quite similar in terms of gene expression while at high passages the LIF only culturing condition appeared to be more different from both the CH+LIF and 2i+LIF high passages samples, and the LIF low passage sample.

Table 5.2. Comparison between experimental conditions for differential expression.

Experiments	Media	Genes Number	Pathways
EXP2 vs EXP1	CH+LIF LP vs 2i+LIF LP	5	Table A.1
EXP3 vs EXP1	LIF LP vs 2i+LIF LP	60	Table A.2
EXP3 vs EXP2	LIF LP vs CH+LIF LP	40	Table A.3
EXP5 vs EXP4	CH+LIF HP vs 2i+LIF HP	386	TableA.4
EXP6 vs EXP4	LIF HP vs 2i+LIF HP	765	Table A.5
EXP6 vs EXP5	LIF HP vs CH+LIF HP	909	Table A.6
EXP5 vs EXP2	CH+LIF HP vs CH+LIF LP	29	Table A.7
EXP6 vs EXP3	LIF HP vs LIF LP	2120	Table A.8

Even though all those results were promising, we also focused on the investigation of gene expression for a set of genes involved in mESCs characterization. In figure 5.18 was reported the gene expression for a list of genes involved in the general pluripotency expression behavior. Our results showed that for all of them, but for Utf1, Zic3, and Sox2, changes were not significant across conditions suggesting that by alternating exposure to drugs, we had not impaired the pluripotency. Furthermore, we investigated specific genes involved in the naive state as reported in figure 5.19, and similarly to the pluripotency, we were not impairing pluripotency potential. Next, we checked the expression of groups of genes that are involved in the differentiation process, in particular, we focused on mesoderm, en-

doderm and ectoderm specification as reported in figures 5.20, 5.21, 5.22. Although those genes as expected are expressed at a low level, for the majority we did not find any significant difference across culture conditions; further suggesting that alternating drugs was not impairing the pluripotency potential of cells. Here, we demonstrated how constant exposure to the drugs is not strictly necessary for maintaining pluripotency in mESCs. The advantages of not exposing constantly mESCs to drugs are relevant not only for biological applications, because can overcome problems due to long-term culture, but also relevant to cost saving due to lower amount of drugs required for mESCs long-term culture.

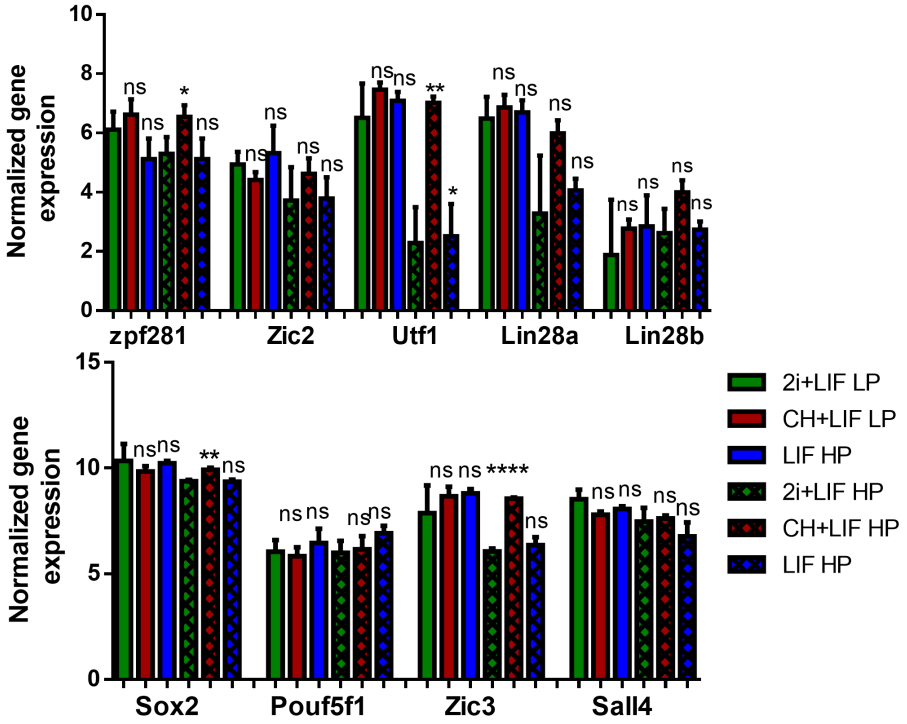

Figure 5.18. Gene expression for general pluripotency. Gene expression is normazalized via Relative Log Expression (RLE) using DESeq2 R library [112]. p-values from two-tailed unpaired t-test computed over Naïve pluripotency are shown * $p < 0.05$, **$p<0.01$, ***$p<0.001$, ****$p<0.001$.

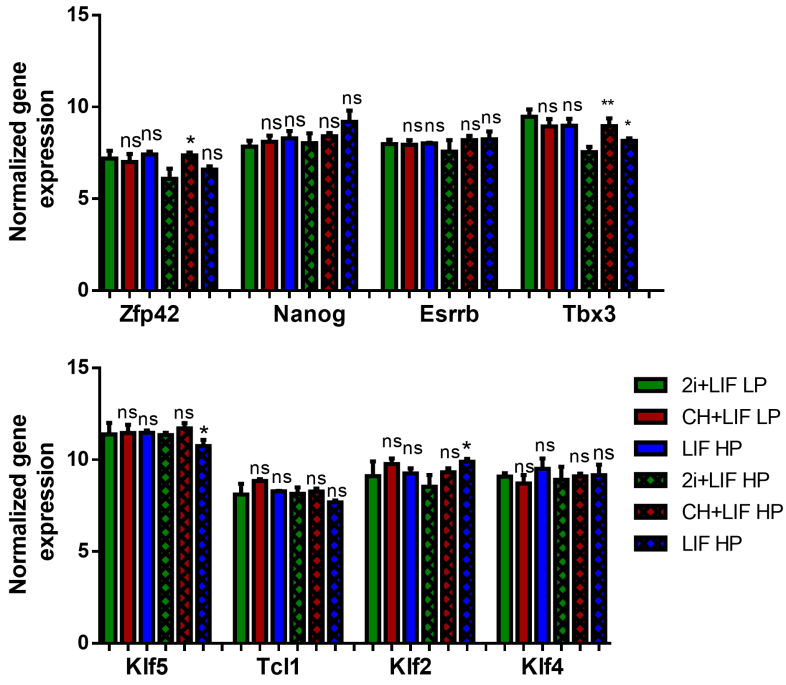

Figure 5.19. Gene expression for naive pluripotency. Gene expression is normalized via Relative Log Expression (RLE) using DESeq2 R library [112]. p-values from two-tailed unpaired t-test computed over Naïve pluripotency are shown * $p < 0.05$, **$p<0.01$, ***$p<0.001$, ****$p<0.001$.

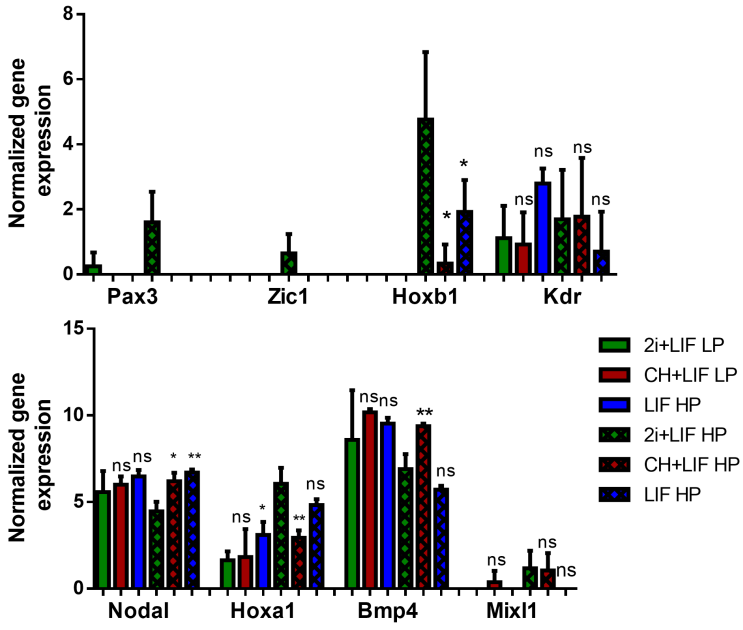

Figure 5.20. Gene expression for mesoderm genes. Gene expression is normalized via Relative Log Expression (RLE) using DESeq2 R library [112]. p-values from two-tailed unpaired t-test computed over Naïve pluripotency are shown * $p < 0.05$, **$p<0.01$, ***$p<0.001$, ****$p<0.001$.

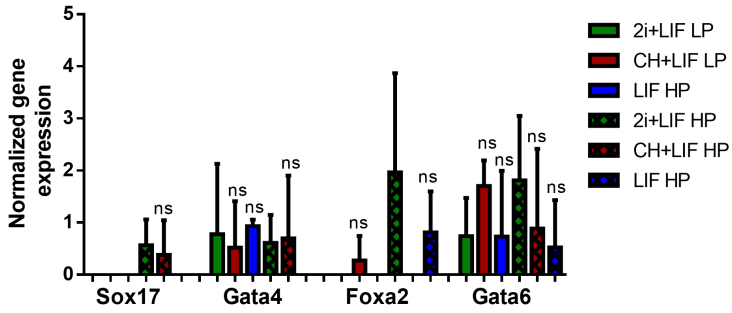

Figure 5.21. Gene expression for endoderm genes. Gene expression is normalized via Relative Log Expression (RLE) using DESeq2 R library [112]. p-values from two-tailed unpaired t-test computed over Naïve pluripotency are shown * $p < 0.05$, **p<0.01, ***p<0.001, ****p<0.001.

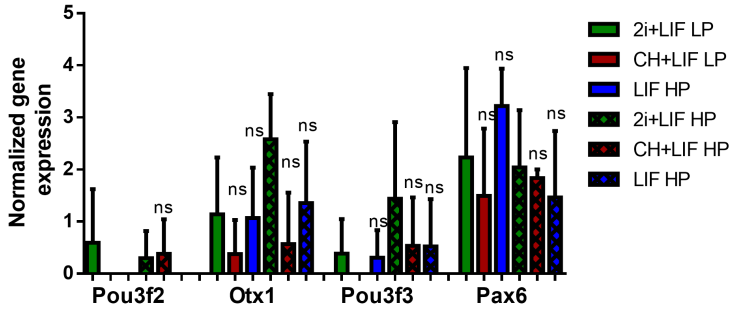

Figure 5.22. Gene expression for ectoderm genes. Gene expression is normalized via Relative Log Expression (RLE) using DESeq2 R library [112]. p-values from two-tailed unpaired t-test computed over Naïve pluripotency are shown * $p < 0.05$, **p<0.01, ***p<0.001, ****p<0.001.

5.6 Discussion

In this chapter, we investigated the feasibility to characterize mESCs dynamics via cybergenetic tools such as specific experimental microfluidic/microscopy platform, and via flow cytometry. We showed how the naive-primed transition and from primed to naive transition could be monitored and investigated with different approaches and techniques. In addition, we developed and implemented an external model-free feedback control to automatically regulate mouse embryonic stem cells pluripotency spectrum transition. We performed specific experiments with two different set points 50 % and 80 % allowing us to alternate the delivery of drugs such as CH and PD with a basal media. In this work, our main aim was to characterize and define a new protocol that allows long-term mESCs culture to maintain stem cells identity. Here, after mESCs system dynamic characterization, we proposed a new approach to culture mESCs. Taking advantage of the capability of LIF to maintain pluripotency on its own we alternated at each passage the presence or absence of drugs. Indeed, we showed two possible alternative methods to culture mESCs. From standard culture conditions the serum-free media 2i+lif was characterized by a constant presence of drugs such as PD, CH and LIF, whereas with our protocol we alternate their presence and this is not affecting pluripotency as confirmed from our flow cytometry and sequencing results. Furthermore, we are planning to perform further experiments to better characterize our culture protocol, in particular, we will perform AP staining and measure the differentiation potential of cells cultured in the described media.
In conclusion, regarding cybergenetics applications, we cannot perform experiments for a long time (weeks) and for this reason, a possible scale-up of the experimental platform, such as culture in a microfluidic bioreactor could be implemented for further applications [125],[126]. The development of our culture protocol in a bioreactor will allow the maintenance, monitoring and control pluripotency spectrum, and the fields of application could be disruptive. The possibility to generate a high quantity of stem cells culture in a bioreactor could facilitate the possibility of further and future applications as a translation for organ-on-chip or applications for bio-printing tissue applications [127],[128].

Chapter 6

Conclusions

The increasing development of new technologies in synthetic biology, microfluidic, and control theory fields rise the number of possible applications on cybergenetics.
In this work, I presented in chapter 2 the state of the art of two biological problems: cell cycle synchronization and mESCs culture protocol optimization. During my studies, I tried and aimed to address these two problems using modern tools of cybergenetics and microfluidic/microscopy platform. The platform that I used has been previously set up for different types of cells but the key novelties of my work were the applications to different biological systems as well as the development of new technological tools.
In detail, in chapter 3 I introduced and defined how to achieve yeast cell cycle synchronization in budding yeast.
We explored the possibility to synchronize a population of budding yeast by forcing cells to divide in a coordinated fashion for multiple generations. Yeast cell cycle synchronization was required mostly for industrial applications. Scientists needed a synchronized population of cells to enable robust measurements of morphological, phenotypical, and molecular properties. Even though there were well-defined protocols to acheve syncronization, scientists still struggle to maintain and achieve long-term yeast cell cycle synchronization. For those reasons, we introduced a new approach based on microfluidic/microscopy application and control theory to tackle the problem of long-term synchronization. Specifically, we developed a com-

pletely automated approach based on a microfluidics platform implementing a feedback control strategy able to maintain an exponentially growing yeast population synchronised over time. Our approach opened the way to automatic control of yeast cell cycle, offering a tool to study the cell cycle and for biotechnological applications. One of the main limitations of our approach was the impossibility to control of a large number of cells as the one required for industrial application with our device, however, our system could be easily scaled up. As matter of fact, it is possible to swap from microfluidics to cheats by switching to optogenetics-based gene expression control systems, opening the way for industrial applications. In addition, our approach could also be used to facilitate open-loop control strategies as it could automatically identify the best period and duration of stimulation to apply to yeast strains of scientific and commercial interest in different growth media and environmental conditions.
In chapter 4, we reported new tools for cybergenetic applications. The big expansion of cybergenetics field led to the need to define and develop new tools for precise image segmentation and long-term microfluidic culture. Even though, a range of segmentation algorithms has been proposed to automatically analyze images of organisms they were often difficult to adjust for specific needs and could not be extended to new types of analysis. For those reasons, we developed Cheetah, an easy-to-use computational toolkit that was highly adaptable to new needs in cybergenetic applications. Its major contribution was in providing a coherent computational framework that combines both robust U-Net image segmentation with analysis functions tailored for the rapid development of cybergenetic control setups and was suitable to apply to a complex morphological system such as mouse embryonic stem cells that changed their morphology over time. Furthermore, the code provided in the toolkit could easily be refined, customized, and extended to allow for new features to be implemented as more sophisticated control strategies. One of the main possible limitations of deep learning approaches was the necessity to retrain the system when changes were made to the types of input data, such as the changes due to the use of a different cell type. One of the possibilities to overcome such limitations was the development of new tools for transfer learning. However, we expected the deep learning methods that are central to Cheetah's capabilities will play an increasingly important role in synthetic biology applications.

In addition, in the last years, the fields of designing microfluidic devices for a range of mammalian cell applications received great interest. A lot of designs have been developed for applications such as parallelized drug screening, easy-to-use perfusion for cell proliferation and differentiation studies, and automated feedback control of gene expression. However, the possibility to culture long-term mammal cells is still an open challenge due to the high sensibility of this organism. Indeed, we investigated this field and we developed a microfluidic device for long-term culture for mouse embryonic stem cells. The device allowed cell culture with reduced shear stress and dynamical cell stimulation with combinations of 4 different media, which could be automatically delivered to cells via computer-controlled pumps. Specifically, one of the main applications of the device could be to allow automatic control of cells' behavior in real time. Furthermore, for the first time a single-layer microfluidic platform has been proposed to allow mixing of different media inside the device and for long term mammal culture. The outcoming of our device can be disruptive for closed-loop experiments when the long-term culture was required.
In chapter 5 we investigated, characterized, and studied pluripotency transition in mESCs. Even though was well-known how to maintain mESCs pluripotent state in vitro, there were still limitations due to high variability across cell cultures and over long term culture. Here, we investigated and design a new optimized protocol to maintain pluripotency in mESCs for long culture. Specifically, we explored the pluripotency transition from naive to primed and primed to naive via a microfluidic/experimental platform and via a flow cytometry approach. In both cases, we monitored the response to the external perturbations applied to mESCs. Furthermore, we applied a model-free external feedback control to automatically regulate the pluripotency transition. We managed to decide the best input for the cells in real-time and we manage to steer the dynamics of mESCs to reach and maintain a specific value of the expression of the pluripotency gene in a completely automatic way. Finally, a new culturing protocol to control mESCs identity was developed in this work. Starting from previous data obtained via microscopy /microfluidic and flow cytometer sensors, we concluded that the constant presence of all the drugs is not strictly necessary to keep pluripotency and those led us to define a new protocol in the dish to optimize mESCs culture. We cultured cells in 2i+LIF

media for 1 week and then we started to alternate the drugs present in the media at each passage. We tested two different conditions: one where we delivered two drugs (Ndiff+CH+LIF) and one with one (Ndiff+LIF). We cultured the cells for a couple of months using this alternate approach and tested them via flow cytometry and via RNA sequencing, and the results showed that pluripotency is not altered with the new protocol. We believed that avoiding the constant presence of drugs in the media could allow long-term culture in serum-free media for mESCs while still maintaining pluripotency. Even though our results were promising and could improve the way to culture mESCs, they still required additional tests to further validate our preliminary results.

Appendix A

Appendix

Table A.1. Pathways involved in the comparison between the media condition of CH+LIF vs 2i+LIF at low passage culture.

Pathways	p-Adj
WikiPathways	
SIDS Susceptibility Pathways	0.01321
BioPlanet	
Highly sodium permeable acetylcholine nicotinic receptors	0.00936
Acetylcholine binding and downstream events	0.00936
Nicotine activity on dopaminergic neurons	0.00936
SIDS susceptibility pathways	0.01733
Nuclear beta-catenin signaling and target gene transcription regulation	0.01733
PANTHER	
Nicotine pharmacodynamics pathway	0.02830
Nicotinic acetylcholine receptor signaling pathway	0.03436
REACTOME	
Highly sodium permeable postsynaptic acetylcholine nicotinic receptors	0.00257
Highly calcium permeable nicotinic acetylcholine receptors	0.00257
Highly calcium permeable postsynaptic nicotinic acetylcholine receptors	0.00257
TRP channels	0.00631
Pathway Interaction DB	
Regulation of Wnt-mediated beta catenin signaling and target gene transcription	0.03513

Table A.2. Pathways involved in the comparison between the media condition of LIF vs 2i+LIF at low passage culture.

Pathways	p-Adj
WikiPathways	
Arachidonate Epoxygenase Epoxide Hydrolases	0.20609
One carbon metabolism and related pathways	0.20609
mir-193a and MVP in colon cancer metastasis	0.20609
Myometrial Relaxation and Contraction Pathways	0.20609
Wnt Signaling Pathway	0.20609
BioPlanet	
Amino acid metabolism	0.18840
PI3K class IB pathway in neutrophils	0.18840
GFR1b ligand binding and activations	0.18840
Ion channel and phorbal esters signaling pathway	0.18840
Phospholipase C delta-1 interactions in phospholipid-associated cell signaling	0.18840
PANTHER	
Asparagine and aspartate biosynthesis	0.26295
TGF-beta signaling pathway	0.26295
Cell cycle	0.26295
Enkephalin release	0.26295
Opioid prodynorphin pathway	0.26295
REACTOME	
Biosynthesis of maresins	0.06261
Response to elevated platelet cytosolic Ca2+	0.06261
Synthesis of epoxy (EET) and dihydroxyeicosatrienoic acids (DHET)	0.06261
Antagonism of Activin by Follistatin	0.06261
FGFR1b ligand binding and activation	0.06261
BIOCYC	
L-cysteine degradation VI	0.03072
asparagine biosynthesis I	0.03072
L-cysteine degradation I I	0.03072
creatine biosynthesis I	0.03072
leucine degradation I I I	0.03072
Pathway Interaction DB	
Regulation of Wnt-mediated beta catenin signaling and target gene transcription	0.12910
Validated targets of C-MYC transcriptional activation	0.12910
Ras signaling in the CD4+ TCR pathway	0.12910
JNK signaling in the CD4+ TCR pathway	0.12910
IL2 signaling events mediated by STAT5	0.17501

Table A.3. Pathways involved in the comparison between the media condition of LIF vs CH+LIF at low passage culture.

Pathways	p-Adj
WikiPathways	
Arachidonate Epoxygenase Epoxide Hydrolase	0.16526
Wnt Signaling Pathway	0.16526
Lung fibrosis	0.16526
mir-193a and MVP in colon cancer metastasis	0.16526
Amino Acid metabolism	0.18310
BioPlanet	
Interleukin-2 signaling pathway	0.12540
Lysosome	0.12540
Bioactive peptide-induced signaling pathway	0.12540
PI3K class IB pathway in neutrophils	0.12540
Kit receptor signaling pathway	0.12540
PANTHER	
Thyrotropin-releasing hormone receptor signaling pathway	0.12091
Asparagine and aspartate biosynthesis	0.12091
FGF signaling pathway	0.12091
Cell cycle	0.12091
Enkephalin release	0.12091
REACTOME	
Biosynthesis of maresins	0.03931
Metallothioneins bind metals	0.03931
Response to elevated platelet cytosolic Ca2+	0.03931
CREB3 factors activate genes	0.03931
Synthesis of epoxy (EET) and dihydroxyeicosatrienoic acids (DHET)	0.03931
BIOCYC	
asparagine biosynthesis I	0.02312
threonine degradation III (to methylglyoxal)	0.02312
leucine degradation I	0.02312
valine degradation I	0.02312
Leucine Catabolism	0.03455
Pathway Interaction DB	
Validated targets of C-MYC transcriptional activation	0.12975
Ras signaling in the CD4+ TCR pathway	0.12975
JNK signaling in the CD4+ TCR pathway	0.12975
Reelin signaling pathway	0.13673
IL2 signaling events mediated by STAT5	0.13673

Table A.4. Pathways involved in the comparison between the media condition of CH+LIF vs 2i+LIF at high passage culture.

Pathways	p-Adj
WikiPathways	
PluriNetWork	3.4e-07
Neural Crest Differentiation	0.00052
miR-127 in mesendoderm differentiation	0.04304
Dopaminergic Neurogenesis	0.20629
Eicosanoid Synthesis	0.18310
BioPlanet	
Wnt interactions in lipid metabolism and immune response	0.00200
TGF-beta regulation of extracellular matrix	0.00430
NODAL signaling regulation	0.00966
Basigin interactions	0.02842
PANTHER	
Vasopressin synthesis	0.49955
TGF-beta signaling pathway	0.49955
Glycolysis	0.49955
Alzheimer disease-presenilin pathway	0.49955
Wnt signaling pathway	0.49955
REACTOME	
Basigin interactions	0.01308
Repression of WNT target genes	0.08764
MET interacts with TNS proteins	0.12300
Amino acid transport across the plasma membrane	0.12300
N-Glycan antennae elongation	0.12300
BIOCYC	
urate degradation to allantoin	0.05407
ureide biosynthesis	0.05485
UDP-alpha-D-glucuronate biosynthesis (from UDP-glucose)	0.25667
Fe(III)-reduction and Fe(II) transport	0.25667
Pathway Interaction DB	
Regulation of Wnt-mediated beta catenin signaling and target gene transcription	0.14598
EphrinB-EPHB pathway	0.50137
Glypican 3 network	0.50137
Signaling events mediated by PRL	0.50137
Validated targets of C-MYC transcriptional repression	0.50137

Table A.5. Pathways involved in the comparison between the media condition of LIF vs 2i+LIF at high passage culture.

Pathways	p-Adj
WikiPathways	
Electron Transport Chain	4.8e-10
Cytoplasmic Ribosomal Proteinsy	4.8e-10
Oxidative phosphorylatio	6.6e-08
Folic Acid Network	0.00506
Selenium Micronutrient Network	0.14485
BioPlanet	
Alzheimer's disease	0.12540
Translation	0.12540
Electron transport chain	0.12540
Oxidative phosphorylation	0.12540
Activation of mRNA upon binding of the cap-binding complex and eIFs, and subsequent binding to 43S	0.12540
PANTHER	
De novo pyrimidine deoxyribonucleotide biosynthesis	0.15348
Salvage pyrimidine ribonucleotides	0.15348
p53 pathway	0.19162
De novo purine biosynthesis	0.19162
Coenzyme A biosynthesis	0.21945
REACTOME	
Nonsense Mediated Decay (NMD) independent of the Exon Junction Complex (EJC)	0
Nonsense Mediated Decay (NMD) enhanced by the Exon Junction Complex (EJC)	0
Formation of the ternary complex, and subsequently, the 43S complex	0
GTP hydrolysis and joining of the 60S ribosomal subunit	0
SRP-dependent cotranslational protein targeting to membrane	0
BIOCYC	
aerobic respiration – electron donor II	2.1e-09
NADH to cytochrome bo oxidase electron transfer I	5.8e-07
glutathione redox reactions I	0.01667
Leloir pathway	0.32410
Pathway Interaction DB	
Direct p53 effectors	0.01616
Regulation of Wnt-mediated beta catenin signaling and target gene transcription	0.26201
Validated targets of C-MYC transcriptional repression	0.68302
p53 pathway	0.68302
Aurora A signaling	0.68302

Table A.6. Pathways involved in the comparison between the media condition of LIF vs CH+LIF at high passage culture.

Pathways	p-Adj
WikiPathways	
Cytoplasmic Ribosomal Proteins	5.7e-10
Electron Transport Chain	5.7e-10
Oxidative Stress	0.30145
BioPlanet	
Respiratory electron transport, ATP biosynthesis by chemiosmotic coupling, and heat production by uncoupling proteins	1.6e-09
Activation of mRNA upon binding of the cap-binding complex and eIFs, and subsequent binding to 43S	1.6e-09
Influenza viral RNA transcription and replication	1.6e-09
Oxidative phosphorylation	0.12540
Activation of mRNA upon binding of the cap-binding complex and eIFs, and subsequent binding to 43S	0.12540
PANTHER	
p53 pathway	0.58600
P53 pathway feedback loops 1	0.58600
Parkinson disease	0.58600
Integrin signalling pathway	0.58600
Salvage pyrimidine ribonucleotides	0.58600
REACTOME	
GTP hydrolysis and joining of the 60S ribosomal subunit	0
Formation of the ternary complex, and subsequently, the 43S complex	9.5e-10
Nonsense Mediated Decay (NMD) enhanced by the Exon Junction Complex (EJC)	9.5e-10
Nonsense Mediated Decay (NMD) independent of the Exon Junction Complex (EJC)	1.1e-09
SRP-dependent cotranslational protein targeting to membrane	1.1e-09
BIOCYC	
aerobic respiration – electron donor II	2.2e-06
NADH to cytochrome bo oxidase electron transfer I	5.8e-07
NADH to cytochrome bd oxidase electron transfer I	1.9e-05
glycine cleavage complex	0.30419
glutathione redox reactions I	0.30419
Pathway Interaction DB	
Sumoylation by RanBP2 regulates transcriptional repression	0.16462
Aurora A signaling	0.16462
ErbB1 downstream signaling	0.29930
Validated targets of C-MYC transcriptional repression	0.37590
p53 pathway	0.42014

Table A.7. Pathways involved in the comparison between the media condition of CH+LIF at low and high passage.

Pathways	p-Adj
WikiPathways	
Selenium Micronutrient Network	0.17505
White fat cell differentiation	0.17505
PluriNetWork	0.17505
SIDS Susceptibility Pathways	0.17505
Lung fibrosis	0.17505
BioPlanet	
Nuclear beta-catenin signaling and target gene transcription regulation	0.04003
Highly sodium permeable acetylcholine nicotinic receptors	0.15946
SREBP control of lipid biosynthesis	0.15946
Nitric oxide effects	0.15946
NODAL signaling regulation	0.15946
PANTHER	
Nicotine pharmacodynamics pathway	0.26061
Cytoskeletal regulation by Rho GTPase	0.26061
p53 pathway	0.26061
Nicotinic acetylcholine receptor signaling pathway	0.26061
Parkinson disease	0.26061
REACTOME	
Recruitment of NuMA to mitotic centrosomes	0.05768
RUNX3 regulates WNT signaling	0.05768
Transcriptional Regulation by VENTX	0.05768
Highly sodium permeable postsynaptic acetylcholine nicotinic receptors	0.05768
Highly calcium permeable nicotinic acetylcholine receptors	0.05768
BIOCYC	
aerobic respiration – electron donor II	2.2e-06
Pathway Interaction DB	
Regulation of Wnt-mediated beta catenin signaling and target gene transcription	0.01159
p38 signaling mediated by MAPKAP kinases	0.10722
Insulin-mediated glucose transport	0.10722
a6b1 and a6b4 Integrin signaling	0.10722
Trk receptor signaling mediated by PI3K and PLC-gamma	0.10722

Table A.8. Pathways involved in the comparison between the media condition of LIF at high and low passage.

Pathways	p-Adj
WikiPathways	
Oxidative phosphorylation	5.4e-10
Cytoplasmic Ribosomal Proteins	5.4e-10
Electron Transport Chain	5.4e-10
PluriNetWork	3.1e-093.1e-09
mRNA processing	8.5e-05
BioPlanet	
Alzheimer's disease	0
Translation	0
Electron transport chain	0
Oxidative phosphorylation	0
Disease	0
PANTHER	
p53 pathway	0.05101
p53 pathway feedback loops 2	0.05101
Parkinson disease	0.17655
De novo pyrimidine deoxyribonucleotide biosynthesis	0.45500
Pyruvate metabolism	0.45500
REACTOME	
Major pathway of rRNA processing in the nucleolus and cytosol	0
Nonsense Mediated Decay (NMD) independent of the Exon Junction Complex (EJC)	0
Nonsense Mediated Decay (NMD) enhanced by the Exon Junction Complex (EJC)	0
Ribosomal scanning and start codon recognition	0
Complex I biogenesis	0
BIOCYC	
aerobic respiration – electron donor II	0
NADH to cytochrome bo oxidase electron transfer I	0
NADH to cytochrome bd oxidase electron transfer I	0
Targeted protein degradation	0.02422
L-cysteine degradation VI	0.49816
Pathway Interaction DB	
FoxO family signaling	0.07946
Aurora B signaling	0.07946
ErbB1 downstream signaling	0.07946
Validated targets of C-MYC transcriptional activation	0.07946
Aurora A signaling	0.07946

Bibliography

[1] Domitilla Del Vecchio, Yili Qian, Richard M Murray, and Eduardo D Sontag. Future systems and control research in synthetic biology. *Annual Reviews in Control*, 45:5–17, 2018.

[2] Domitilla Del Vecchio, Aaron J Dy, and Yili Qian. Control theory meets synthetic biology. *Journal of The Royal Society Interface*, 13(120):20160380, 2016.

[3] Z Tuza, L Bandiera, D Gomez-Cabeza, GB Stan, and F Menolascina. A systematic framework for biomolecular system identification. In *Proceedings of the 58th IEEE Conference on Decision and Control*, 2019.

[4] M. Khammash, M. Di Bernardo, and D. Di Bernardo. Cybergenetics: Theory and methods for genetic control system. In *2019 IEEE 58th Conference on Decision and Control (CDC)*, pages 916–926, 2019.

[5] Iacopo Ruolo, Sara Napolitano, Davide Salzano, Mario di Bernardo, and Diego di Bernardo. Control engineering meets synthetic biology: Foundations and applications. *Current Opinion in Systems Biology*, 28:100397, 2021.

[6] Filippo Menolascina, Mario Di Bernardo, and Diego Di Bernardo. Analysis, design and implementation of a novel scheme for in-vivo control of synthetic gene regulatory networks. *Automatica*, 47(6):1265–1270, 2011.

[7] Gianfranco Fiore, Filippo Menolascina, Mario Di Bernardo, and Diego Di Bernardo. An experimental approach to identify dynamical models of transcriptional regulation in living cells. *Chaos: An Interdisciplinary Journal of Nonlinear Science*, 23(2):025106, 2013.

[8] Filippo Menolascina, Gianfranco Fiore, Emanuele Orabona, Luca De Stefano, Mike Ferry, Jeff Hasty, Mario Di Bernardo, and Diego Di Bernardo.

In-vivo real-time control of protein expression from endogenous and synthetic gene networks. *PLoS computational biology*, 10(5):e1003625, 2014.

[9] Gianfranco Fiore, Giansimone Perrino, Mario Di Bernardo, and Diego Di Bernardo. In vivo real-time control of gene expression: a comparative analysis of feedback control strategies in yeast. *ACS synthetic biology*, 5(2):154–162, 2016.

[10] Chiara Fracassi, Lorena Postiglione, Gianfranco Fiore, and Diego Di Bernardo. Automatic control of gene expression in mammalian cells. *ACS synthetic biology*, 5(4):296–302, 2016.

[11] Lorena Postiglione, Sara Napolitano, Elisa Pedone, Daniel L Rocca, Francesco Aulicino, Marco Santorelli, Barbara Tumaini, Lucia Marucci, and Diego di Bernardo. Regulation of gene expression and signaling pathway activity in mammalian cells by automated microfluidics feedback control. *ACS synthetic biology*, 7(11):2558–2565, 2018.

[12] Elisa Pedone, Lorena Postiglione, Francesco Aulicino, Dan L Rocca, Sandra Montes-Olivas, Mahmoud Khazim, Diego di Bernardo, Maria Pia Cosma, and Lucia Marucci. A tunable dual-input system for on-demand dynamic gene expression regulation. *Nature communications*, 10(1):1–13, 2019.

[13] Barbara Shannon, Criseida G Zamora-Chimal, Lorena Postiglione, Davide Salzano, Claire S Grierson, Lucia Marucci, Nigel J Savery, and Mario Di Bernardo. In vivo feedback control of an antithetic molecular-titration motif in escherichia coli using microfluidics. *ACS Synthetic Biology*, 9(10):2617–2624, 2020.

[14] Giansimone Perrino, Sara Napolitano, Francesca Galdi, Antonella La Regina, Davide Fiore, Teresa Giuliano, Mario di Bernardo, and Diego di Bernardo. Automatic synchronisation of the cell cycle in budding yeast through closed-loop feedback control. *Nature communications*, 12(1):1–12, 2021.

[15] Elisa Pedone, Irene De Cesare, Criseida G Zamora-Chimal, David Haener, Lorena Postiglione, Antonella La Regina, Barbara Shannon, Nigel J Savery, Claire S Grierson, Mario Di Bernardo, et al. Cheetah: a computational toolkit for cybergenetic control. *ACS Synthetic Biology*, 10(5):979–989, 2021.

[16] Adil Mustafa, Elisa Pedone, Antonella La Regina, Ahmet Erten, and Lucia Marucci. Development of a single layer microfluidic device for dynamic stimulation, culture and imaging of mammalian cells. *bioRxiv*, 2022.

[17] Antonella La Regina, Elisa Pedone, and Lucia Marucci. Culturing pluripotent stem cells: state of the art, challenges and future opportunities. *Current Opinion in Systems Biology*, 28:100364, 2021.

[18] Sierra Brooks and Hal Alper. Applications, challenges, and needs for employing synthetic biology beyond the lab. *Nature Communications*, 12:1390, 03 2021.

[19] Fred S Grodins. *Control theory and biological systems*. Columbia University Press, 1963.

[20] Howard T Milhorn. Application of control theory to physiological systems. 1966.

[21] Karl Johan Aström and Richard M Murray. *Feedback systems: an introduction for scientists and engineers*. Princeton university press, 2010.

[22] Mustafa Khammash. An engineering viewpoint on biological robustness. *BMC biology*, 14(1):1–11, 2016.

[23] Lorena Postiglione, Sara Napolitano, Elisa Pedone, Daniel Rocca, Francesco Aulicino, Marco Santorelli, Barbara Tumaini, Lucia Marucci, and Diego Di Bernardo. Regulation of gene expression and signaling pathway activity in mammalian cells by automated microfluidics feedback control. *ACS Synthetic Biology*, 7, 10 2018.

[24] Gianfranco Fiore, Giansimone Perrino, Mario di Bernardo, and Diego di Bernardo. In vivo real-time control of gene expression: A comparative analysis of feedback control strategies in yeast. *ACS Synthetic Biology*, 5(2):154–162, 2015.

[25] Marc Rullan, Dirk Benzinger, Gregor W Schmidt, Andreas Milias-Argeitis, and Mustafa Khammash. An optogenetic platform for real-time, single-cell interrogation of stochastic transcriptional regulation. *Molecular cell*, 70(4):745–756, 2018.

[26] Anne Rademacher, Fabian Erdel, Jorge Trojanowski, Sabrina Schumacher, and Karsten Rippe. Real-time observation of light-controlled transcription in living cells. *Journal of Cell Science*, 130(24):4213–4224, 2017.

[27] Jared E Toettcher, Delquin Gong, Wendell A Lim, and Orion D Weiner. Light-based feedback for controlling intracellular signaling dynamics. *Nature methods*, 8(10):837–839, 2011.

[28] Andrew H Ng, Taylor H Nguyen, Mariana Gómez-Schiavon, Galen Dods, Robert A Langan, Scott E Boyken, Jennifer A Samson, Lucas M Waldburger, John E Dueber, David Baker, et al. Modular and tunable biological

feedback control using a de novo protein switch. *Nature*, 572(7768):265–269, 2019.

[29] Mingqi Xie, Haifeng Ye, Hui Wang, Ghislaine Charpin-El Hamri, Claude Lormeau, Pratik Saxena, Jörg Stelling, and Martin Fussenegger. β-cell–mimetic designer cells provide closed-loop glycemic control. *Science*, 354(6317):1296–1301, 2016.

[30] Mustafa H Khammash. Cybergenetics: Theory and applications of genetic control systems. *Proceedings of the IEEE*, 110(5):631–658, 2022.

[31] Hans V Westerhoff and Bernhard O Palsson. The evolution of molecular biology into systems biology. *Nature biotechnology*, 22(10):1249–1252, 2004.

[32] Roger Schneiter. Genetics, molecular and cell biology of yeast. 2004.

[33] B. Alberts. Molecular biology of the cell. *Garland Science*, 2000.

[34] Jonathan J Turner, Jennifer C Ewald, and Jan M Skotheim. Cell size control in yeast. *Current biology*, 22(9):R350–R359, 2012.

[35] Leland H Hartwell and Michael W Unger. Unequal division in saccharomyces cerevisiae and its implications for the control of cell division. *The Journal of cell biology*, 75(2):422–435, 1977.

[36] Murat Acar, Jerome T Mettetal, and Alexander Van Oudenaarden. Stochastic switching as a survival strategy in fluctuating environments. *Nature genetics*, 40(4):471–475, 2008.

[37] Hubertus JE Beaumont, Jenna Gallie, Christian Kost, Gayle C Ferguson, and Paul B Rainey. Experimental evolution of bet hedging. *Nature*, 462(7269):90–93, 2009.

[38] Tobias Claus Neymann, Sven Wegerhoff, and Sebastian Engell. Synchronization of budding yeast cultures. *IFAC Proceedings Volumes*, 44(1):8384–8390, 2011.

[39] Roger Lionel Poulter Adams. *Cell culture for biochemists*, volume 8. Elsevier, 1990.

[40] Bruce Futcher. Cell cycle synchronization. *Methods in cell science*, 21(2-3):79–86, 1999.

[41] Adam P Rosebrock. Methods for synchronization and analysis of the budding yeast cell cycle. *Cold Spring Harbor Protocols*, 2017(1):pdb–top080630, 2017.

[42] Jamie A Hackett and M Azim Surani. Regulatory principles of pluripotency: from the ground state up. *Cell stem cell*, 15(4):416–430, 2014.

[43] Kathryn C Davidson, Elizabeth A Mason, and Martin F Pera. The pluripotent state in mouse and human. *Development*, 142(18):3090–3099, 2015.

[44] Wojciech Zakrzewski, Maciej Dobrzyński, Maria Szymonowicz, and Zbigniew Rybak. Stem cells: past, present, and future. *Stem cell research & therapy*, 10(1):1–22, 2019.

[45] Kathryn Blair, Jason Wray, and Austin Smith. The liberation of embryonic stem cells. *PLoS genetics*, 7(4):e1002019, 2011.

[46] Siim Pauklin, Roger A Pedersen, and Ludovic Vallier. Mouse pluripotent stem cells at a glance. *Journal of cell science*, 124(22):3727–3732, 2011.

[47] Jun Wu and Juan Carlos Izpisua Belmonte. Dynamic pluripotent stem cell states and their applications. *Cell stem cell*, 17(5):509–525, 2015.

[48] Graziano Martello and Austin Smith. The nature of embryonic stem cells. *Annual review of cell and developmental biology*, 30:647–675, 2014.

[49] Martin J Evans and Matthew H Kaufman. Establishment in culture of pluripotential cells from mouse embryos. *nature*, 292(5819):154–156, 1981.

[50] Martin Evans. Discovering pluripotency: 30 years of mouse embryonic stem cells. *Nature reviews Molecular cell biology*, 12(10):680–686, 2011.

[51] Kazutoshi Takahashi and Shinya Yamanaka. Induction of pluripotent stem cells from mouse embryonic and adult fibroblast cultures by defined factors. *cell*, 126(4):663–676, 2006.

[52] Simon Hastreiter, Stavroula Skylaki, Dirk Loeffler, Andreas Reimann, Oliver Hilsenbeck, Philipp S Hoppe, Daniel L Coutu, Konstantinos D Kokkaliaris, Michael Schwarzfischer, Konstantinos Anastassiadis, et al. Inductive and selective effects of gsk3 and mek inhibition on nanog heterogeneity in embryonic stem cells. *Stem cell reports*, 11(1):58–69, 2018.

[53] Sabitri Ghimire, Margot Van der Jeught, Jitesh Neupane, Matthias S Roost, Jasper Anckaert, Mina Popovic, Filip Van Nieuwerburgh, Pieter Mestdagh, Jo Vandesompele, Dieter Deforce, et al. Comparative analysis of naive, primed and ground state pluripotency in mouse embryonic stem cells originating from the same genetic background. *Scientific reports*, 8(1):1–11, 2018.

[54] Carla Mulas, Tüzer Kalkan, Ferdinand von Meyenn, Harry G Leitch, Jennifer Nichols, and Austin Smith. Defined conditions for propagation and manipulation of mouse embryonic stem cells. *Development*, 146(6):dev173146, 2019.

[55] Qi-Long Ying and Austin G Smith. Defined conditions for neural commitment and differentiation. *Methods in enzymology*, 365:327–341, 2003.

[56] Elisa Pedone, Mario Failli, Gennaro Gambardella, Rossella De Cegli, Antonella La Regina, Diego di Bernardo, and Lucia Marucci. β-catenin perturbations control differentiation programs in mouse embryonic stem cells. *Iscience*, 25(2):103756, 2022.

[57] Tüzer Kalkan and Austin Smith. Mapping the route from naive pluripotency to lineage specification. *Philosophical Transactions of the Royal Society B: Biological Sciences*, 369(1657):20130540, 2014.

[58] Chen-Yun Chen, Yuan-Yuan Cheng, Christopher YT Yen, and Patrick CH Hsieh. Mechanisms of pluripotency maintenance in mouse embryonic stem cells. *Cellular and Molecular Life Sciences*, 74(10):1805–1817, 2017.

[59] Qi-Long Ying, Jason Wray, Jennifer Nichols, Laura Batlle-Morera, Bradley Doble, James Woodgett, Philip Cohen, and Austin Smith. The ground state of embryonic stem cell self-renewal. *nature*, 453(7194):519–523, 2008.

[60] Qi-Long Ying, Jennifer Nichols, Ian Chambers, and Austin Smith. Bmp induction of id proteins suppresses differentiation and sustains embryonic stem cell self-renewal in collaboration with stat3. *Cell*, 115(3):281–292, 2003.

[61] Jiho Choi, Aaron J Huebner, Kendell Clement, Ryan M Walsh, Andrej Savol, Kaixuan Lin, Hongcang Gu, Bruno Di Stefano, Justin Brumbaugh, Sang-Yong Kim, et al. Prolonged mek1/2 suppression impairs the developmental potential of embryonic stem cells. *Nature*, 548(7666):219–223, 2017.

[62] Masaki Yagi, Satoshi Kishigami, Akito Tanaka, Katsunori Semi, Eiji Mizutani, Sayaka Wakayama, Teruhiko Wakayama, Takuya Yamamoto, and Yasuhiro Yamada. Derivation of ground-state female es cells maintaining gamete-derived dna methylation. *Nature*, 548(7666):224–227, 2017.

[63] Takeshi Shimizu, Jun Ueda, Jolene Caifeng Ho, Katsuhiko Iwasaki, Lorenz Poellinger, Ichiro Harada, and Yasuhiro Sawada. Dual inhibition of src and gsk3 maintains mouse embryonic stem cells, whose differentiation is mechanically regulated by src signaling. *Stem cells*, 30(7):1394–1404, 2012.

[64] Seyedeh-Nafiseh Hassani, Mehdi Totonchi, Ali Sharifi-Zarchi, Sepideh Mollamohammadi, Mohammad Pakzad, Sharif Moradi, Azam Samadian, Najmehsadat Masoudi, Shahab Mirshahvaladi, Ali Farrokhi, et al. Inhibition of tgfβ signaling promotes ground state pluripotency. *Stem Cell Reviews and Reports*, 10(1):16–30, 2014.

[65] Cian J Lynch, Raquel Bernad, Ana Martínez-Val, Marta N Shahbazi, Sandrina Nóbrega-Pereira, Isabel Calvo, Carmen Blanco-Aparicio, Carolina Tarantino, Elena Garreta, Laia Richart-Ginés, et al. Global hyperactivation of enhancers stabilizes human and mouse naive pluripotency through inhibition of cdk8/19 mediator kinases. *Nature Cell Biology*, 22(10):1223–1238, 2020.

[66] Patrick Cahan, Davide Cacchiarelli, Sara-Jane Dunn, Martin Hemberg, Susana M Chuva de Sousa Lopes, Samantha A Morris, Owen JL Rackham, Antonio Del Sol, and Christine A Wells. Computational stem cell biology: open questions and guiding principles. *Cell Stem Cell*, 28(1):20–32, 2021.

[67] Maria Herberg and Ingo Roeder. Computational modelling of embryonic stem-cell fate control. *Development*, 142(13):2250–2260, 2015.

[68] Maria Herberg, Tüzer Kalkan, Ingmar Glauche, Austin Smith, and Ingo Roeder. A model-based analysis of culture-dependent phenotypes of mescs. *PloS one*, 9(3):e92496, 2014.

[69] Ayako Yachie-Kinoshita, Kento Onishi, Joel Ostblom, Matthew A Langley, Eszter Posfai, Janet Rossant, and Peter W Zandstra. Modeling signaling-dependent pluripotency with boolean logic to predict cell fate transitions. *Molecular systems biology*, 14(1):e7952, 2018.

[70] Lucia Marucci. Nanog dynamics in mouse embryonic stem cells: results from systems biology approaches. *Stem cells international*, 2017, 2017.

[71] Ian Chambers, Jose Silva, Douglas Colby, Jennifer Nichols, Bianca Nijmeijer, Morag Robertson, Jan Vrana, Ken Jones, Lars Grotewold, and Austin Smith. Nanog safeguards pluripotency and mediates germline development. *Nature*, 450(7173):1230–1234, 2007.

[72] Tibor Kalmar, Chea Lim, Penelope Hayward, Silvia Munoz-Descalzo, Jennifer Nichols, Jordi Garcia-Ojalvo, and Alfonso Martinez Arias. Regulated fluctuations in nanog expression mediate cell fate decisions in embryonic stem cells. *PLoS biology*, 7(7):e1000149, 2009.

[73] Vijay Chickarmane, Victor Olariu, and Carsten Peterson. Probing the role of stochasticity in a model of the embryonic stem cell–heterogeneous gene expression and reprogramming efficiency. *BMC systems biology*, 6:1–12, 2012.

[74] Elisa Pedone, Irene de Cesare, Criseida G. Zamora-Chimal, David Haener, Lorena Postiglione, Antonella La Regina, Barbara Shannon, Nigel J. Savery, Claire S. Grierson, Mario di Bernardo, Thomas E. Gorochowski, and Lucia Marucci. Cheetah: A computational toolkit for cybergenetic control. *ACS Synthetic Biology*, 10(5):979–989, 2021. PMID: 33904719.

[75] Gianfranco Fiore. Identification and control of gene networks in living cells. 2015.

[76] Todd M Squires and Stephen R Quake. Microfluidics: Fluid physics at the nanoliter scale. *Reviews of modern physics*, 77(3):977, 2005.

[77] Scott Cookson, Natalie Ostroff, Wyming Lee Pang, Dmitri Volfson, and Jeff Hasty. Monitoring dynamics of single-cell gene expression over multiple cell cycles. *Molecular systems biology*, 1(1), 2005.

[78] Sahand Jamal Rahi, Kresti Pecani, Andrej Ondracka, Catherine Oikonomou, and Frederick R Cross. The cdk-apc/c oscillator predominantly entrains periodic cell-cycle transcription. *Cell*, 165(2):475–487, 2016.

[79] G Charvin, FR Cross, and ED Siggia. Forced periodic expression of g1 cyclins phase-locks the budding yeast cell cycle. *Proceedings of the National Academy of Sciences*, 106(16):6632–6637, 2009.

[80] Jennifer M Gardner and Sue L Jaspersen. Manipulating the yeast genome: deletion, mutation, and tagging by pcr. In *Yeast Genetics*, pages 45–78. Springer, 2014.

[81] Mike S Ferry, Ivan A Razinkov, and Jeff Hasty. Microfluidics for synthetic biology: from design to execution. In *Methods in enzymology*, volume 497, pages 295–372. Elsevier, 2011.

[82] Giansimone Perrino, Cathal Wilson, Marco Santorelli, and Diego di Bernardo. Quantitative characterization of α-synuclein aggregation in living cells through automated microfluidics feedback control. *Cell reports*, 27(3):916–927, 2019.

[83] Sahand Jamal Rahi, Johannes Larsch, Kresti Pecani, Alexander Y Katsov, Nahal Mansouri, Krasimira Tsaneva-Atanasova, Eduardo D Sontag, and Frederick R Cross. Oscillatory stimuli differentiate adapting circuit topologies. *Nature methods*, 14(10):1010, 2017.

[84] Qiong Yang and James E Ferrell Jr. The cdk1–apc/c cell cycle oscillator circuit functions as a time-delayed, ultrasensitive switch. *Nature cell biology*, 15(5):519, 2013.

[85] WO Friesen and GD Block. What is a biological oscillator? *American Journal of Physiology-Regulatory, Integrative and Comparative Physiology*, 246(6):R847–R853, 1984.

[86] Arthur T Winfree. *The geometry of biological time*, volume 12. Springer Science & Business Media, 2001.

[87] Yoshiki Kuramoto. *Chemical oscillations, waves, and turbulence*. Courier Corporation, 2003.

[88] Dane Taylor, Per Sebastian Skardal, and Jie Sun. Synchronization of heterogeneous oscillators under network modifications: Perturbation and optimization of the synchrony alignment function. *SIAM journal on applied mathematics*, 76(5):1984–2008, 2016.

[89] Hiroya Nakao. Phase reduction approach to synchronization of nonlinear oscillators. *arXiv preprint arXiv:1704.03293*, 2017.

[90] Giansimone Perrino, Davide Fiore, Sara Napolitano, Mario di Bernardo, and Diego di Bernardo. Towards feedback control of the cell-cycle across a population of yeast cells. In *2019 18th European Control Conference (ECC)*, pages 2644–2650. IEEE, 2019.

[91] He Bai and John T Wen. Asymptotic synchronization of phase oscillators with a single input. *IEEE Transactions on Automatic Control*, 64(4):1611–1618, 2018.

[92] Martin Kolnik, Lev S Tsimring, and Jeff Hasty. Vacuum-assisted cell loading enables shear-free mammalian microfluidic culture. *Lab on a chip*, 12(22):4732–4737, 2012.

[93] Jonathan W Young, James CW Locke, Alphan Altinok, Nitzan Rosenfeld, Tigran Bacarian, Peter S Swain, Eric Mjolsness, and Michael B Elowitz. Measuring single-cell gene expression dynamics in bacteria using fluorescence time-lapse microscopy. *Nature protocols*, 7(1):80–88, 2012.

[94] Erik Meijering. Cell segmentation: 50 years down the road [life sciences]. *IEEE signal processing magazine*, 29(5):140–145, 2012.

[95] Nobuyuki Otsu. A threshold selection method from gray-level histograms. *IEEE transactions on systems, man, and cybernetics*, 9(1):62–66, 1979.

[96] Thorsten Falk, Dominic Mai, Robert Bensch, Özgün Çiçek, Ahmed Abdulkadir, Yassine Marrakchi, Anton Böhm, Jan Deubner, Zoe Jäckel, Katharina Seiwald, et al. U-net: deep learning for cell counting, detection, and morphometry. *Nature methods*, 16(1):67–70, 2019.

[97] Jean-Baptiste Lugagne, Haonan Lin, and Mary J Dunlop. Delta: Automated cell segmentation, tracking, and lineage reconstruction using deep learning. *PLoS computational biology*, 16(4):e1007673, 2020.

[98] Jason Wray, Tüzer Kalkan, Sandra Gomez-Lopez, Dominik Eckardt, Andrew Cook, Rolf Kemler, and Austin Smith. Inhibition of glycogen synthase kinase-3 alleviates tcf3 repression of the pluripotency network and

increases embryonic stem cell resistance to differentiation. *Nature cell biology*, 13(7):838–845, 2011.

[99] Ronald J Parchem, Julia Ye, Robert L Judson, Marie F LaRussa, Raga Krishnakumar, Amy Blelloch, Michael C Oldham, and Robert Blelloch. Two mirna clusters reveal alternative paths in late-stage reprogramming. *Cell stem cell*, 14(5):617–631, 2014.

[100] Fatimah Ibrahim, NA Abu Osman, Juliana Usman, and Nahrizul Adib Kadri. *3rd Kuala Lumpur International Conference on Biomedical Engineering 2006: Biomed 2006, 11-14 December 2006, Kuala Lumpur, Malaysia*, volume 15. Springer Science & Business Media, 2007.

[101] Kevin Ward and Z Hugh Fan. Mixing in microfluidic devices and enhancement methods. *Journal of Micromechanics and Microengineering*, 25(9):094001, 2015.

[102] Philip Dettinger, Tino Frank, Martin Etzrodt, Nouraiz Ahmed, Andreas Reimann, Christoph Trenzinger, Dirk Loeffler, Konstantinos D Kokkaliaris, Timm Schroeder, and Savas Tay. Automated microfluidic system for dynamic stimulation and tracking of single cells. *Analytical chemistry*, 90(18):10695–10700, 2018.

[103] Jason Wray, Tuzer Kalkan, and Austin G Smith. The ground state of pluripotency. *Biochemical Society Transactions*, 38(4):1027–1032, 2010.

[104] Satoshi Ohtsuka and Hitoshi Niwa. The differential activation of intracellular signaling pathways confers the permissiveness of embryonic stem cell derivation from different mouse strains. *Development*, 142(3):431–437, 2015.

[105] Jose Silva, Ornella Barrandon, Jennifer Nichols, Jitsutaro Kawaguchi, Thorold W Theunissen, and Austin Smith. Promotion of reprogramming to ground state pluripotency by signal inhibition. *PLoS biology*, 6(10):e253, 2008.

[106] Pablo Navarro. 2i, or not 2i: The soliloquy of nanog-negative mouse embryonic stem cells. *Stem Cell Reports*, 11(1):1–3, 2018.

[107] Jamie A Hackett, Toshihiro Kobayashi, Sabine Dietmann, and M Azim Surani. Activation of lineage regulators and transposable elements across a pluripotent spectrum. *Stem cell reports*, 8(6):1645–1658, 2017.

[108] Baojiang Wu, Yunxia Li, Bojiang Li, Baojing Zhang, Yanqiu Wang, Lin Li, Junpeng Gao, Yuting Fu, Shudong Li, Chen Chen, et al. Dnmts play an important role in maintaining the pluripotency of leukemia inhibitory

factor-dependent embryonic stem cells. *Stem cell reports*, 16(3):582–596, 2021.

[109] Yuguang Xiong, Magali Soumillon, Jie Wu, Jens Hansen, Bin Hu, Johan Gc Van Hasselt, Gomathi Jayaraman, Ryan Lim, Mehdi Bouhaddou, Loren Ornelas, et al. A comparison of mrna sequencing with random primed and 3-directed libraries. *Scientific reports*, 7(1):1–12, 2017.

[110] Tanja Magoč and Steven L Salzberg. Flash: fast length adjustment of short reads to improve genome assemblies. *Bioinformatics*, 27(21):2957–2963, 2011.

[111] Liguo Wang, Shengqin Wang, and Wei Li. Rseqc: quality control of rna-seq experiments. *Bioinformatics*, 28(16):2184–2185, 2012.

[112] Michael I Love, Wolfgang Huber, and Simon Anders. Moderated estimation of fold change and dispersion for rna-seq data with deseq2. *Genome biology*, 15(12):1–21, 2014.

[113] Alex L Mitchell, Teresa K Attwood, Patricia C Babbitt, Matthias Blum, Peer Bork, Alan Bridge, Shoshana D Brown, Hsin-Yu Chang, Sara El-Gebali, Matthew I Fraser, et al. Interpro in 2019: improving coverage, classification and access to protein sequence annotations. *Nucleic acids research*, 47(D1):D351–D360, 2019.

[114] Antonio Fabregat, Steven Jupe, Lisa Matthews, Konstantinos Sidiropoulos, Marc Gillespie, Phani Garapati, Robin Haw, Bijay Jassal, Florian Korninger, Bruce May, et al. The reactome pathway knowledgebase. *Nucleic acids research*, 46(D1):D649–D655, 2018.

[115] Denise N Slenter, Martina Kutmon, Kristina Hanspers, Anders Riutta, Jacob Windsor, Nuno Nunes, Jonathan Mélius, Elisa Cirillo, Susan L Coort, Daniela Digles, et al. Wikipathways: a multifaceted pathway database bridging metabolomics to other omics research. *Nucleic acids research*, 46(D1):D661–D667, 2018.

[116] Vasundhra Kashyap, Naira C Rezende, Kymora B Scotland, Sebastian M Shaffer, Jenny Liao Persson, Lorraine J Gudas, and Nigel P Mongan. Regulation of stem cell pluripotency and differentiation involves a mutual regulatory circuit of the nanog, oct4, and sox2 pluripotency transcription factors with polycomb repressive complexes and stem cell microrna. *Stem cells and development*, 18(7):1093–1108, 2009.

[117] Mahmoud Khazim, Lorena Postiglione, Elisa Pedone, Dan L Rocca, Carine Zahra, and Lucia Marucci. Towards automated control of embryonic stem cell pluripotency. *IFAC-PapersOnLine*, 52(26):82–87, 2019.

[118] Shin-ya Hatano, Masako Tada, Hironobu Kimura, Shinpei Yamaguchi, Tomohiro Kono, Toru Nakano, Hirofumi Suemori, Norio Nakatsuji, and Takashi Tada. Pluripotential competence of cells associated with nanog activity. *Mechanisms of development*, 122(1):67–79, 2005.

[119] Tüzer Kalkan, Nelly Olova, Mila Roode, Carla Mulas, Heather J Lee, Isabelle Nett, Hendrik Marks, Rachael Walker, Hendrik G Stunnenberg, Kathryn S Lilley, et al. Tracking the embryonic stem cell transition from ground state pluripotency. *Development*, 144(7):1221–1234, 2017.

[120] Igor Boiko. Oscillations and transfer properties of relay servo systems—the locus of a perturbed relay system approach. *Automatica*, 41(4):677–683, 2005.

[121] Zalmanovich Tsykin, Iakov and Yakov Z Tsypkin. *Relay control systems*. CUP Archive, 1984.

[122] Mark A Krasnosel'skii and Aleksei V Pokrovskii. *Systems with hysteresis*. Springer Science & Business Media, 2012.

[123] Katherine M McKinnon. Flow cytometry: an overview. *Current protocols in immunology*, 120(1):5–1, 2018.

[124] Satoshi Ohtsuka, Yoko Nakai-Futatsugi, and Hitoshi Niwa. Lif signal in mouse embryonic stem cells. *Jak-stat*, 4(2):1–9, 2015.

[125] Elisa Figallo, Christopher Cannizzaro, Sharon Gerecht, Jason A Burdick, Robert Langer, Nicola Elvassore, and Gordana Vunjak-Novakovic. Micro-bioreactor array for controlling cellular microenvironments. *Lab on a Chip*, 7(6):710–719, 2007.

[126] Spyridon Achinas, Jorn-Ids Heins, Janneke Krooneman, and Gerrit Jan Willem Euverink. Miniaturization and 3d printing of bioreactors: a technological mini review. *Micromachines*, 11(9):853, 2020.

[127] Tiago Ramos and Lorenzo Moroni. Tissue engineering and regenerative medicine 2019: the role of biofabrication—a year in review. *Tissue Engineering Part C: Methods*, 26(2):91–106, 2020.

[128] John A Reid, Peter A Mollica, Garett D Johnson, Roy C Ogle, Robert D Bruno, and Patrick C Sachs. Accessible bioprinting: adaptation of a low-cost 3d-printer for precise cell placement and stem cell differentiation. *Biofabrication*, 8(2):025017, 2016.